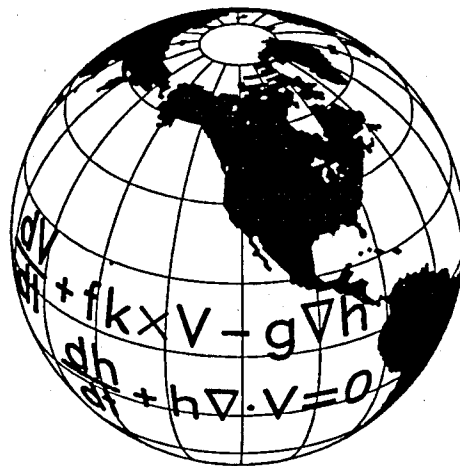May 1993

Solutions to the Shallow Water Test Set Using the Spectral Transform Method

RUEDIGER JAKOB
JAMES J. HACK
DAVID L. WILLIAMSON

CLIMATE AND GLOBAL DYNAMICS DIVISION

NATIONAL CENTER FOR ATMOSPHERIC RESEARCH
BOULDER, COLORADO

INTRODUCTION

A standard test set for numerical approximations to the shallow water equations in spherical geometry has been proposed by Williamson et. al. (1992). The present technical note contains solutions to those test cases that were obtained using the spectral transform method. The detailed mathematical formulation of the numerical test set are not included in this report. Thus, this technical note relies strongly on Williamson et al. (1992) for a detailed mathematical description of the test cases and the requested performance metrics.

The spectral transform method was first introduced by Orszag (1970) and Eliasen, Machenhauer and Rasmussen (1970), and is summarized in the review by Machenhauer (1979). The solutions in this report were produced by a spectral transform shallow water model, whose specific algorithm and numerical approximations are described in Hack and Jakob (1992). The spectral transform shallow water model (STSWM) is coded in the Fortran 77 programming language (ANSI X3J3, 1978) and is available via anonymous FTP from the authors. A more detailed description is available in electronic form from

ftp.ucar.edu (IP address: 128.117.64.4)

in the plain text file
/chammp/shallow/docu/description.txt

Reference solutions for Test Case 5 (Zonal flow over an isolated mountain), Test Case 6 (Rossby-Haurwitz wave) and Test Case 7 (Analyzed 500 mb height and wind field initial conditions) were computed using the STSWM since the solutions to these test cases are not analytic. The model code was compiled using the Cray Fortran CFT77 compiler, version 5.0.4.1 and executed under operating system UNICOS, version 6.1 on a Cray Y-MP 8/864. Real and integer variables used a word length of 64 bits, which equals about 15 decimal digits accuracy for the mantissa of real variables. Further detail on how these reference solutions were obtained, along with measures of their uncertainty, are provided in Appendix A. The solutions themselves are provided in the form of spectral expansion coefficients using the portable NetCDF data format. Fortran code to project these coefficients onto an arbitrary grid is also included. Instructions on how to obtain the solutions and code can be found in the plain text file

/chammp/shallow/docu/refsol.txt

The reference solutions and codes are also available at Oak Ridge National Laboratory. One can obtain a list of available material by mailing "send index from chammp" to netlib@ornl.gov. Instructions on how to obtain the solutions and code can be obtained by mailing "send README from chammp" to netlib@ornl.gov. Difficulties in accessing the

files at NCAR should be reported to the NCAR computer consulting office at 303-497-1278 (email: consult1@ncar.ucar.edu). Difficulties in accessing files at ORNL should be reported electronically to bbd@ornl.gov. Software bugs, along with suggested fixes, should be reported electronically to stswm@ncar.ucar.edu.

All solutions have been computed using triangular spectral truncations, which have become the most commonly adopted spectral truncation, due to the isotropic nature of the underlying spectral representation. Alternative truncation strategies, such as rhomboidal truncation, are generally used for extremely low resolution models, and are not considered here. Table 1 lists the spectral truncations employed in the following numerical experiments and the corresponding number of meridional and longitudinal points for the transform grid. The longitudinal distribution of the grid points is equiangular, but the meridional distribution is not equiangular. The meridional grid points are located at the Gaussian latitudes θ_j, which are the J roots of the Legendre polynomial: $P_J(\sin \theta_j) = 0$. The number of grid points in each direction is determined by aliasing considerations. To allow unaliased representation of quadratic terms,

$$ I \quad \geq \quad 3M + 1 \tag{1} $$

$$ J \quad \geq \quad (3K + 1)/2 \tag{2} $$

where I and J are the number of longitude and latitude grid points, respectively, and M and K are the highest wavenumbers retained in the longitudinal Fourier and latitudinal Legendre representations respectively. Furthermore, the model requires an even number of latitudes to make convenient use of the associated Legendre function symmetry. The number of longitudes are also constrained to have only the prime factors 2, 3 and 5 to allow use of the highly efficient FFT library developed by Temperton (1983).

Spectral Truncation	Number of Grid Points	
M	meridional: J	longitudinal: I
42	64	128
63	96	192
106	160	320
170	256	512
213	320	640

Table 1: Spectral Transform Grid Resolution

Table 2 lists the time steps that have been used to produce the solutions presented in this document, unless specifically stated otherwise in the text. The time step scales approximately as 1/N for reasons associated with linear stability.

Spectral Truncation	Timestep (Seconds)
42	1200
63	900
106	600
170	450
213	360

Table 2: Model Time Step as a Function of Truncation

The global integral (Eq. 81 in Williamson et. al., 1992), used in many of the errors measures

$$I(h) = \int_0^{2\pi} \int_{-\frac{\pi}{2}}^{\frac{\pi}{2}} h(\lambda, \theta) \cos \theta d\theta d\lambda, \qquad (3)$$

is approximated by the discrete double sum

$$I(h) \approx \frac{2\pi}{I} \sum_{i=1}^{I} \sum_{j=1}^{J} h(\lambda_i, \theta_j) w_j, \qquad (4)$$

where w_j are the weights of the Gaussian quadrature given by

$$w_j = \frac{2 \cos^2 \theta_j}{[J P_{J-1}(\sin \theta_j)]^2}, \qquad (5)$$

The approximation is exact up to zonal wavenumber I/2 and degree 2J + 1 of the associated Legendre functions. For a discussion of the effects of grid sampling and spectral truncation, also see Sections 1 and 3.

The optional Asselin time filter, which is included with the code, has not been used for the solutions presented here, unless specifically stated otherwise, since no significant even-odd temporal mode splitting was observed during relatively short integration periods.

Test Case 5 of Williamson et al. (1992) uses an irregular lower boundary (i.e. surface topography) requiring changes to the shallow water equations and numerical algorithms in Hack and Jakob (1992) (hereafter referred to as HJ92). Let h_s denote the height of the mountains, h^* the depth of the fluid, and $h = h^* + h_s$ the height of the free surface. In the momentum equation (2.1) of HJ92, the pressure gradient force is based on the gradient of the free surface

$$\frac{d\mathbf{V}}{dt} = -f\mathbf{k} \times \mathbf{V} - \nabla(\Phi_s + \Phi^*),$$ (6)

where the surface geopotential $\Phi_s = gh_s$ and $\Phi^* = gh^*$. The mass continuity equation (2.2) of HJ92 applies only to the fluid itself

$$\frac{d\Phi^*}{dt} = -\Phi^* \nabla \cdot \mathbf{V} .$$ (7)

As in HJ92, the geopotential Φ^* is divided into a time-invariant spatial mean $\overline{\Phi}$ and a time-dependent deviation $\Phi' = \Phi^* - \overline{\Phi}$. After applying the *curl* and *div* operators, the prediction equations (2.12)-(2.14) of HJ92 are now:

$$\frac{\partial \eta}{\partial t} = -\frac{1}{a(1-\mu^2)}\frac{\partial}{\partial \lambda}(U\eta) - \frac{1}{a}\frac{\partial}{\partial \mu}(V\eta),$$ (8)

$$\frac{\partial \delta}{\partial t} = \frac{1}{a(1-\mu^2)}\frac{\partial}{\partial \lambda}(V\eta) - \frac{1}{a}\frac{\partial}{\partial \mu}(U\eta) - \nabla^2\left(\Phi_s + \Phi' + \frac{U^2 + V^2}{2(1-\mu^2)}\right),$$ (9)

$$\frac{\partial \Phi'}{\partial t} = -\frac{1}{a(1-\mu^2)}\frac{\partial}{\partial \lambda}(U\Phi') - \frac{1}{a}\frac{\partial}{\partial \mu}(V\Phi') - \overline{\Phi}\delta .$$ (10)

The generalized equations only add the surface topography term Φ_s in the divergence tendency equation. The changes to the numerical algorithm are thus relatively small. Only the definition of the intermediate variable E in (5.11) of HJ92 must be changed to

$$E \equiv \Phi_s + \frac{U^2 + V^2}{2(1-\mu^2)} .$$ (11)

A diffusion operator, of the type typically applied to atmospheric general circulation models, has been added to the shallow water model to deal with spectral blocking for Test Cases 5, 6, and 7. Diffusion is important for the lower resolution model integrations where the initial data have significant energy near the truncation limit. Thus the prediction

4

equations (2.12)-(2.14) of HJ92 are expanded to include a parameterization of sub-grid scale mixing in the form of a dissipation term F_η^{Diff}, F_δ^{Diff} and F_Φ^{Diff}

$$\frac{\partial \eta}{\partial t} = -\frac{1}{a(1-\mu^2)}\frac{\partial}{\partial \lambda}(U\eta) - \frac{1}{a}\frac{\partial}{\partial \mu}(V\eta) + F_\eta^{Diff} \; , \tag{12}$$

$$\frac{\partial \delta}{\partial t} = \frac{1}{a(1-\mu^2)}\frac{\partial}{\partial \lambda}(V\eta) - \frac{1}{a}\frac{\partial}{\partial \mu}(U\eta) - \nabla^2\left(\Phi_s + \Phi' + \frac{U^2+V^2}{2(1-\mu^2)}\right) + F_\delta^{Diff} \; , \tag{13}$$

$$\frac{\partial \Phi'}{\partial t} = -\frac{1}{a(1-\mu^2)}\frac{\partial}{\partial \lambda}(U\Phi') - \frac{1}{a}\frac{\partial}{\partial \mu}(V\Phi') - \overline{\Phi}\delta + F_\Phi^{Diff} \; . \tag{14}$$

The form of the dissipation term is equivalent to the horizontal diffusion used in the NCAR Community Climate Model (Williamson et al., 1987). The diffusion term is given by

$$F_\eta^{Diff} = -K_4[\nabla^4\eta - \frac{4}{a^4}\eta] \; , \tag{15}$$

$$F_\delta^{Diff} = -K_4[\nabla^4\delta - \frac{4}{a^4}\delta] \; , \tag{16}$$

$$F_\Phi^{Diff} = -K_4\nabla^4\left(\overline{\Phi} + \Phi' + \Phi_s\right) \; . \tag{17}$$

The linear correction term has been added to the vorticity and divergence operator to prevent damping of solid body rotation. The geopotential diffusion operator is applied to the free surface geopotential to prevent spurious damping caused by surface topography. The linear diffusion operator is applied in spectral space

$$\left\{F_\eta^{Diff}\right\}_n^m = -K_4\frac{[n(n+1)]^2 - 4}{a^4}\eta_n^m \; , \tag{18}$$

$$\left\{F_\delta^{Diff}\right\}_n^m = -K_4\frac{[n(n+1)]^2 - 4}{a^4}\delta_n^m \; , \tag{19}$$

$$\left\{F_\Phi^{Diff}\right\}_n^m = -K_4\frac{[n(n+1)]^2}{a^4}\left(\{\Phi'\}_n^m + \{\Phi_s\}_n^m\right) \; , \tag{20}$$

and as follows for the case $n = 0$:

$$\left\{F_\eta^{Diff}\right\}_0^0 = 0 \tag{21}$$

$$\left\{F_\delta^{Diff}\right\}_0^0 = 0 \tag{22}$$

5

The spectral terms are computed implicitly in the code after the spectral coefficients for the new time level have been computed, i.e.,

$$\left\{\eta^{Diff}\right\}_n^m = \eta_n^m - 2\Delta t K_4 \frac{[n(n+1)]^2 - 4}{a^4} \left\{\eta^{Diff}\right\}_n^m \tag{23}$$

$$\left\{\delta^{Diff}\right\}_n^m = \delta_n^m - 2\Delta t K_4 \frac{[n(n+1)]^2 - 4}{a^4} \left\{\delta^{Diff}\right\}_n^m \tag{24}$$

$$\left\{\Phi'^{Diff}\right\}_n^m = \Phi'^m_n - 2\Delta t K_4 \frac{[n(n+1)]^2}{a^4} \left(\left\{\Phi'^{Diff}\right\}_n^m + \left\{\Phi_s\right\}_n^m\right) \tag{25}$$

Table 3 lists values of the diffusion coefficients K_4 that have been used in the model runs unless specifically stated otherwise. The coefficients scale as $[N(N+1)]^{-2}$ (because of spectral form of ∇^4 operator), so that the smallest scales (highest wavenumber) are damped at about the same rate. The effect of diffusion on the solutions is discussed in Appendix A.

Spectral Truncation	K_4 (m^4/s)
42	0.50 x 10^{16}
63	1.00 x 10^{15}
106	1.25 x 10^{14}
170	2.00 x 10^{13}
213	8.00 x 10^{12}

Table 3: Diffusion Coefficient K_4 as a Function of Spectral Truncations

The reader is referred to Williamson et al., (1992) for complete descriptions of the test cases and their associated error measures, and the values for all physical constants.

Sequential and parallel performance results for the STSWM code on the Cray Y-MP vector multiprocessor can be found in Jakob (1993), which also includes a performance model for the spectral transform algorithm and its implementation. Table 4 contains representative execution times and execution rates for a semi-implicit time step as a function of model resolution for Test Case 2 (see Williamson et al., 1992, section 3).

6

Spectral truncation	T-42	T-63	T-106	T-170	T-213
Execution time	0.019	0.053	0.184	0.598	1.140
Execution rate	162	169	198	214	215

Table 4: Representative CPU time (seconds) and floating point execution rate (in millions of floating point operations per second or MFLOPS) on a single processor of a CRAY Y-MP per semi-implicit time step as a function of horizontal spectral resolution. Execution time for a five day integration (as discussed in Williamson et al., 1992) can be obtained by combining this data with the time step data in Table 2.

1. Advection of Cosine Bell over the Pole

This test case is designed to test the advective component of a numerical scheme in isolation; i.e., it does not deal with the complete shallow water system. For this test case a cosine bell is advected once around the sphere, directly around the equator, directly over the poles, and at slight angles to these two extremes, to expose any problems associated with asymmetries. Examples of the initial height field, which should be maintained throughout the course of one rotation, and the initial height truncated to T42 resolution are shown in Figure 1.1a and b respectively, for the $\alpha = \pi/2 - 0.05$ case. For all rotation angles, α, the final height fields after one rotation (288 hours or 864 time steps of 1200 seconds) are visibly indistinguishable from each other so only the $\alpha = \pi/2 - 0.05$ case is shown in Figure 1.2a. Even the error fields for the different rotation angles ($\alpha = 0$, 0.05, $\pi/2 - 0.05$, and $\pi/2$) are extremely similar to each other, so it is only necessary to show the $\pi/2 - 0.05$ error in Figure 1.2b. The l_1, l_2, and l_∞ error measures are shown in Figure 1.3 for the $\pi/2 - 0.05$ rotation angle with a T42 truncation and 1200 sec time step (once again, these curves are very similar for all four rotation angles, only the details of the high frequency noise component differ). These error estimates show a significant error associated with the initial representation of the cosine bell, followed by a systematic monotonic increase as the cosine bell is advected around the sphere.

In addition to the global error estimates, this test case requests the time dependent behavior of the normalized mean, variance, minimum and maximum values in the height field. These curves are quite different in character for each of the four rotation angles, and are therefore presented individually for the T42 case in Figures 1.4 - 1.7. In all cases the relative errors are very small, but exhibit uniquely different modulations of the high frequency behavior. By manipulating the analytic solution in various ways it can be demonstrated that the high frequency behavior seen in these figures is attributable to sampling the solution on a discrete grid. For example, the expanding envelope seen in the normalized maximum height error is a consequence of sampling a solution with a very small phase error introduced by time truncation (and can be reproduced by sampling the *analytic* solution with a slight phase error). Thus, the running average represents the fundamental amplitude error. Note the clear signature of a pole crossing in all the error estimates for the $\pi/2 - 0.05$ and $\pi/2$ rotation angle solutions. Once again, this is a consequence of sampling on the discrete grid, arising from a significantly larger meridional grid interval at the polar cap.

Finally, in Figure 1.8 we show the standard global error estimates as a function of horizontal truncation at the $\pi/2 - 0.05$ rotation angle to illustrate the convergence properties of the solution. The time steps used were 600, 900, 600 and 450 sec for the T42, T63, T106 and T170 truncations respectively. These are the standard values listed in the introduction with the exception of the T42 value. For this figure, the value was chosen to be the same as the T106 value to illustrate the role of the time truncation error. Error
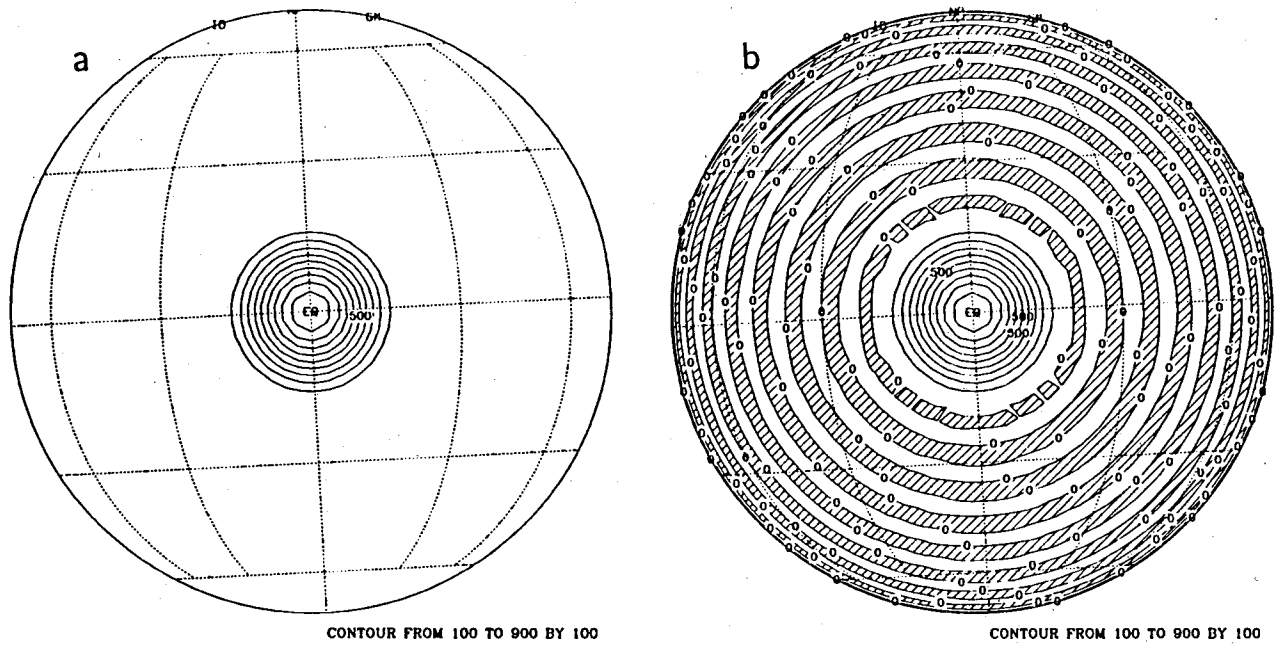
Figure 1.1 Initial height field (a) and height field truncated to T42 (b) for $\alpha = \pi/2 - 0.05$ case. Contour interval is 100 m.
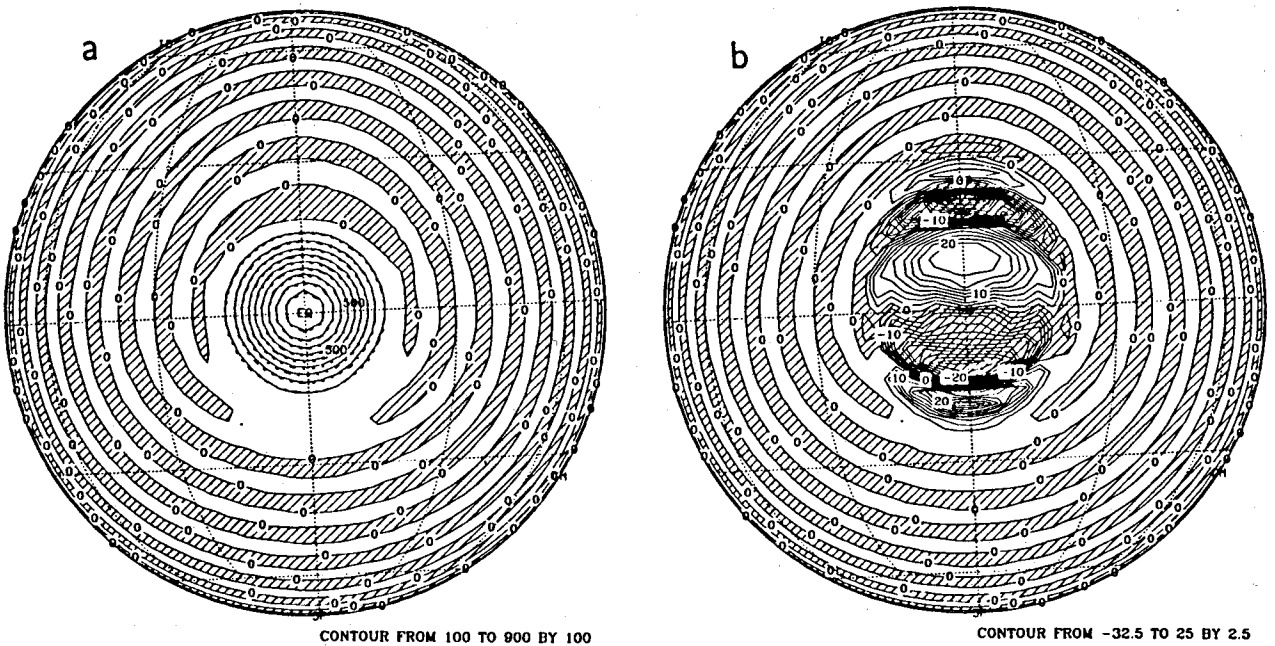
Figure 1.2 Height field (a) and height field error (b) after one rotation for $\alpha = \pi/2 - 0.05$ case. Contour interval is 100 m for the field and 2.5 m for the error.

10

estimates with the T42 standard time step of 1200 were shown earlier in Figure 1.3. The curves in Figure 1.8 show large differences in all measures at the initial state (associated with spectral runcation), with significantly smaller values at the higher resolutions. The growth in the error estimates (i.e., the slope of these measures with respect to time) appears to be dominated by time truncation error. This can be clearly seen by comparing the T106 and T42 results with each other since both were run with the same time step. In addition, comparison with the T42 case in Figure 1.3 with a 1200 sec time step also shows the faster growth with the longer time step. Thus, the selected time step is an important component in the error estimates reported for this test case.
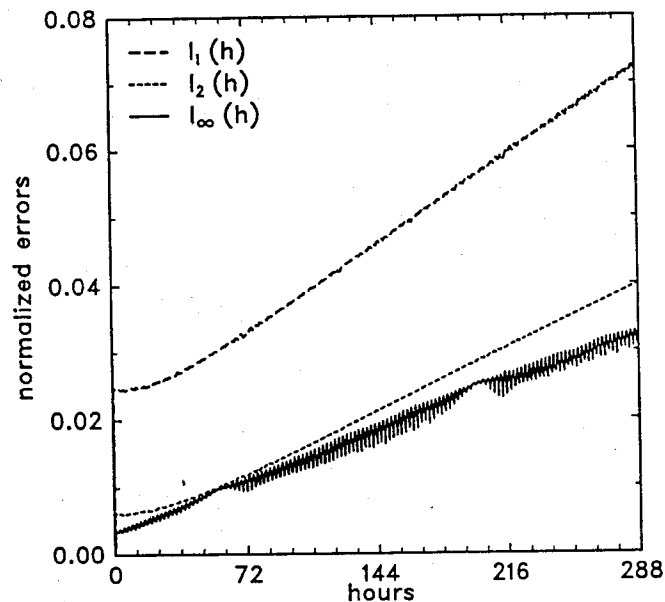
Figure 1.3 l_1 (long dash), l_2 (short dash), and l_∞ (solid) errors versus time during one rotation for $\alpha = \pi/2 - 0.05$ case.
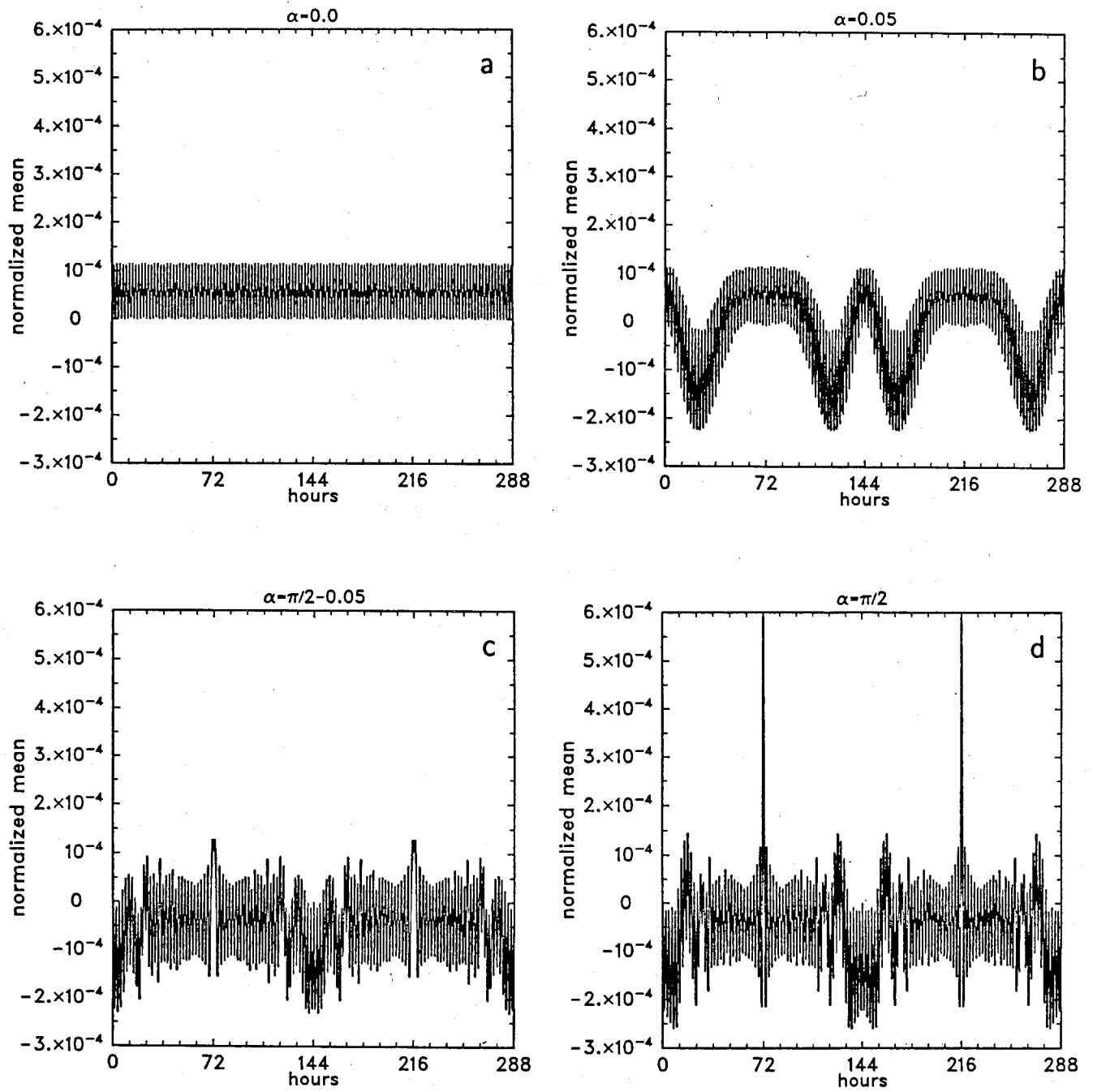
Figure 1.4 Normalized mean error versus time during one rotation for (a) $\alpha = 0.0$, (b) $\alpha = 0.05$, (c) $\alpha = \pi/2 - 0.05$, and (d) $\alpha = \pi/2$.
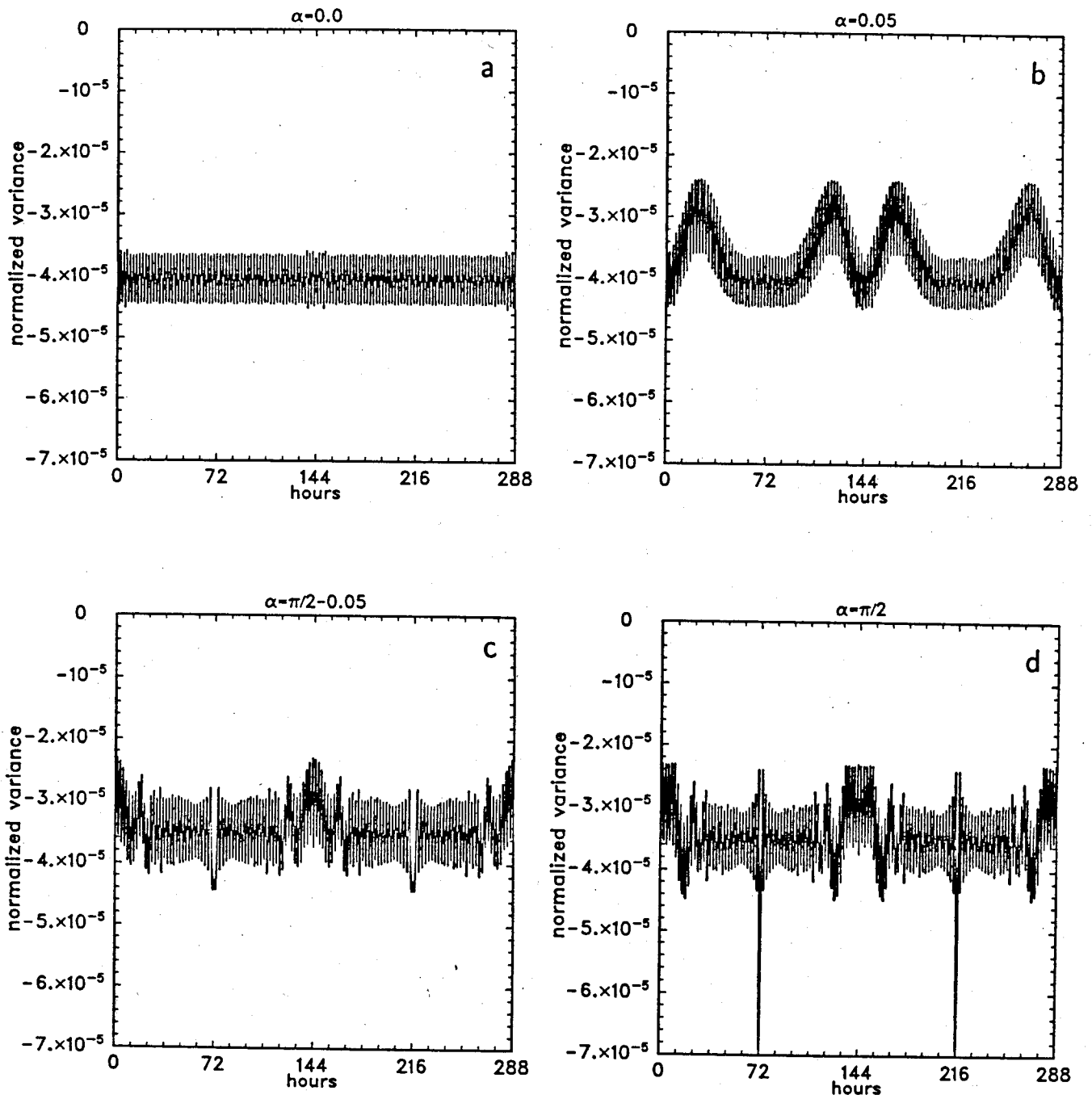
Figure 1.5 Normalized variance error versus time during one rotation for (a) $\alpha = 0.0$, (b) $\alpha = 0.05$, (c) $\alpha = \pi/2 - 0.05$, and (d) $\alpha = \pi/2$.

13
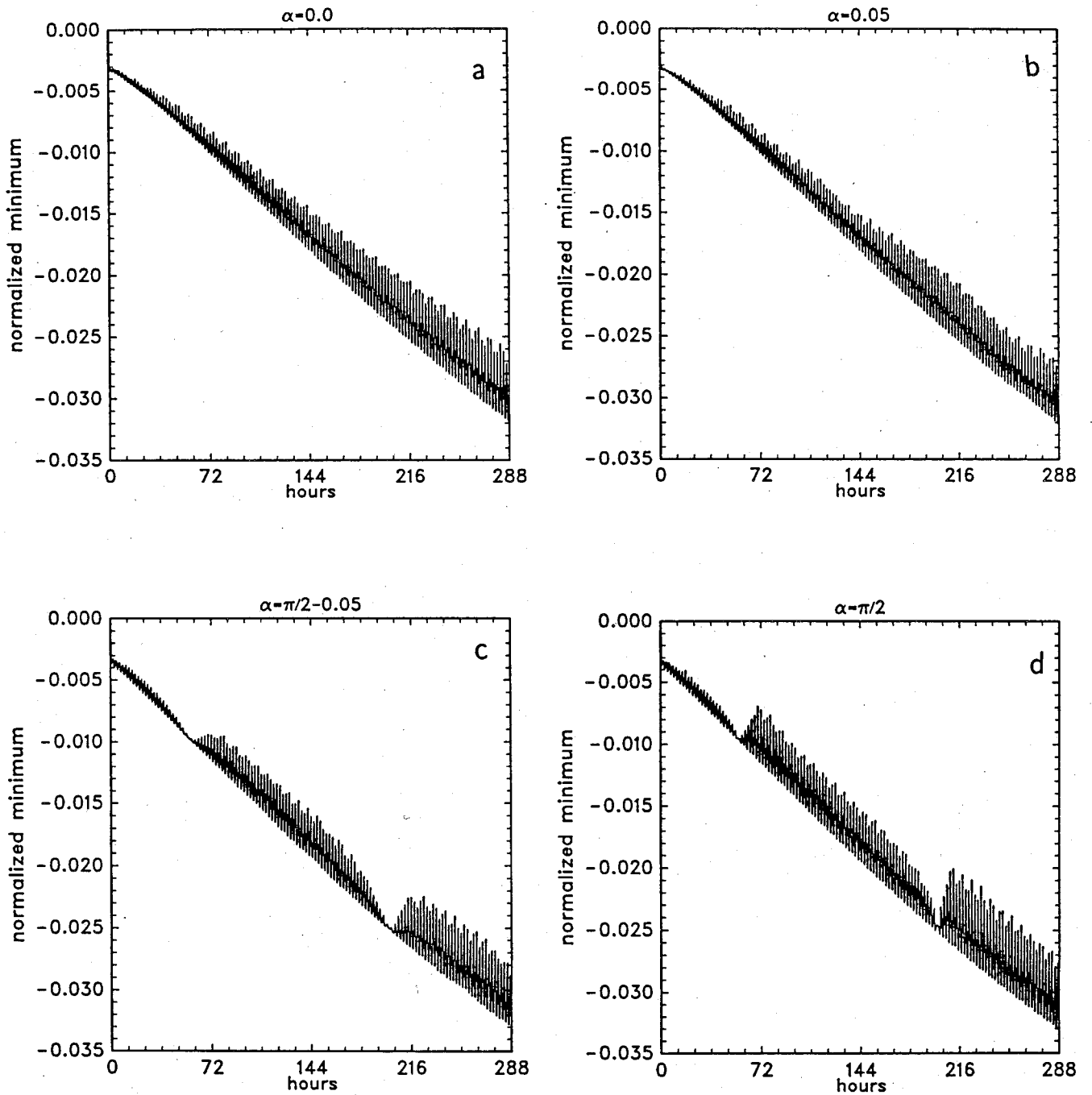
Figure 1.6 Normalized minimum versus time during one rotation for (a) $\alpha = 0.0$, (b) $\alpha = 0.05$, (c) $\alpha = \pi/2 - 0.05$, and (d) $\alpha = \pi/2$.

14
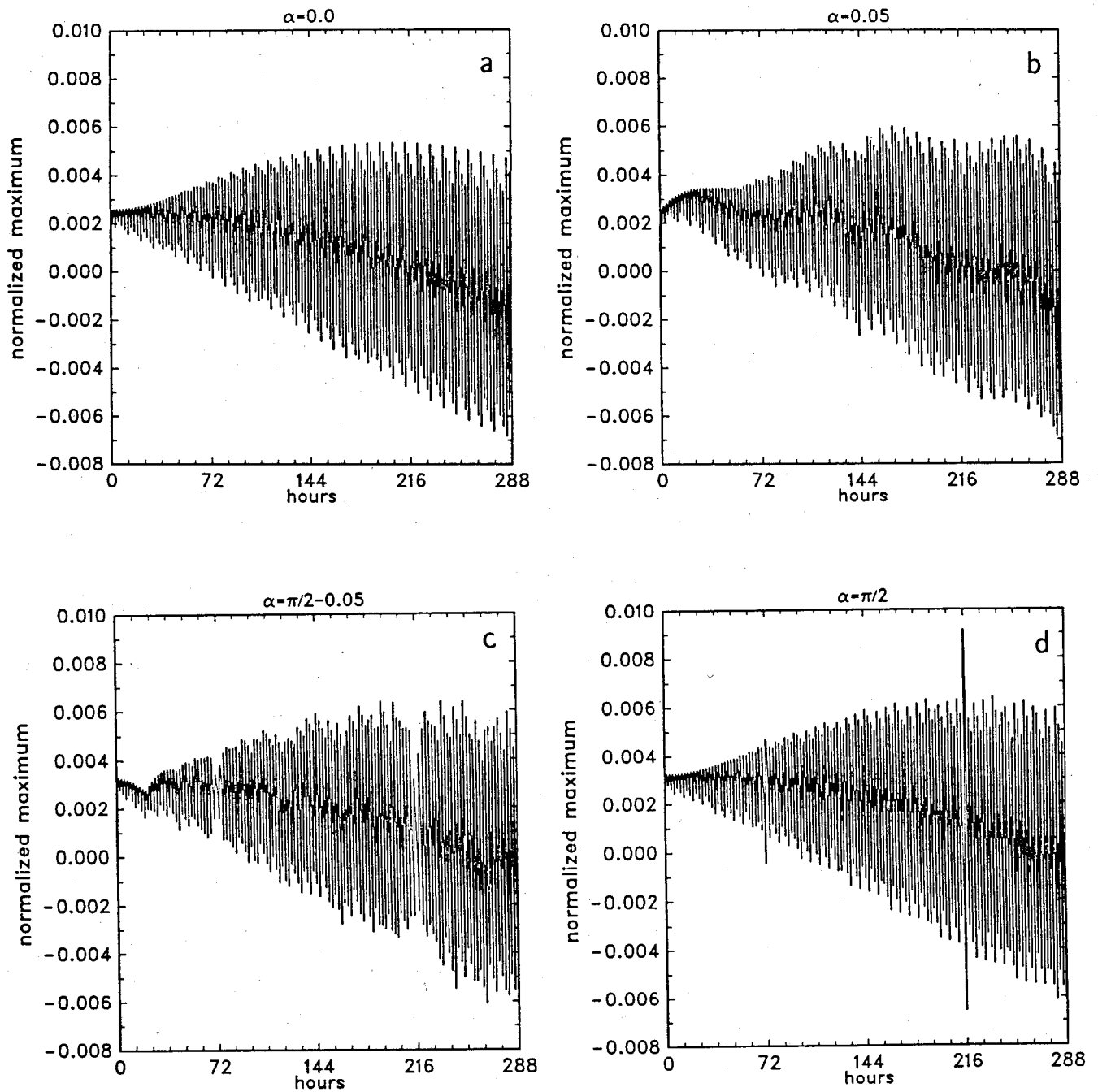
Figure 1.7 Normalized maximum versus time during one rotation for (a) $\alpha = 0.0$, (b) $\alpha = 0.05$, (c) $\alpha = \pi/2 - 0.05$, and (d) $\alpha = \pi/2$.

15
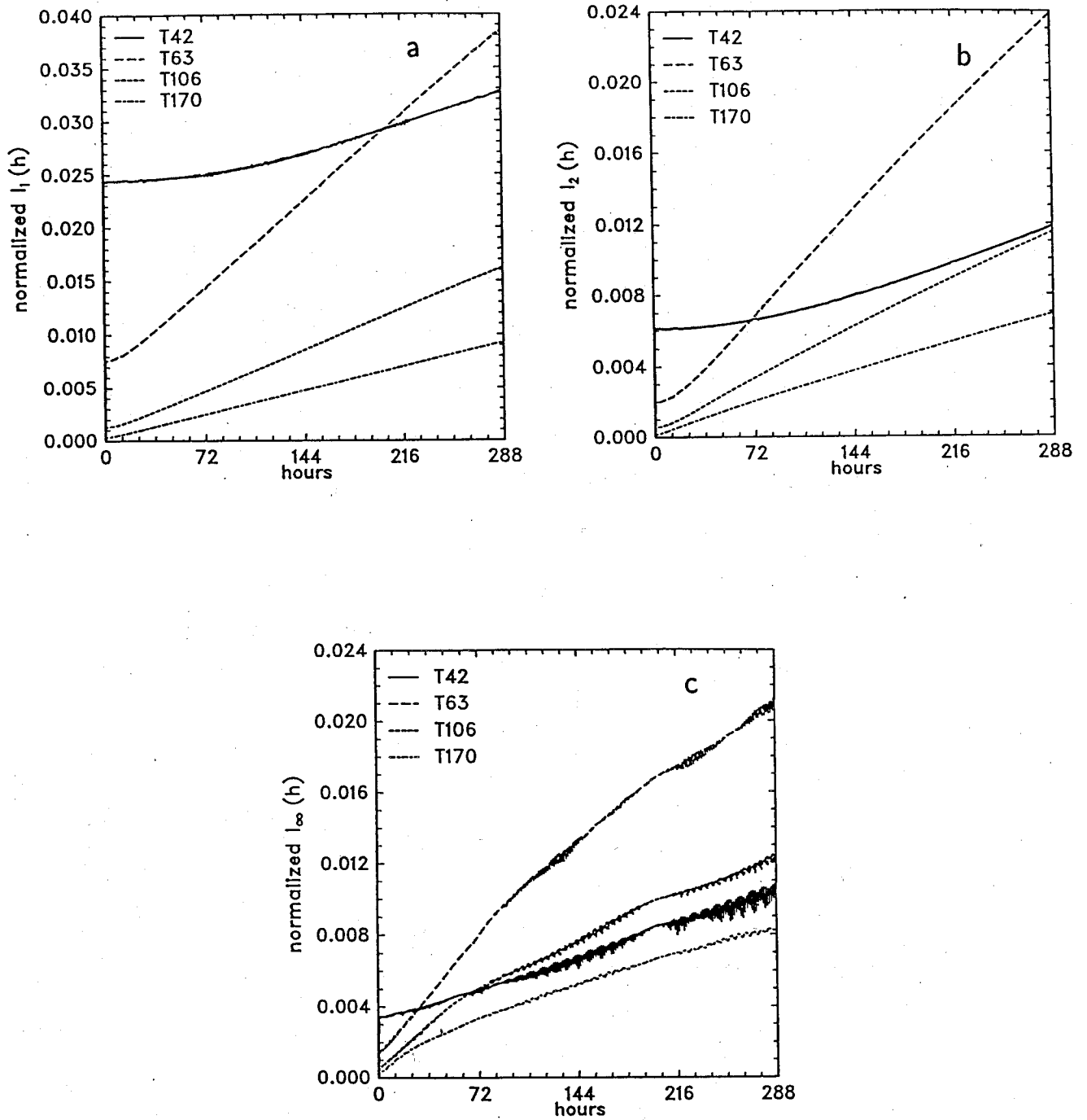
Figure 1.8 l_1 (a), l_2 (b), and l_∞ (c) height errors for T42, T63, T106, and T170 truncations with 600, 900, 600, and 450 second time steps respectively.

2. Global Steady State Nonlinear Zonal Geostrophic Flow

This zonal geostrophic flow case is a trivial problem for the spectral transform method. The height and wind fields are represented exactly by the basis functions of degree $n \leq 1$. The errors reflect the accumulation of rounding errors associated with the particular implementation and computer rather than truncation errors of the method. Therefore there is no point in performing a convergence study, and we present details for T42 resolution only. The errors in the following discussion are extremely small and there is clearly no need for competitive schemes to do anywhere near as well to be considered viable for atmospheric models. We consider these errors simply to explore the characteristics of the particular implementation of the STSWM code.

Figure 2.1 shows the l_1, l_2 and l_∞ height and wind errors, for the T42 cases for each of the four rotation angles. The thicker solid line is for $\alpha = 0$, the thin line for $\alpha = 0.05$, the thin dashed line is for $\alpha = \pi/2 - 0.05$, and the thick dashed line for $\alpha = \pi/2$. The h error for the $\alpha = 0.0$ and 0.05 cases are very close to each other and in many instances the thin and thick lines overlay each other. The $\alpha = \pi/2$ and $\pi/2 - 0.05$ are also close to each other but with smaller values than the other pair. The wind errors have similar characteristics. Figures 2.2 and 2.3 illustrate the nature of the error. Figure 2.2 shows the initial and analytic solution and Figure 2.3 shows the northern hemisphere (with respect to the rotational system) errors at Day 5. With $\alpha = 0.0$ and 0.05 the error is concentrated near the representational poles and coincident or nearly coincident with the rotational poles. (Here we define the representational pole to be the pole associated with the spectral representation or computational grid, and the rotational pole to be associated with the rotating geometry of the physical problem.) When the representational pole is near the rotational equator, the errors are more evenly distributed (Figure 2.3c and d). Figure 2.4 helps to explain the source of these errors. This figure shows the errors as in Figure 2.3 but for time 0, after the spectral truncation of the initial data. In all cases the errors are associated with the representational pole and are associated with the discrete computational non-normality and non-orthogonality of the polynomials. The codes which generated the associated Legendre functions used in these tests produce functions with orthogonality and normality errors which can be as large as 1000 ϵ where ϵ is machine accuracy (1.4×10^{-14}) for CRAY floating point format. The largest orthogonality and normality errors are given in Table 2.1 for the resolutions in this study. These errors are defined as the largest Gaussian quadrature of any associated Legendre function with any other of same order m and the largest of one minus the quadrature of any function with itself. The errors are not equally distributed but are particularly large for order $m=0$ and $m=1$ and relatively large degree n for those two wave numbers. Thus the initial representational errors maximize at the representational poles. The errors remain concentrated there and grow in the two cases in which the flow is concentric to this error ($\alpha=0.0$ and 0.05). In the other cases ($\alpha = \pi/2 - 0.05$ and $\pi/2$) the initial error, located

17

in the center of the jet, is advected zonally (in the rotational sense) by the jet and then propagates meridionally.

Resolution	Orthogonality	Normality
T42	9.0×10^{-12}	8.5×10^{-12}
T63	1.7×10^{-11}	1.6×10^{-11}
T106	8.5×10^{-11}	8.5×10^{-11}
T213	3.2×10^{-10}	3.2×10^{-10}

Table 2.1: Maximum error

As would be expected, the orthonormality errors are reduced using double precision for the calculation of the Gaussian latitudes, weights and polynomials. At T42 the maximum orthogonality and normality errors are reduced to 8.0×10^{-14} and 2.2×10^{-13} respectively when the latitudes and weights are calculated in double precision and to 3.5×10^{-14} and 6.8×10^{-14} respectively, when in addition the polynomials themselves are calculated in double precision. In both cases the quadrature continues to be in single precision. Thus the orthonormality is still not to machine accuracy because of rounding error in the quadrature itself.
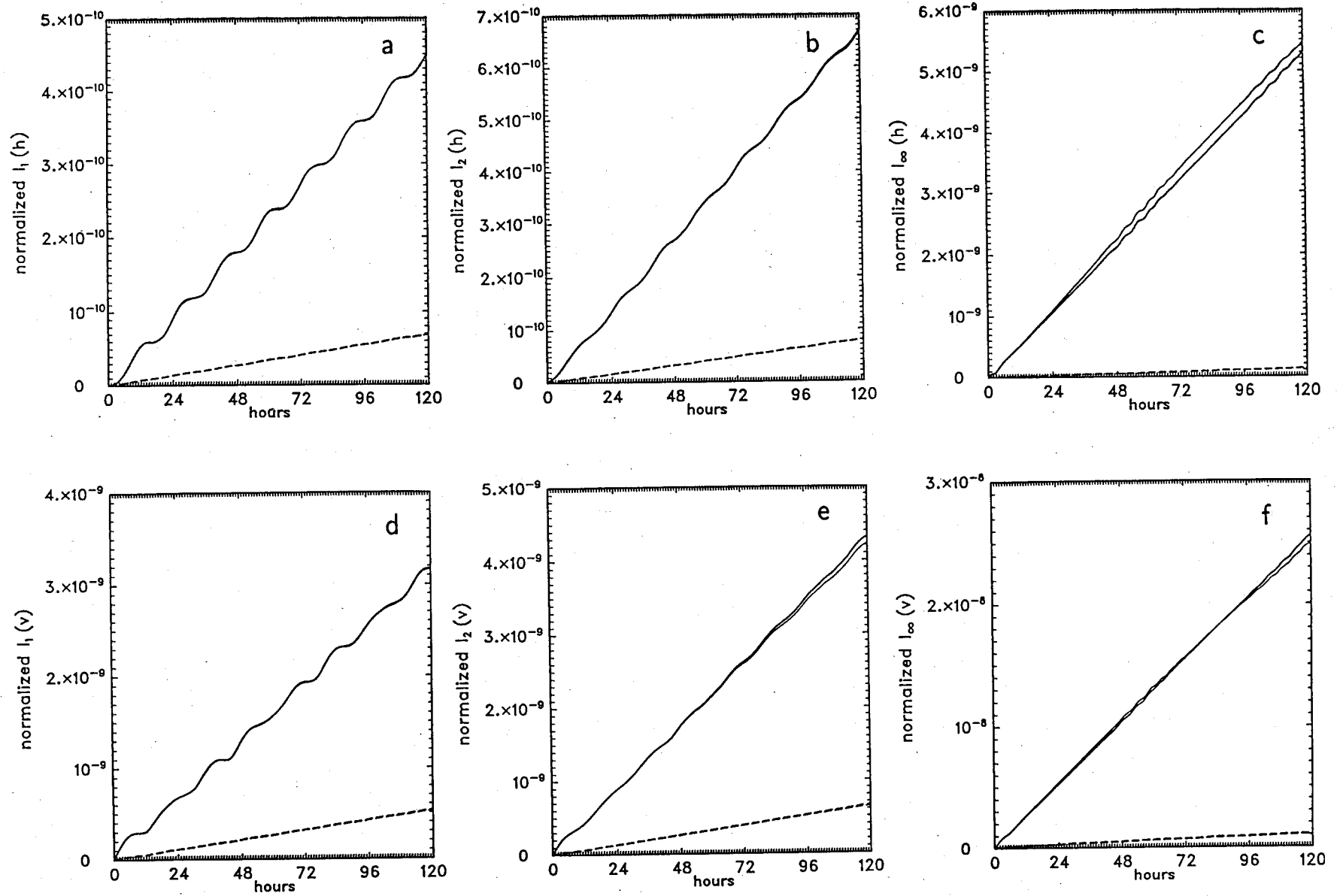
Figure 2.1 l_1, l_2, and l_∞ height errors (a–c) and l_1, l_2, and l_∞ wind errors (d–f) for T42, zonal geostrophic flow case. Thick solid for $\alpha = 0$, thin solid for $\alpha = 0.05$, thin dashed for $\alpha = \pi/2 - 0.05$, and thick dashed for $\alpha = \pi/2$.

CONTOUR FROM 1100 TO 2900 BY 100
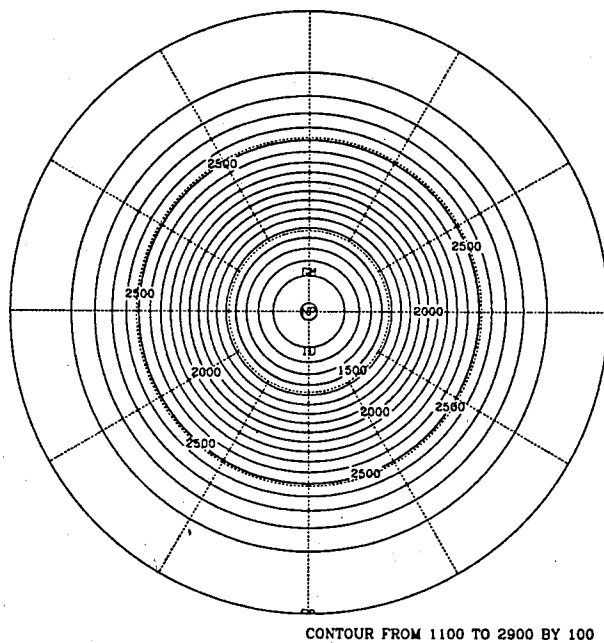
Figure 2.2 Initial and analytic solution height field plotted on a North polar (with respect to the rotational system) stereographic projection (outer circle is the equator). Contour interval is 100 m.

a

CONTOUR FROM -.000001 TO .000015 BY .000001

b

CONTOUR FROM -.000001 TO .000016 BY .000001

c

CONTOUR FROM -.000000375 TO .000000175 BY .000000025

d

CONTOUR FROM -.000000375 TO .00000015 BY .000000025
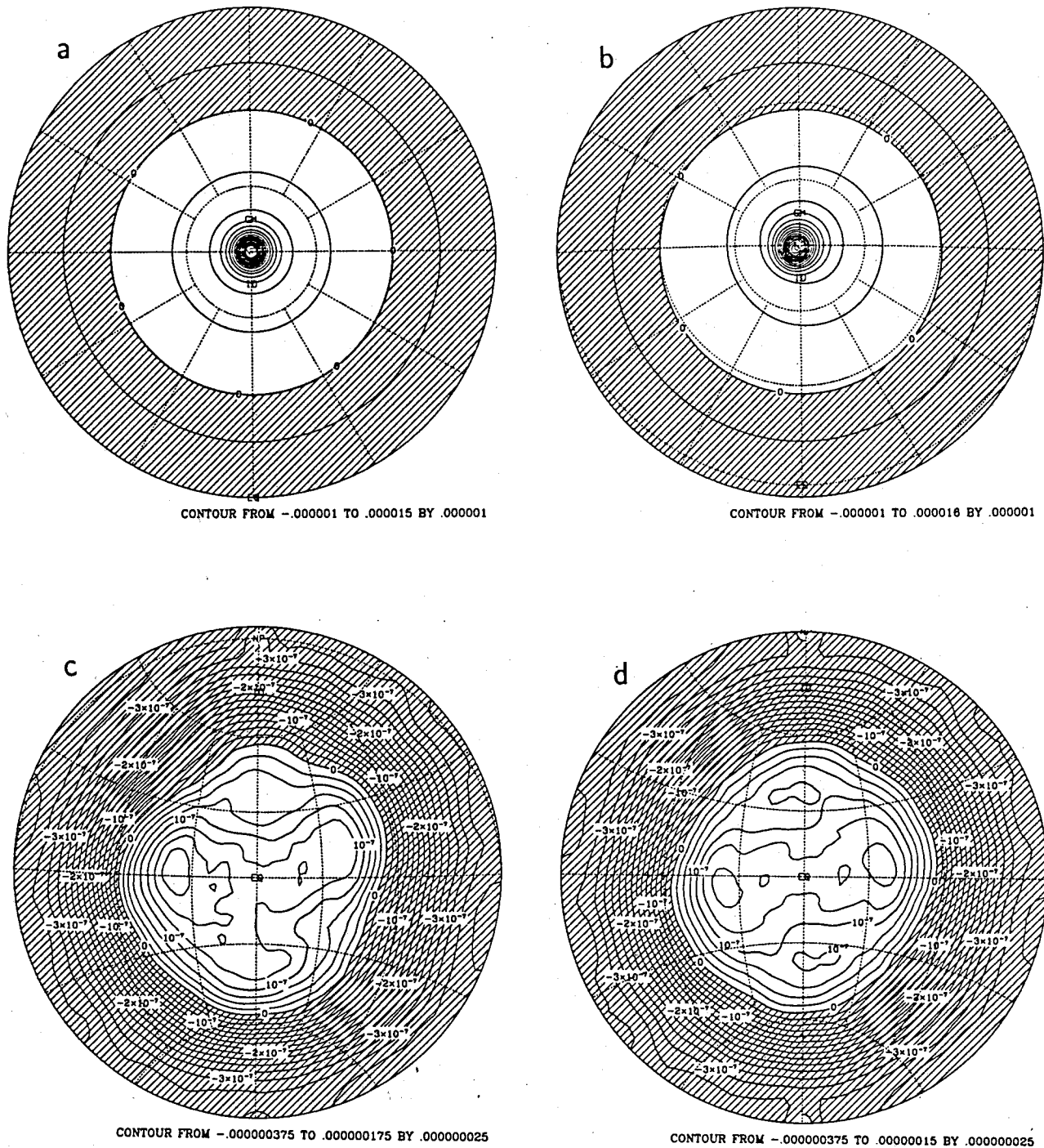
Figure 2.3 Height errors at day 5 for T42 case plotted on a North polar (with respect to the rotational system) stereographic projection (outer circle is the equator). (a) $\alpha = 0$, (b) $\alpha = 0.05$, (c) $\alpha = \pi/2 - 0.05$, and (d) $\alpha = \pi/2$. Contour intervals are 1×10^{-6} for (a) and (b), and 2.5×10^{-8} for (c) and (d).

21

CONTOUR FROM 0 TO .000000155 BY .000000005

CONTOUR FROM 0 TO .000000155 BY .000000005

CONTOUR FROM −7.5×10⁻⁸ TO 0 BY 0.5×10⁻⁸

CONTOUR FROM −7.5×10⁻⁸ TO 0 BY 0.5×10⁻⁸
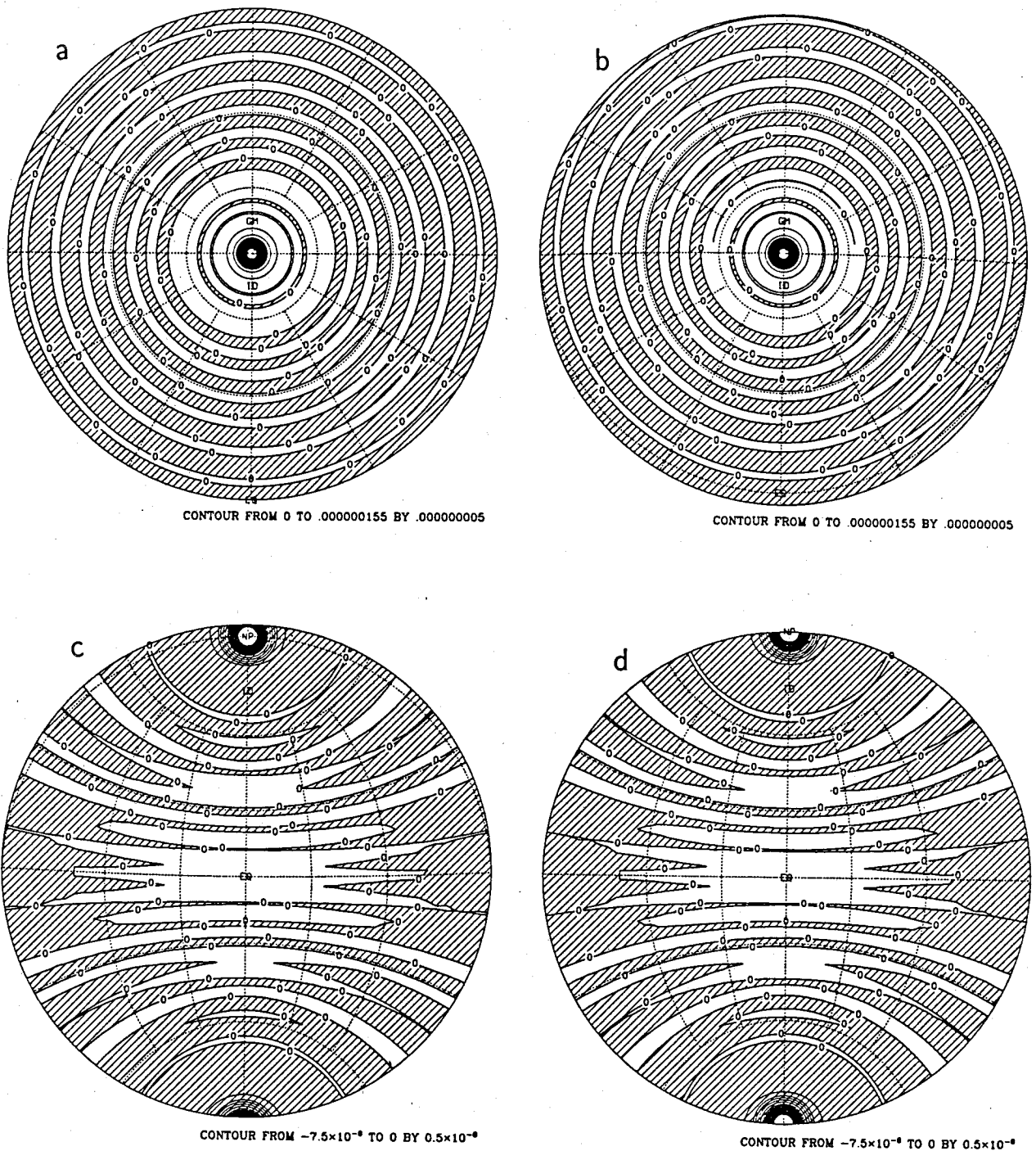
Figure 2.4 Height errors at day 0 after initial spectral truncation for T42 case plotted on a North polar (with respect to the rotational system) stereographic projection (outer circle is the equator). (a) $\alpha = 0$, (b) $\alpha = 0.05$, (c) $\alpha = \pi/2 - 0.05$, and (d) $\alpha = \pi/2$. Contour interval is 5 x 10^{-9}.

3. Steady State Nonlinear Zonal Geostrophic Flow with Compact Support

The zonal geostrophic flow with compact support is also essentially a trivial problem for the spectral transform method at resolutions in use today. During the 5 day integration, the errors reflect truncation rather than roundoff at T42, but initially they are only one order of magnitude larger for the height and two orders for the wind than the discrete orthonormality errors seen in the previous section, and thus are insignificant with regard to practical problems. As with Test Case 2, competitive schemes do not have to do equally well to be considered for practical applications. Figure 3.1 shows the l_1, l_2 and l_∞ height and wind errors for the T42 case with $\alpha = 0$ (wide solid line) and $\alpha = \pi/3$ (dashed line) along with the T63 case with $\alpha = \pi/3$ (narrow solid line). Compared to the global scale zonal flow of the previous section the T42, $\alpha = 0$ height errors are larger initially, then grow as they do in the global case. In the $\alpha = \pi/3$ case the height errors are larger in the compact support case than the global case for the entire period, as the global case shows slow growth for the 5 day period. The noise superimposed on the T42 curves is probably attributable to the lack of initialization in this integration. Very small amplitude gravity waves are present due to errors in the calculation of the integral involved in determining the height field. These waves propagate meridionally (as defined by the rotational pole, rather than the representational pole) and are present to the same extent in the both the $\alpha = 0$ and $\pi/3$ cases. The noise observed is due to the discrete sampling of these waves as their maxima and minima fall near and between the discrete grid points. The T63 case shows a growth behavior similar to the rounding accumulation in the global zonal case. This is not inconsistent with the larger orthonormality errors observed with and smaller truncation errors expected with higher resolution. In addition, the noise associated with the discrete sampling of the erroneous gravity waves is significantly smaller because the gravity waves themselves are smaller. The integral defining the initial conditions is approximated more accurately on the T63 grid. The l_1, l_2 and l_∞ wind errors for the T42 case (Figure 3.1) are up to two orders of magnitude larger than the errors in the global case and show little growth during the 5 day integration.

Figure 3.2 shows the true height fields in the upper row and height errors at 5 days in the lower row. The $\alpha = 0$ case is on the left and the $\alpha = \pi/3$ case is on the right. The errors are clearly associated with the rotational pole in both cases and thus represent truncation error rather than the orthonormality error associated with the representational pole seen in the global case. Further evidence that the errors are truncation-based rather than roundoff is provided in Figure 3.3. The top row shows the initial T42 truncation error due solely to the initial spectral representation for $\alpha = 0$ (a) and $\pi/3$ (b). Figure 3.3c shows the initial error for the T63, $\alpha = \pi/3$ case. The truncation error is reduced (as expected) to a level at which the discrete orthonormality error becomes evident at the representational pole. Further evidence that this is the case is provided by Figure 3.3d, which is also T63, $\alpha = \pi/3$, but with the Gaussian latitudes and weights and the associated Legendre functions calculated in double precision. The quadrature remains in single precision. The error is now dominated by truncation error.
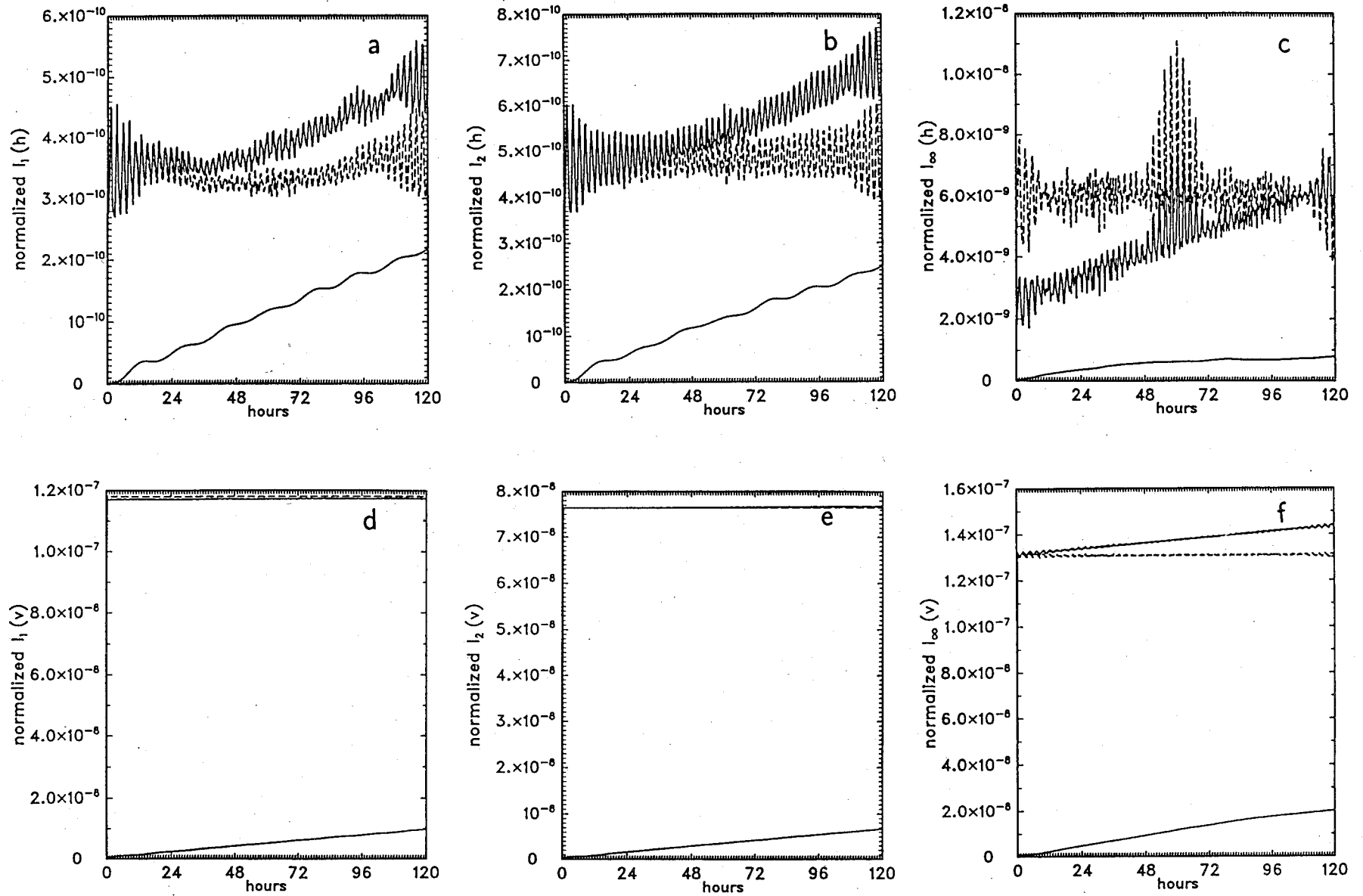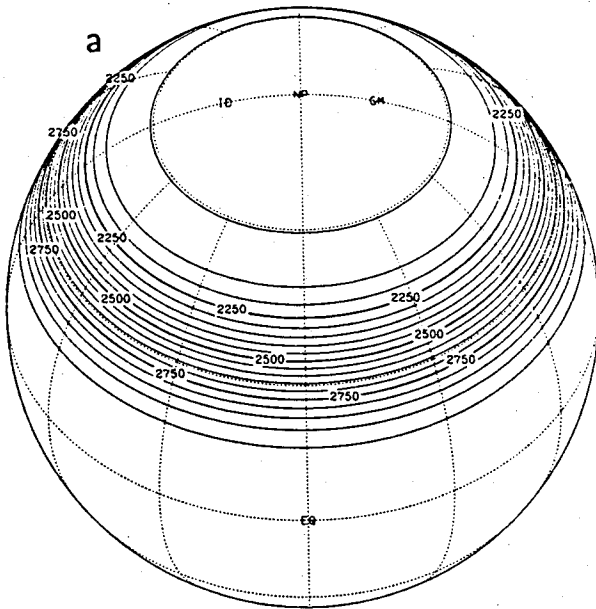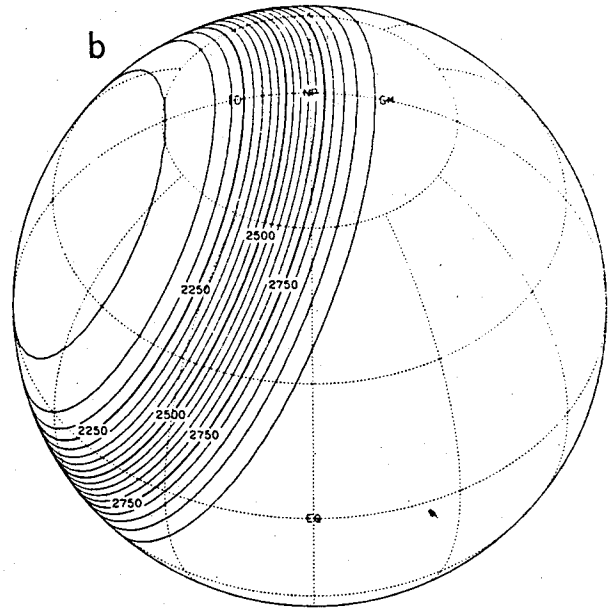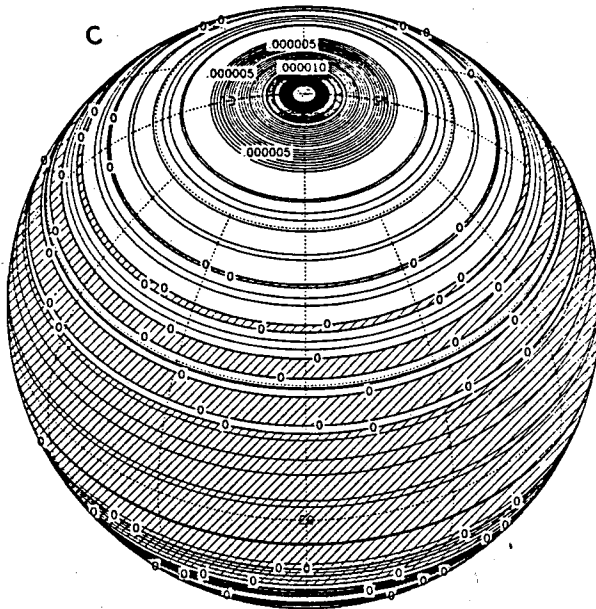
Figure 3.1 l_1, l_2, and l_∞ height errors (a–c) and l_1, l_2, and l_∞ wind errors (d–f) for test case 3. Wide solid line for T42, $\alpha = 0$, dashed line for T42, $\alpha = \pi/3$ and narrow solid line for T63, $\alpha = \pi/3$.
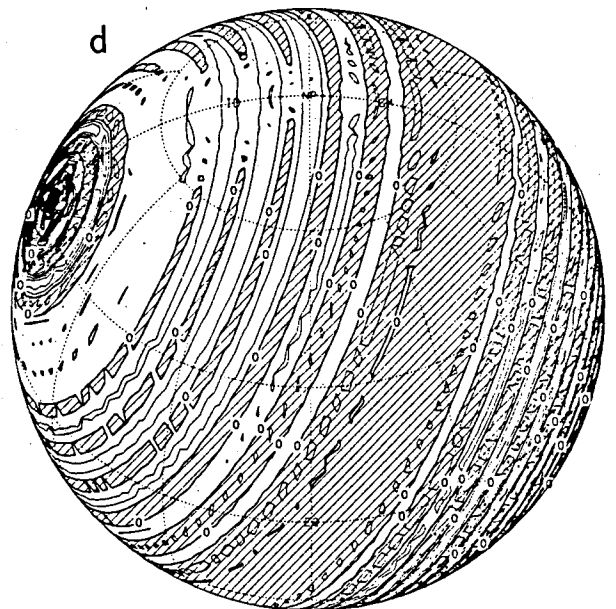
a

CONTOUR FROM 2100 TO 2950 BY 50
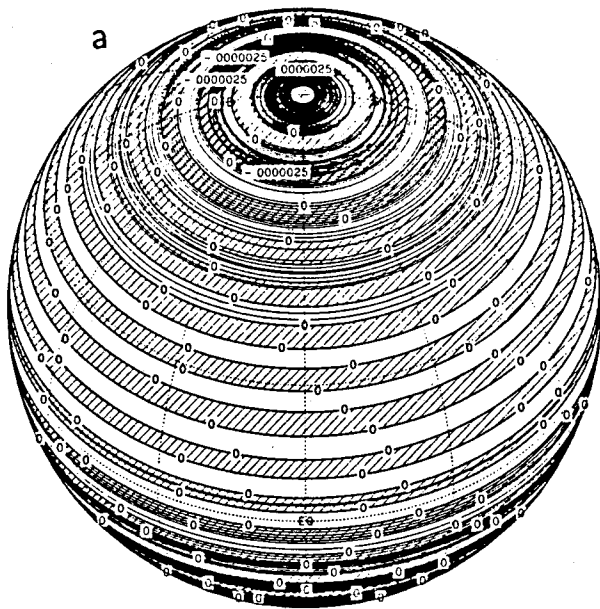
b

CONTOUR FROM 2100 TO 2950 BY 50

c

CONTOUR FROM -.000002 TO .00002 BY .000001
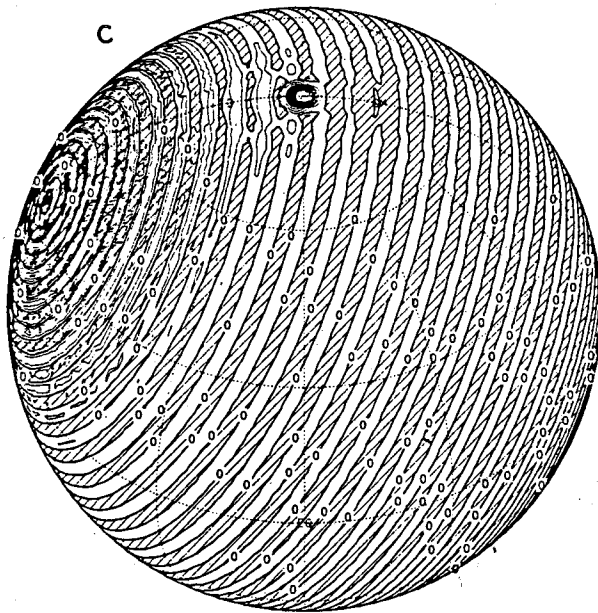
d

CONTOUR FROM -.000008 TO .00002 BY .000001

Figure 3.2 Analytic height field for (a) $\alpha = 0$, (b) $\alpha = \pi/3$. Contour interval is 50 m. Height error at day 5 from T42 case for (c) $\alpha = 0$, (d) $\alpha = \pi/3$. Contour interval is 1×10^{-6} m. All plotted on an orthographic projection centered on 90W, 45N of the representional coordinates.

CONTOUR FROM -.0000045 TO .000004 BY .0000005
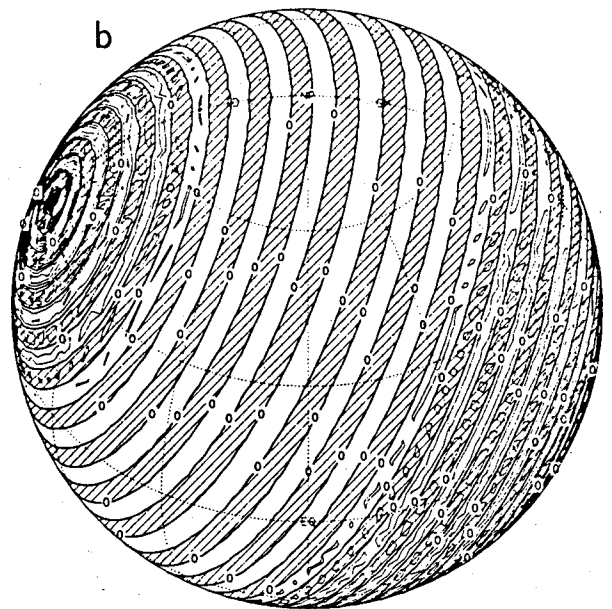
CONTOUR FROM -.000005 TO .000011 BY .000001

CONTOUR FROM -8×10⁻⁹ TO 6×10⁻⁹ BY 0.5×10⁻⁹
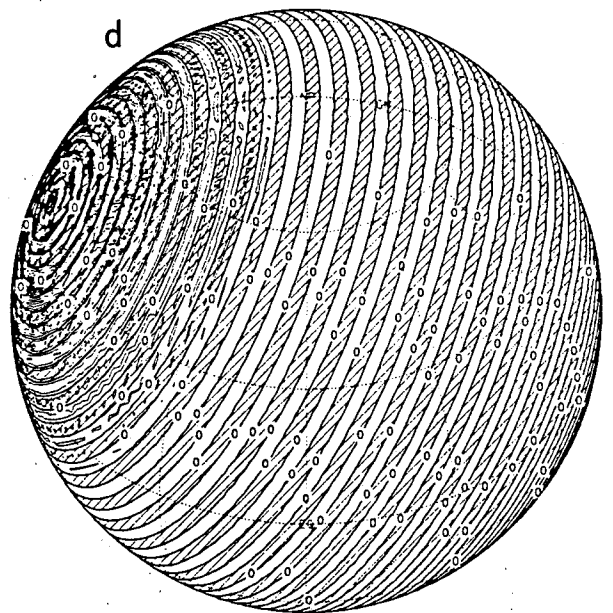
CONTOUR FROM -3.2×10⁻⁹ TO 3.6×10⁻⁹ BY 0.4×10⁻⁹

Figure 3.3 Height error at day 0 after spectral truncation from T42 case for (a) $\alpha = 0$, (b) $\alpha = \pi/3$. Contour intervals are (a) 5 x 10^{-7} and (b) 1 x 10^{-6}. Height error at day 0 after spectral truncation from T63, $\alpha = \pi/3$ case for (c) normal precision, (d) double precision latitude Gaussian weights and polynomials. Contour intervals are (c) 5 x 10^{-9} and (d) 4 x 10^{-9}.

26

4. Forced Nonlinear System with a Translating Low

This test case presents more of a challenge to the spectral scheme in terms of representing the initial state and analytic forcing. The horizontal scales of both the initial state and the forcing are considerably more complex than in the earlier test cases, and are less accurately represented with comparable spectral truncations. This truncation error can be seen in all the error measures at $t = 0$. The l_1, l_2, and l_∞ error for the initial height field are illustrated in Figure 4.1 (left to right in each grouping) as a function of four horizontal truncations for the $u_0 = 20 m/sec$ case. This figure shows that even though the solution is reasonably well represented at T42, a modest improvement in horizontal resolution can yield significantly better results. A curious behavior is seen for the T106 truncation where all error estimates are worse than at T63. This is a consequence of the degree to which the basis functions are orthonormal, as previously discussed in some detail in Section 2. For all practical purposes, the representation has converged to machine accuracy at T63.

Figures 4.2 and 4.3 show the initial height and wind fields for the u_0=20 (top panel) and u_0=40 m/sec (bottom panel) cases. Figures 4.4 and 4.5 show the corresponding height and wind errors at day 5.

Figure 4.6 presents the error norms for the two cases. The high frequency temporal noise appearing in the various error measures occurs because the initial data have not been properly initialized; i.e., the mass and momentum fields have been specified independently and the corresponding truncation errors result in small imbalances contributing to gravity-wave activity. Another important source of this noise arises from discrete sampling of the solution on the Gaussian grid.

The l_1 error in the height field grows rapidly during the first day of integration, after which it grows monotonically but at less than 1/10th the initial rate. A similar, although less exaggerated behavior is seen in the l_1 wind error. The growth in these error curves is predominantly attributable to time truncation error, although in the early stages of the integration it is also associated with the geostrophic adjustment process. For example, during the period of rapid l_1 error growth, the l_∞ error shows a rapid decrease followed by a rebound as the slowly forced mass and momentum fields come into a consistent internal balance.

As mentioned above, the error is dominated by the time truncation component. In T42 integrations with the discrete time step halved (not shown), the growth in all error estimates is reduced by nearly a factor of four. Integrations using a T63 truncation but the same time step as for T42 truncation produce remarkably similar results in the global error estimates, although the detailed structure of the errors is noticeably different. The maximum departures are in the vicinity of the translating low pressure cell.

The l_2 and l_∞ errors in both the height and wind field generally show a monotonic increase in time after the initial adjustment, but begin to exhibit signs of an oscillation

after about 4 days. This behavior is most apparent in the $u_0=40$ m/s case, for which all the error estimates are systematically larger than the $u_0=20$ m/s case (another indication of the dominance of time truncation error). We believe that this behavior is attributable to secondary nonlinearities associated with the growing inconsistency between the evolving state and the analytically specified forcing, seen initially as a phase error. One would expect this type of behavior to be more pronounced in the case of larger departures of the simulated state from the analytic state, which is the case for $u_0=40$ m/s.
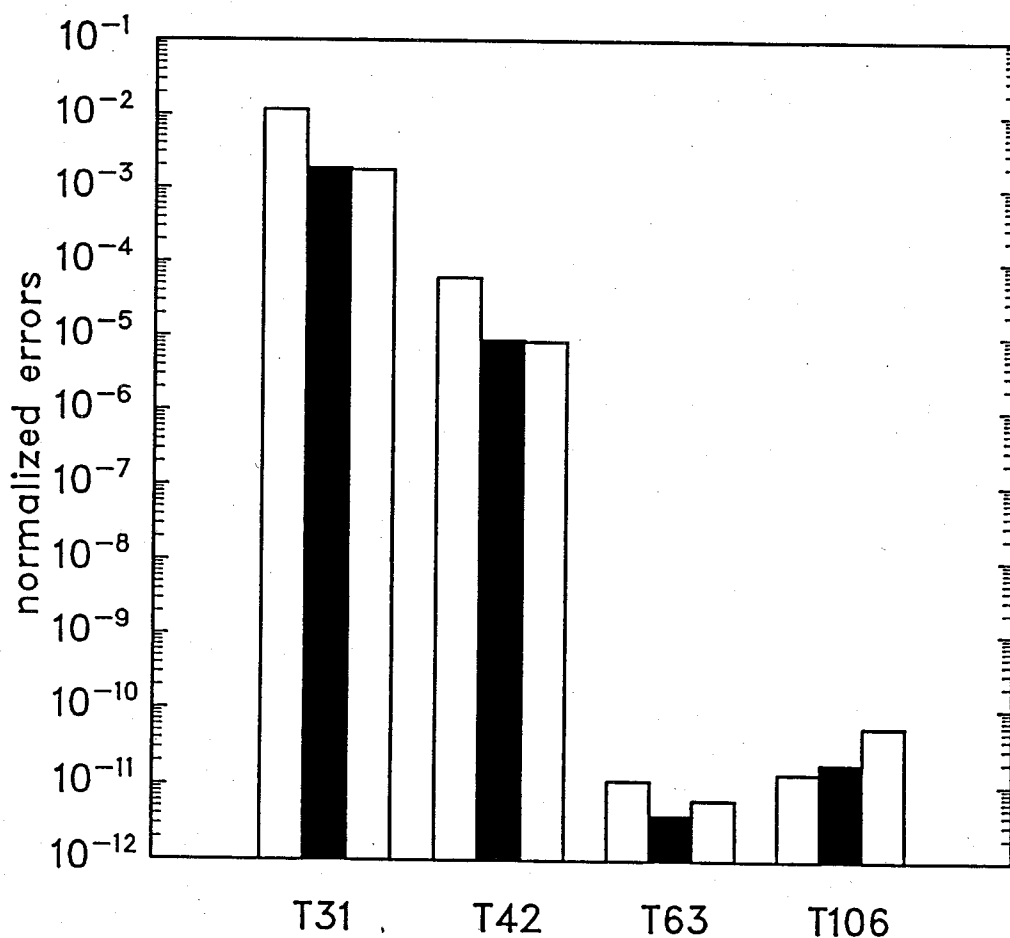
Figure 4.1 Initial normalized height errors for Test Case 4 as function of resolution. Each grouping shows l_1, l_2, and l_∞, from left to right.

CONTOUR FROM 10100 TO 10625 BY 25

CONTOUR FROM 10200 TO 11100 BY 50
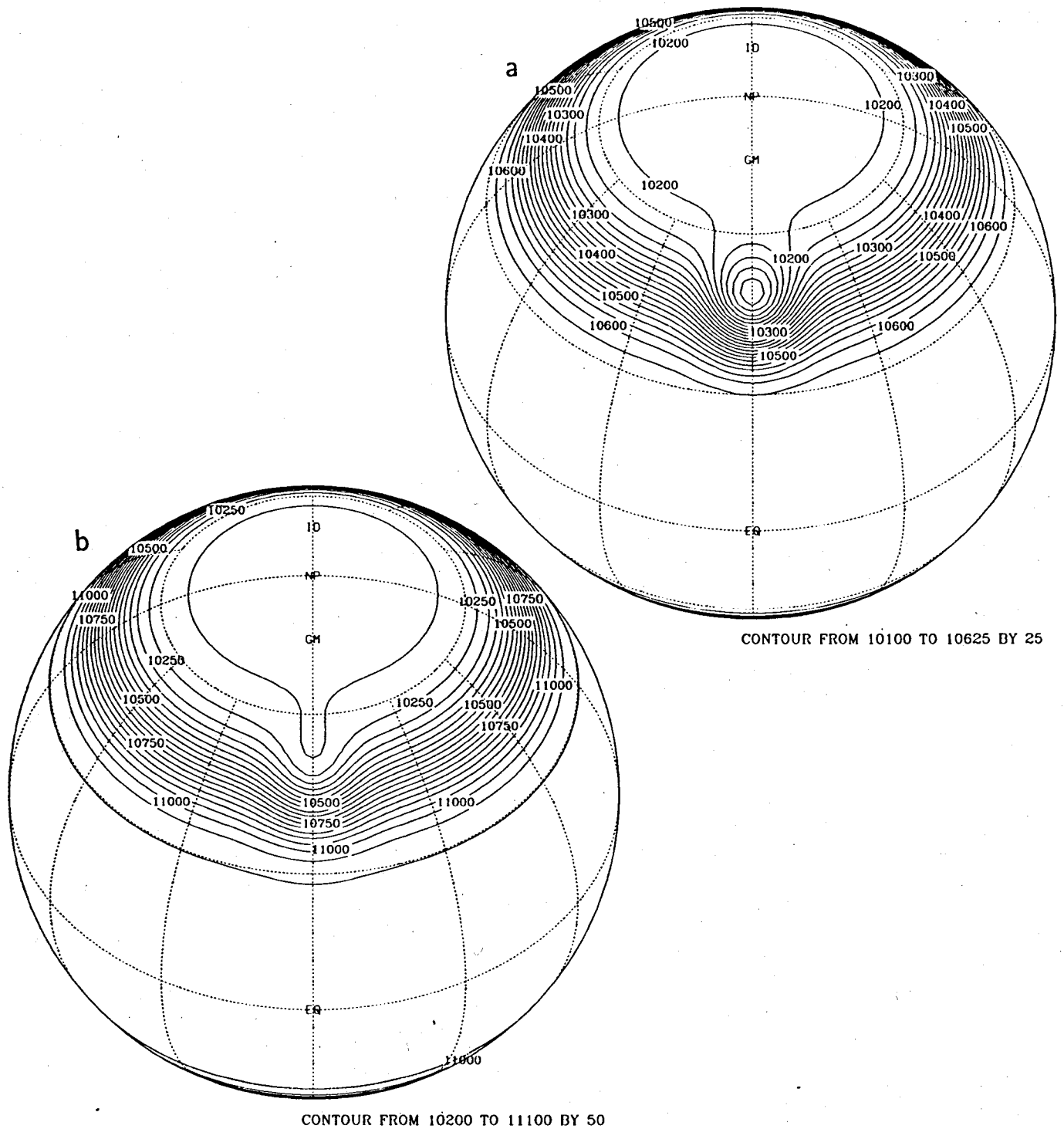
Figure 4.2 Initial height field for (a) $u_0 = 20$ m/sec and (b) $u_0 = 40$ m/sec plotted on an orthographic projection centered at 45N and the longitude of the trough of the analytic solution. Contour intervals are (a) 25 m and (b) 50 m.
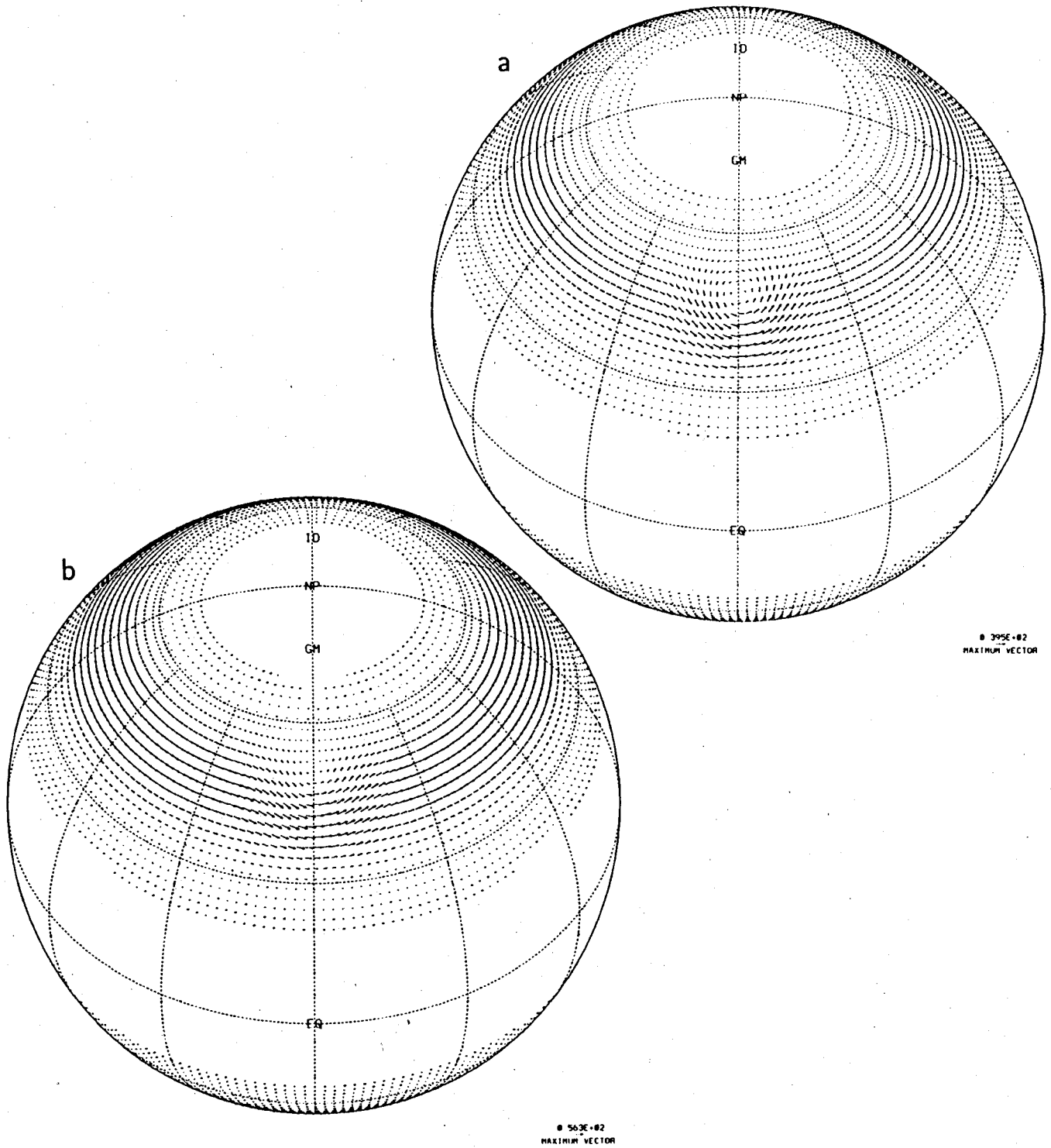
Figure 4.3 Initial wind field for (a) $u_0 = 20$ m/sec and (b) $u_0 = 40$ m/sec plotted on an orthographic projection centered at 45N and the longitude of the trough of the analytic solution.

CONTOUR FROM -.48 TO .16 BY .04

CONTOUR FROM -2.2 TO 1 BY .2
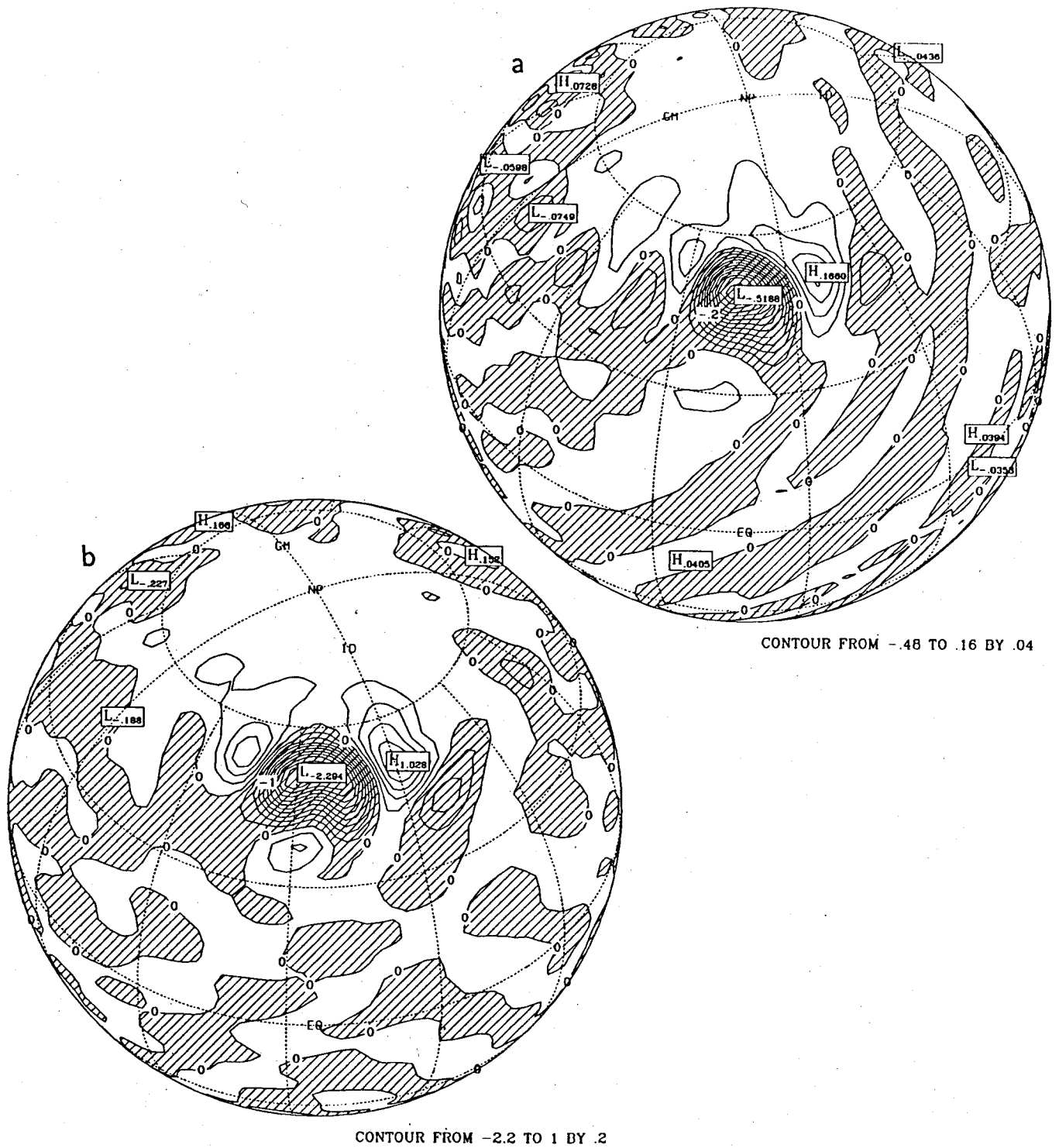
Figure 4.4 Height errors at day 5 from T42 case for (a) $u_0 = 20$ m/sec and (b) $u_0 = 40$ m/sec plotted on an orthographic projection centered at 45N and the longitude of the trough of the analytic solution. Contour intervals are (a) 0.04 m and (b) 0.2 m.
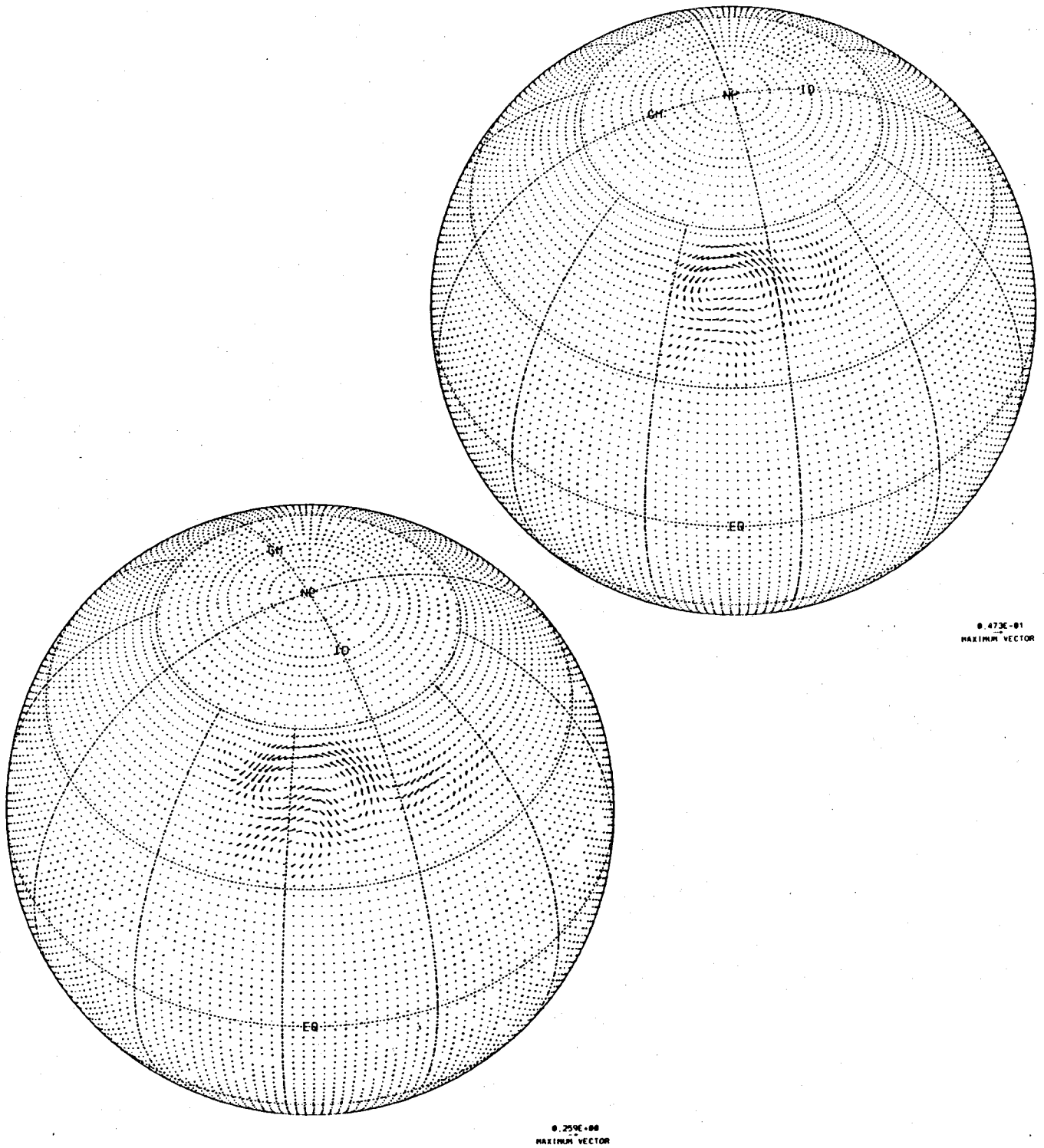
Figure 4.5 Wind errors at day 5 from T42 case for (a) $u_0 = 20$ m/sec and (b) $u_0 = 40$ m/sec plotted on an orthographic projection centered at 45N and the longitude of the trough of the analytic solution.
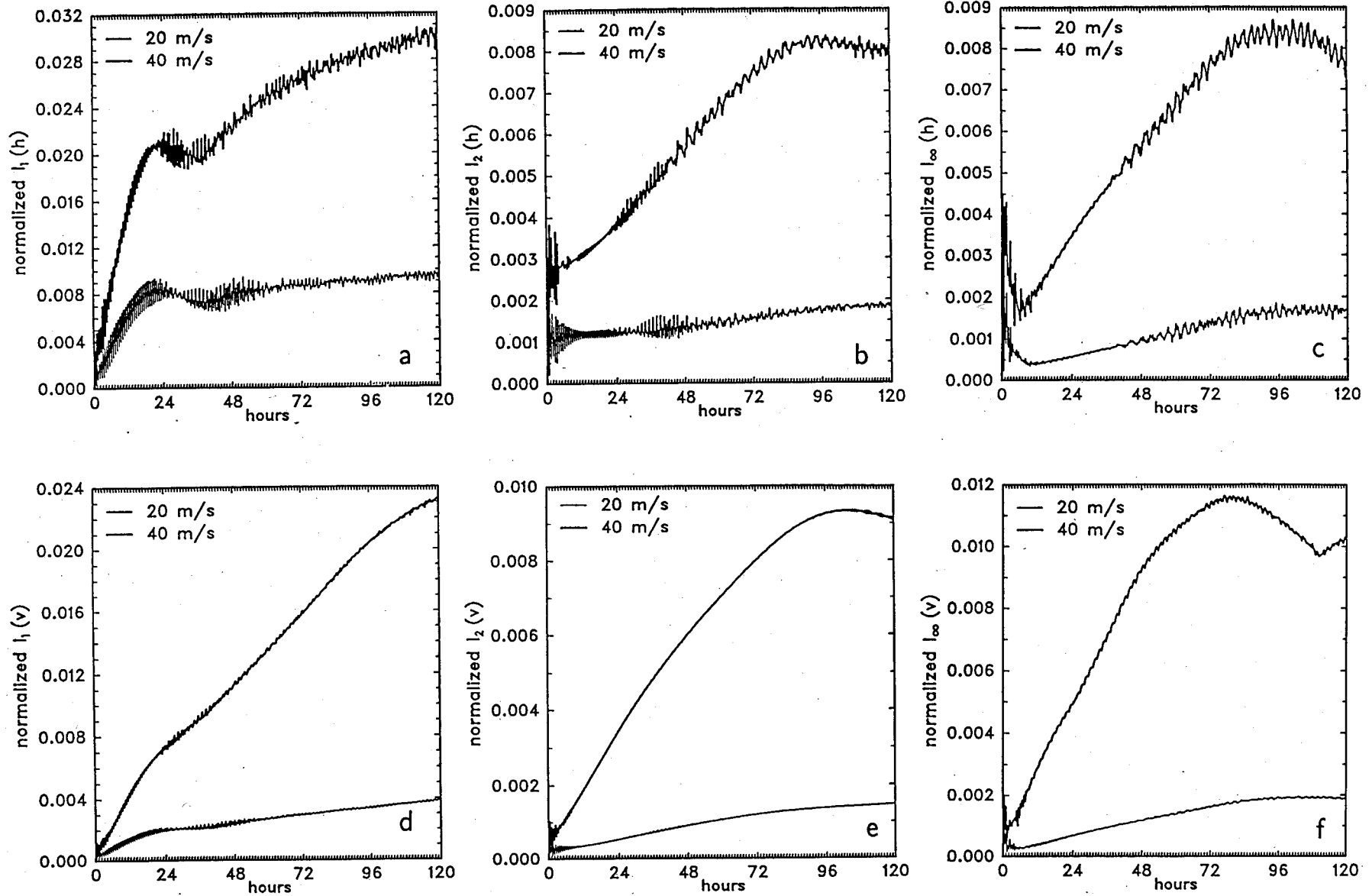
Figure 4.6 $l_1, l_2,$ and l_∞ height errors (a–c) and $l_1, l_2,$ and l_∞ wind errors (d–f) for T42 case for $u_0 = 20$ and 40 m/sec.

33

5. Zonal Flow over an Isolated Mountain

This test case consists of the zonal flow in Case 2 impinging on a mountain. Although the wind and height field are the same as for $\alpha = 0$ in Case 2, the height h_0 is changed to 5960 m. The surface or mountain height is given by

$$h_s = h_{s_0}(1 - r/R)$$

where $h_{s_0} = 2000$ m, $R = \pi/9$ and $r^2 = \min[R^2, (\lambda - \lambda_c)^2 + (\theta - \theta_c)^2]$. The center is taken as $\lambda_c = 3\pi/2$ and $\theta_c = \pi/6$. A qualitative sense for the horizontal scale and location of the mountain feature can be gleaned from the error estimates shown in Figures 5.2 b and d, which are discussed later in this section.

Because there is no analytic solution, this case is in the same class as Test Cases 6 and 7, which follow. For each of these test cases, we use a high resolution integration of the spectral model to generate a reference solution. The various model configurations, including the configuration used for the reference solution, is consistent with the way the model would be configured in real applications. An explicit linear horizontal diffusion term is included to deal with the effects of spectral blocking, as discussed in Appendix A. In practice, the magnitude of the diffusion coefficient increases with lower spectral truncation meaning that the rate of internal dissipation is not necessarily the same for each of the resolutions presented. The time step selected is determined according to the particular horizontal truncation where lower resolution integrations may make use of longer time steps. Thus, the results contain a mix of factors (e.g., time truncation, space truncation, etc.) contributing to differences with the high resolution reference solution. We will qualitatively discuss the relative roles of various sources of "error" when possible. Our principal focus, however, will be on the net error since the various examples are configured as they would be in practical meteorological applications.

The representation of the mountain height and thus the depth of the fluid for this test case is a challenge for the spectral scheme at all resolutions. Significant fluid depth errors occur initially in the vicinity of the mountain. These rapidly translate into local errors in the height of the fluid which are comparable in order of magnitude to the downstream errors which form during the integration. The height field for the T213 reference solution truncated to T106 (the resolution at which the reference solution is archived) and plotted on the T63 Gaussian grid (for direct comparison with the T63 results) is shown in Figure 5.1a–d for the initial state, day 5, day 10, and day 15, respectively. These results show a rapid evolution from a meridionally smooth zonally symmetric flow to an irregular high wavenumber state by day 15. Note the evidence of "spectral ringing" in the solution near the imposed mountain (i.e., upstream from the mid-latitude northern hemisphere trough). Simulation using T42 and T63 truncation are compared with this reference solution. The detailed solutions and differences with the reference solution are presented in Figure 5.2

for day 15. The upper row contains the T42 results, the lower row the T63 plots. Subjective inspection of the solutions after 15 days suggests remarkable agreement between the reference solution and the T63 results. The T42 results appear to be almost as good with evidence of more severe spectral representation problems in the vicinity of the mountain. Nevertheless, the location and magnitude of the major flow features are very accurately captured. The difference maps clearly show the problems that each of the lower resolution models has in representing the solution over the imposed mountain. Away from this region, however, the structure and magnitude of the error field are quite similar, even after 15 days.

This subjective characterization of the low resolution solutions is evidenced by most all of the global error estimates illustrated in Figure 5.3. All error measures exhibit rapid increases during the first few days as the fluid system adjusts to the initially large imbalances (with respect to the reference solution) attributable to the accuracy with which the mountain feature can be resolved. This adjustment is illustrated most clearly in the $l_\infty(v)$, suggesting a larger adjustment of the momentum field toward the mass field which would be expected at these scales and mean fluid depth (Rossby, 1939, Matsumoto, 1961). Note that these data are sampled daily, making it difficult to ascribe significance to the variability exhibited in the latter part of the integrations (i.e., this may be nothing more than a consequence of the sampling interval). In general, after the initial adjustment is complete, the global error estimates show a relatively small increasing trend with the T63 error estimates modestly smaller than the T42 results.

Global integrals of mass, energy, and potential enstrophy, as a function of time, are shown in Figure 5.4. Both resolutions exhibit comparable systematic increases in mass during the course of the integration, which is of the same order as machine rounding. Total energy and potential enstrophy drop off as a consequence of internal dissipation, with expectedly larger dissipation in the lower resolution result. The unnormalized integrals of relative vorticity and divergence, shown in Figure 5.5, are reasonably well maintained (i.e., order machine roundoff), but begin to exhibit signs of a slowly increasing oscillation after about 20 days (not shown).

a

CONTOUR FROM 5000 TO 5950 BY 50

b

CONTOUR FROM 5000 TO 5950 BY 50

c

CONTOUR FROM 5050 TO 5950 BY 50

d

CONTOUR FROM 5050 TO 5950 BY 50
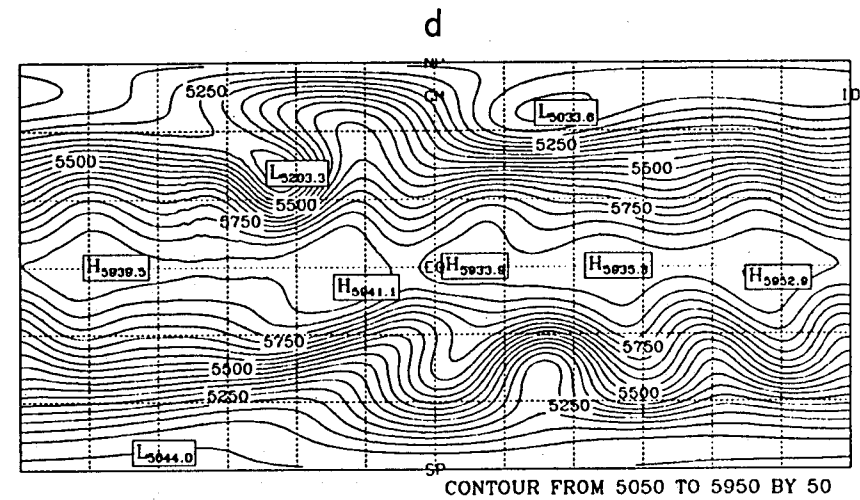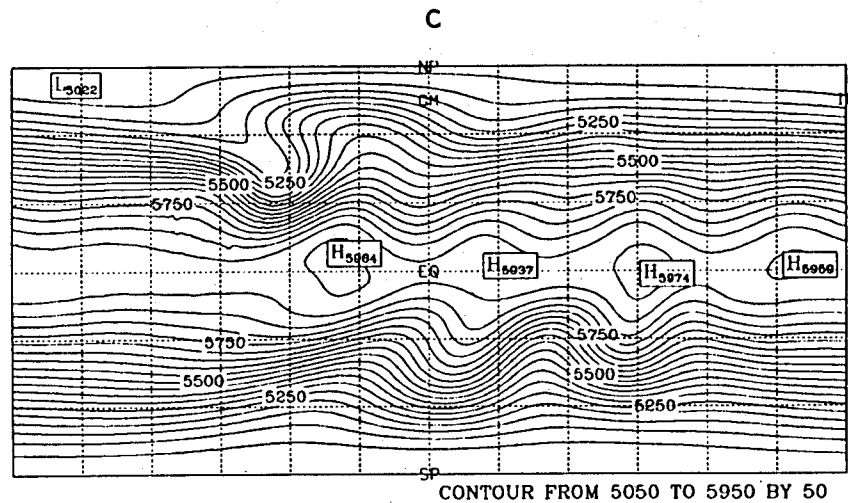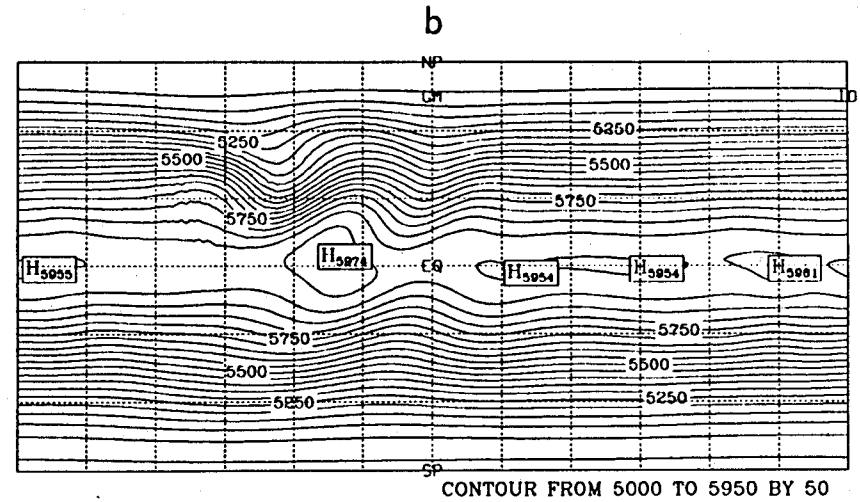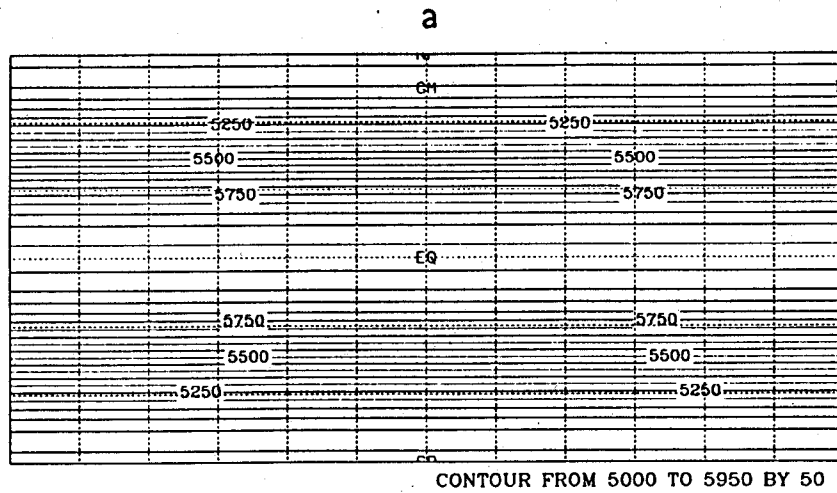
Figure 5.1 T213 reference height solution for Test Case 5 at (a) day 0, (b) day 5, (c) day 10, and (d) day 15 on a cylindrical equidistant projection. Contour interval is 50 m.

a

CONTOUR FROM 5050 TO 5900 BY 50

b

CONTOUR FROM −30 TO 70 BY 5

c

CONTOUR FROM 5050 TO 5900 BY 50

d

CONTOUR FROM −27.5 TO 25 BY 2.5
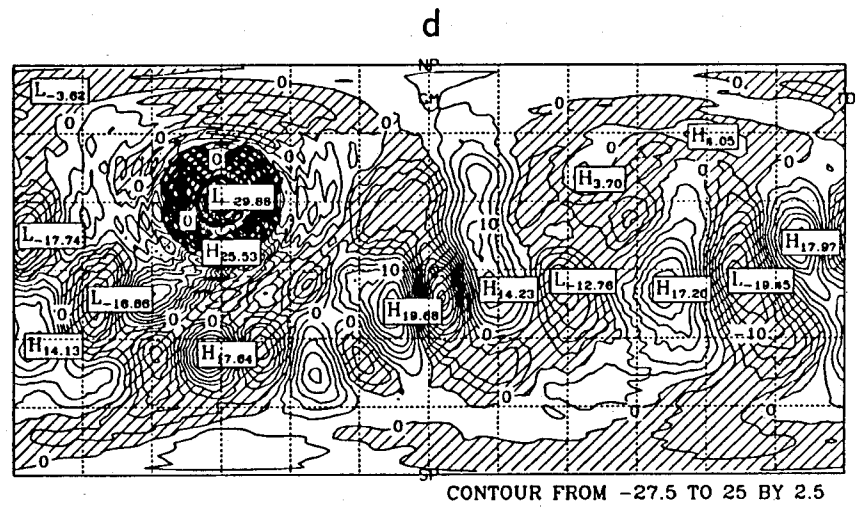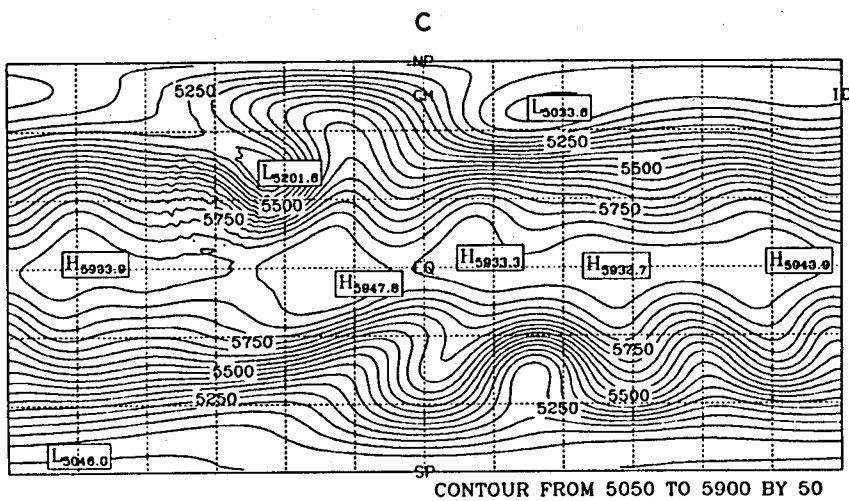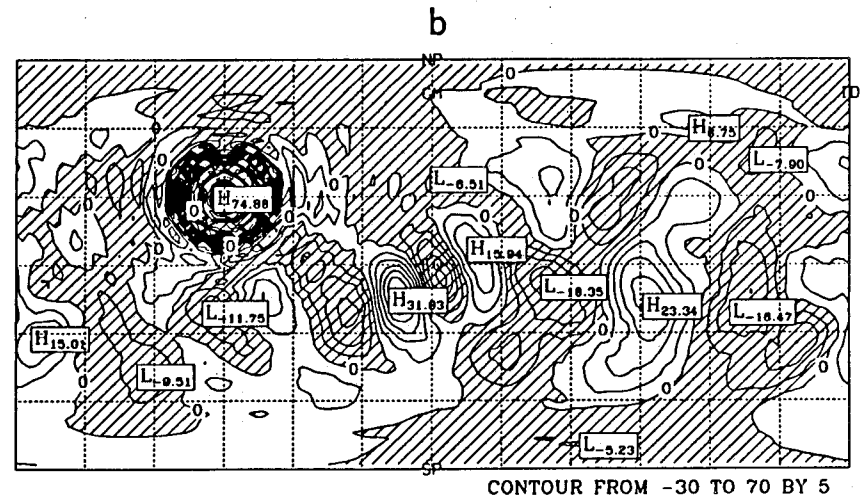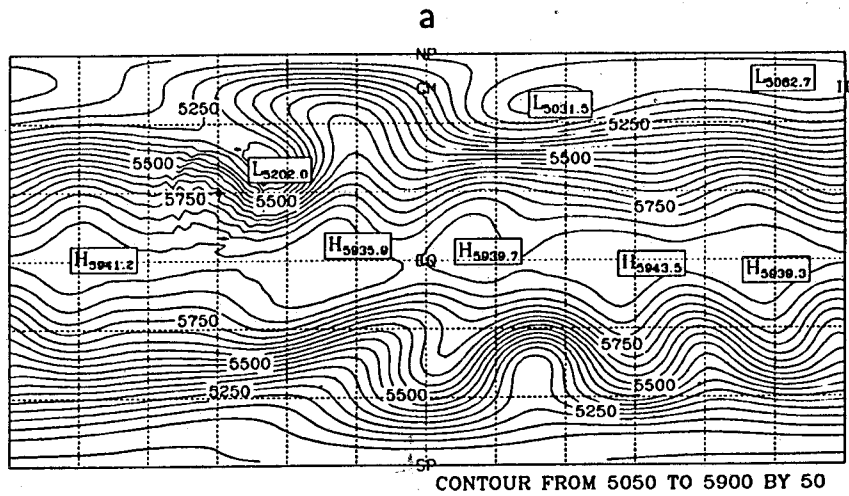
Figure 5.2 Height fields at day 15 for (a) T42 and (c) T63 and differences with reference solution for (b) T42 and (d) T63. Contour intervals are (a) 50 m, (c) 50 m, and (d) 2.5 m.
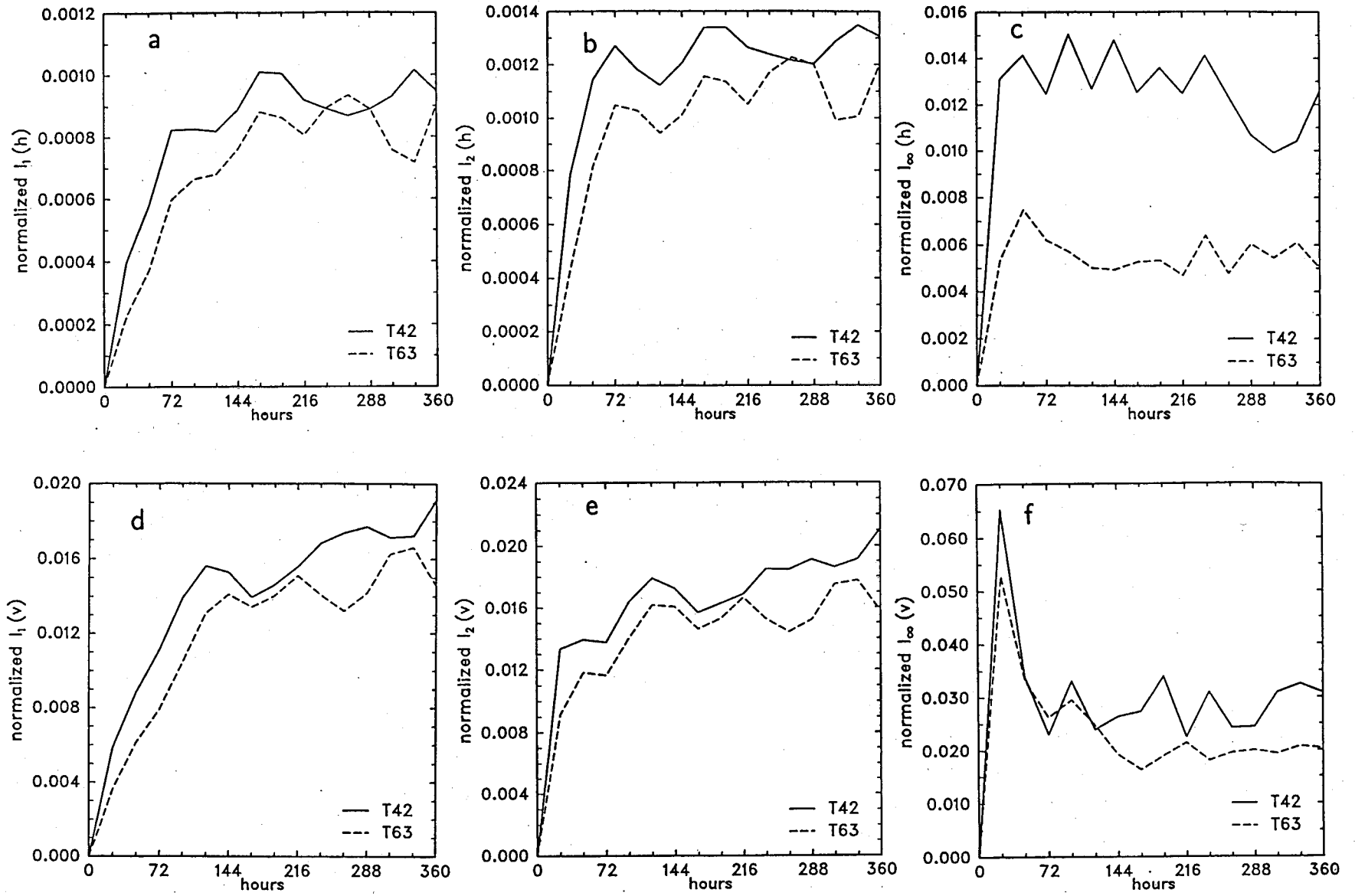
Figure 5.3 l_1, l_2, and l_∞ height errors (a–c) and l_1, l_2, and l_∞ wind errors (d–f) for T42 and T63 cases.
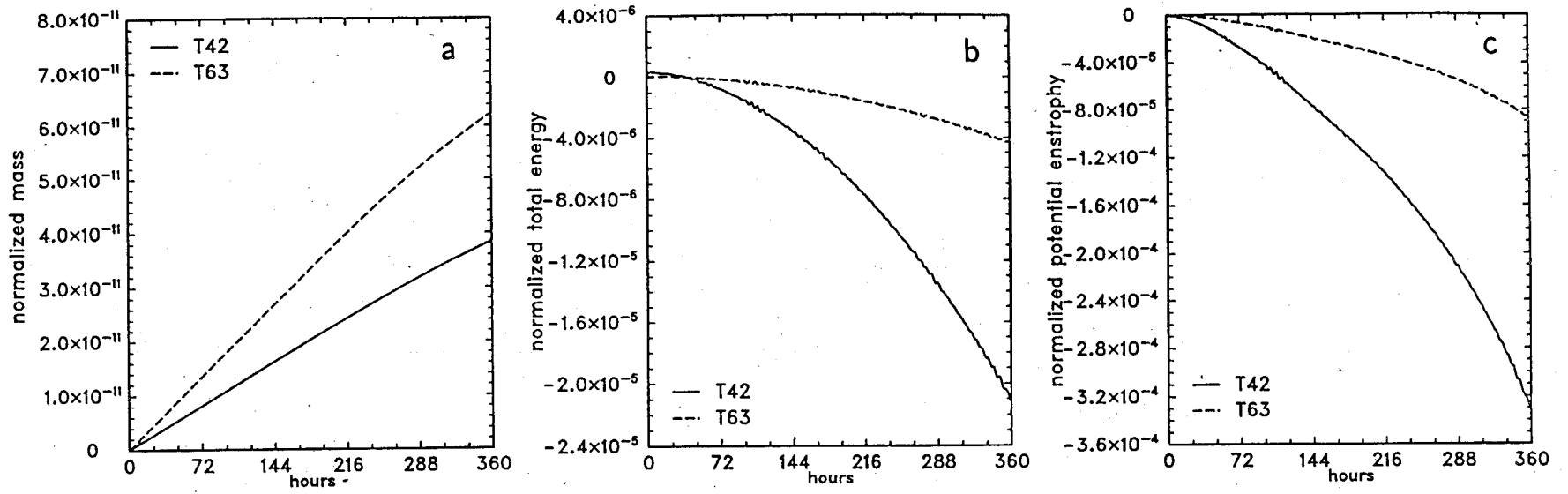
Figure 5.4 Global integrals of (a) mass, (b) energy, and (c) potential enstrophy for T42 and T63 resolutions.
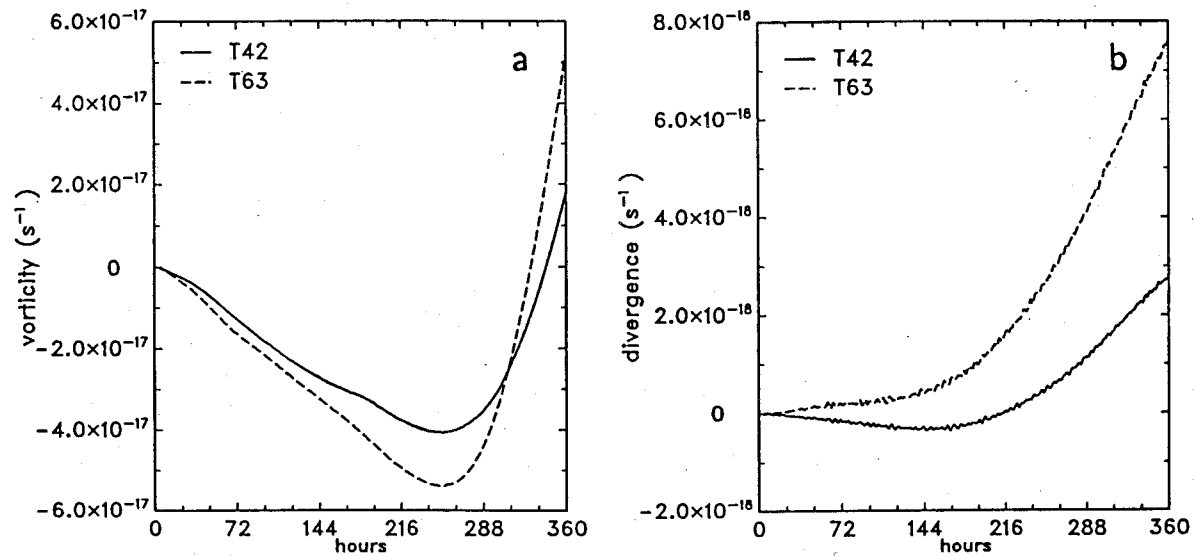
Figure 5.5 Global integrals of (a) vorticity and (b) divergence for T42 and T63 resolutions.

6. Rossby-Haurwitz Wave

Rossby-Haurwitz waves are an ideal test of numerical solutions of the nonlinear barotropic vorticity equation, since they represent exact analytic solutions. They are not closed form solutions for the divergent barotropic system, however, and thus cannot be regarded as a rigorous test for the correct numerical solution of this system of equations. Nevertheless, they are a frequently used meteorological test and have been included in the test case suite for this reason.

Because no analytic solution is known, we use a high resolution integration of the spectral model to generate a reference solution. As mentioned in the previous section, the results contain a mix of factors (e.g., time truncation, space truncation, etc.) contributing to differences with the high resolution reference solution. We will qualitatively discuss the relative roles of various sources of "error" when possible. Our principal focus, however, will be on the net error results since the model for the basic experiments is configured as it would be in practical meteorological applications.

The representation of the initial condition for this test case is not a challenge to the spectral scheme. As the solution evolves, however, the impact of horizontal resolution becomes more apparent since the flow field does not maintain its initial structure. Figure 6.1a–d shows the height field for the T213 reference solution truncated to T106 and plotted on the T63 Gaussian grid for the initial state, day 1, day 7, and day 14, respectively. The time step for this integration is 180 seconds which is smaller than the default listed in the introduction (due to very strong winds associated with this test case), while the horizontal diffusion coefficient $K_4 = 8 \times 10^{12} m^4/s$ is the default value. As can be seen in these maps, there is a noticeable tendency for some sharpening of the mid-latitude troughs in the solution with a hint of some erosion of the tropical ridges. As mentioned earlier, the "errors" associated with the lower resolution integrations are a consequence of horizontal and spatial truncation errors, as well as the choice of the linear horizontal diffusion coefficent. To help quantify the role of horizontal diffusion in the high-resolution T213 reference solution, the diffusion term was eliminated in a second high-resolution integration. The $l_2(h)$ difference in the two solutions is shown in Figure 6.2. This measure illustrates that the first five days are essentially unaffected by the diffusion. After 14 days, this term leads to only a 0.08% $l_2(h)$ difference in the solution, and clearly plays a minor role in the reference solution results.

Figures 6.3 to 6.5 show solutions of the height field for T42 (top) and T63 (bottom), along with the differences from the high-resolution reference solution at day 1,7 and 14. The global error norms are shown in Figure 6.6. The T42 and T63 used time steps of 600 and 450 seconds, respectively. The diffusion coefficients were $5 \times 10^{15} m^4/s$ and $1 \times 10^{15} m^4/s$ respectively. At each of the two resolutions we see similar structures in the error field with a general erosion of zonal and meridional gradients that increases with lower resolution. In

general, the T63 errors are about half the size of the errors exhibited by the T42 integration. In each case, the phase of the wave structure is very well represented.

With regard to conservation properties (Figures 6.7 - 6.8) the T42 and T63 models do reasonably well. Both resolutions exhibit a comparable systematic relative increase in mass during the course of the integration which is of the same order as machine rounding. Total energy and potential enstrophy drop off as a result of internal dissipation, with proportionally larger dissipation in the lower resolution result. The unnormalized integrals of relative vorticity and divergence are reasonably well maintained (i.e., order machine roundoff).

Integration of the T42 and T63 models with a 180 second time step suggests that time truncation is playing some role in the detailed structure of the error. The height fields and differences with the T213 reference solution are shown in Figure 6.9 for the T42 run with 180 second time step at days 7 (top) and 14 (bottom). Comparison with Figures 6.4 and 6.5 shows the sensitivity to time step. The general characteristics of the global error estimates (not shown) are not affected by the time step, however, the details are. For example, the initial growth is a little slower, but the same plateau is reached around hours 144 to 240 followed by the rapid growth to the same level at hour 336. Thus the results are dominated primarily by spectral truncation and internal dissipation.

The effect of horizontal diffusion is seen in Figure 6.10, which shows the T42 solution with no diffusion and a 600 sec time step at days 7 (top) and 14 (bottom). The character of the error is noticeably different compared to Figure 6.5 at day 14.

Finally, we have selected wave number 4 for this test case because it is empirically known to be a stable solution to the equations. Thus small perturbations introduced by truncation error should not grow so rapidly in 14 days so as to produce a solution dominated by any particular perturbations introduced. However, since the flow structure does not maintain itself, as in the nondivergent barotropic system, and since the change in structure is a function of the horizontal resolution, one might ask how long the initial solution should be expected to remain stable. To address this question we have integrated the T42 model with diffusion and the 600 sec time step for a period of 60 days. The height field is shown in Figure 6.11a and b for day at 30 and 60, respectively. Clearly, the pattern maintains its basic wave number 4 structure throughout this period while the details of the pattern change. Consequently, it is quite reasonable to assume that the true solution is nowhere near the point of breaking down at the end of the 14 day integration period selected for the test case, and viable numerical methods should be able to maintain the wave number 4 structure for the 14 day period at a minimum.

a

CONTOUR FROM 8100 TO 10500 BY 100

b

CONTOUR FROM 8100 TO 10500 BY 100

c

CONTOUR FROM 8300 TO 10500 BY 100

d

CONTOUR FROM 8100 TO 10500 BY 100
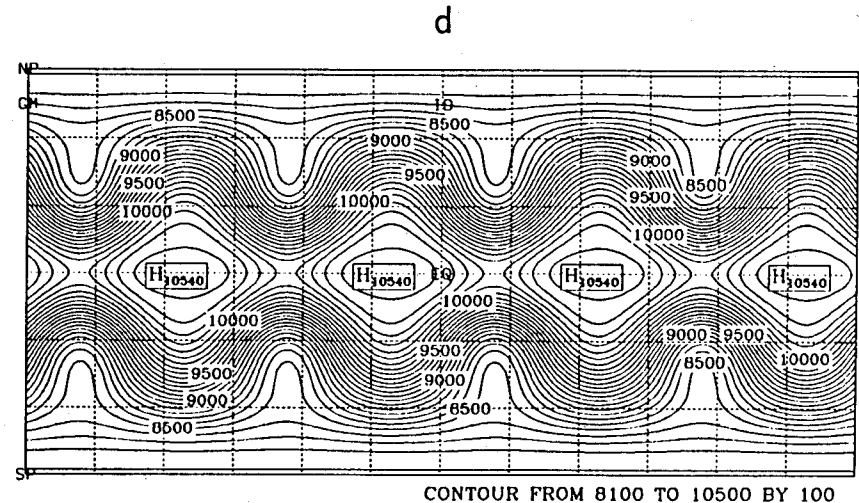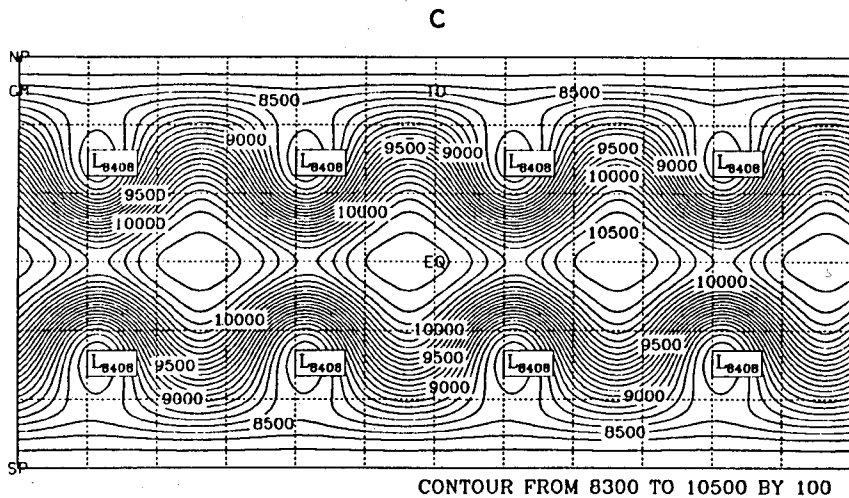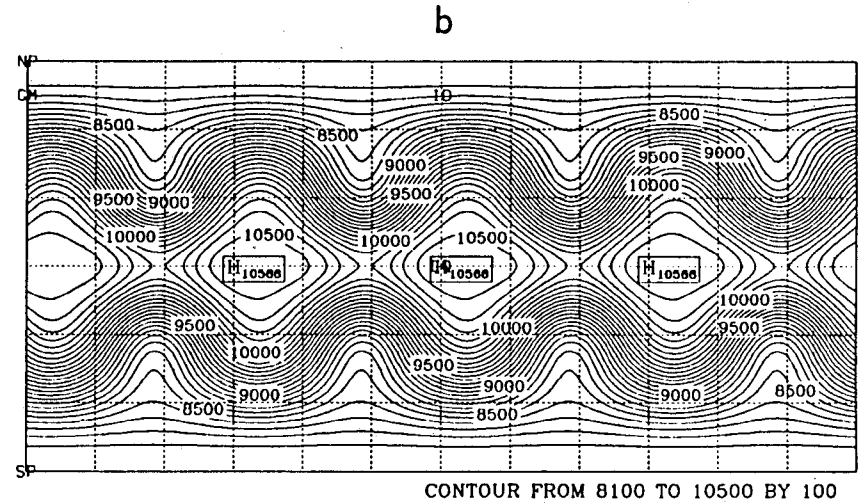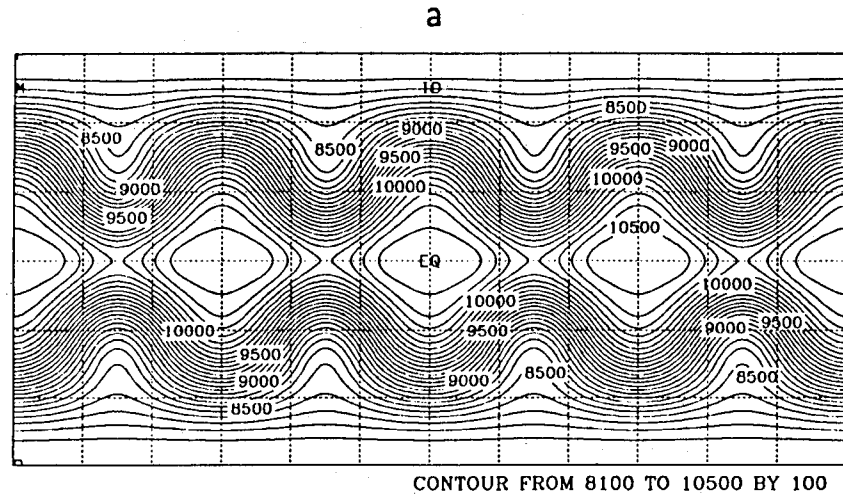
Figure 6.1 T213 reference height solution for Test Case 6 at (a) day 0, (b) day 1, (c) day 7, and (d) day 14 on a cylindrical equidistant projection. Contour interval is 100 m.
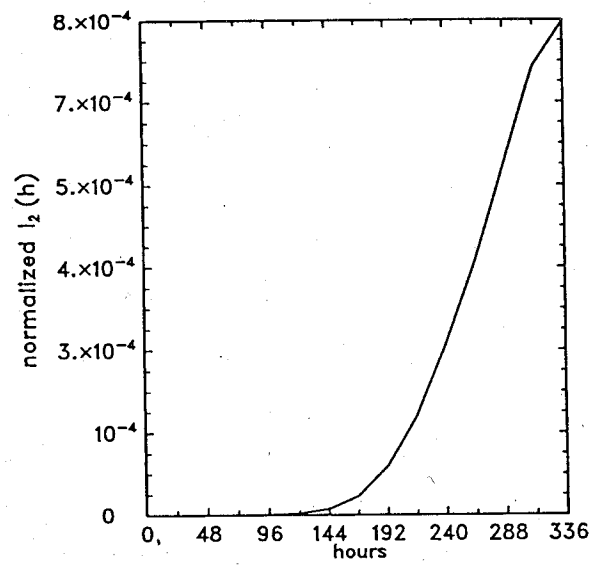
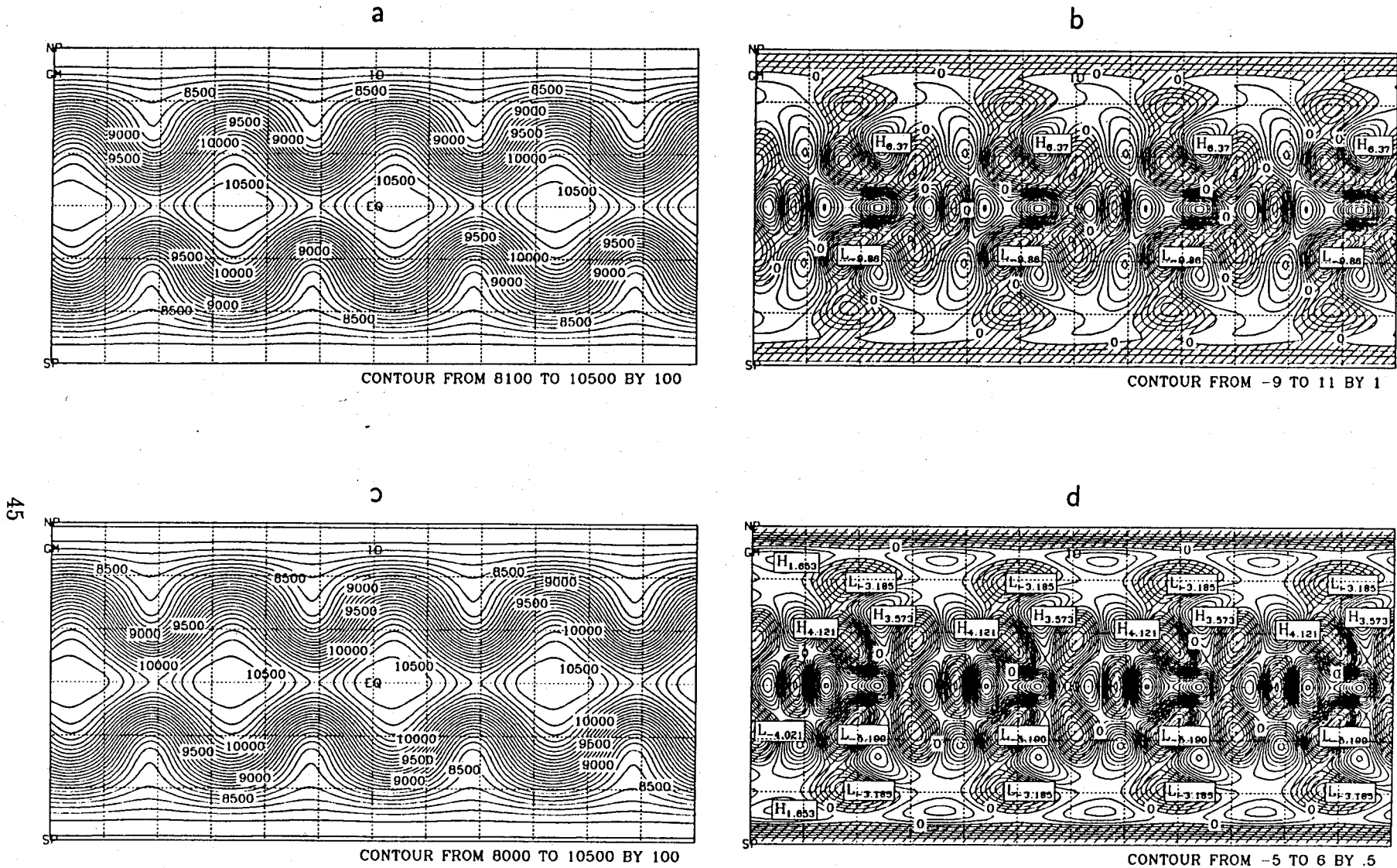Figure 6.2 l_2 height difference for T213 integration with and without diffusion.

a

CONTOUR FROM 8100 TO 10500 BY 100

b

CONTOUR FROM −9 TO 11 BY 1

c

CONTOUR FROM 8000 TO 10500 BY 100

d

CONTOUR FROM −5 TO 6 BY .5

Figure 6.3 Height fields at day 1 for (a) T42 and (c) T63 and differences with reference solution for (b) T42 and (d) T63. Contour intervals are (a) 100 m, (c) 100 m, (b) 1 m and (d) 0.5 m.

a

CONTOUR FROM 8300 TO 10500 BY 100

b

CONTOUR FROM −40 TO 40 BY 5

c

CONTOUR FROM 8300 TO 10500 BY 100

d

CONTOUR FROM −15 TO 27.5 BY 2.5
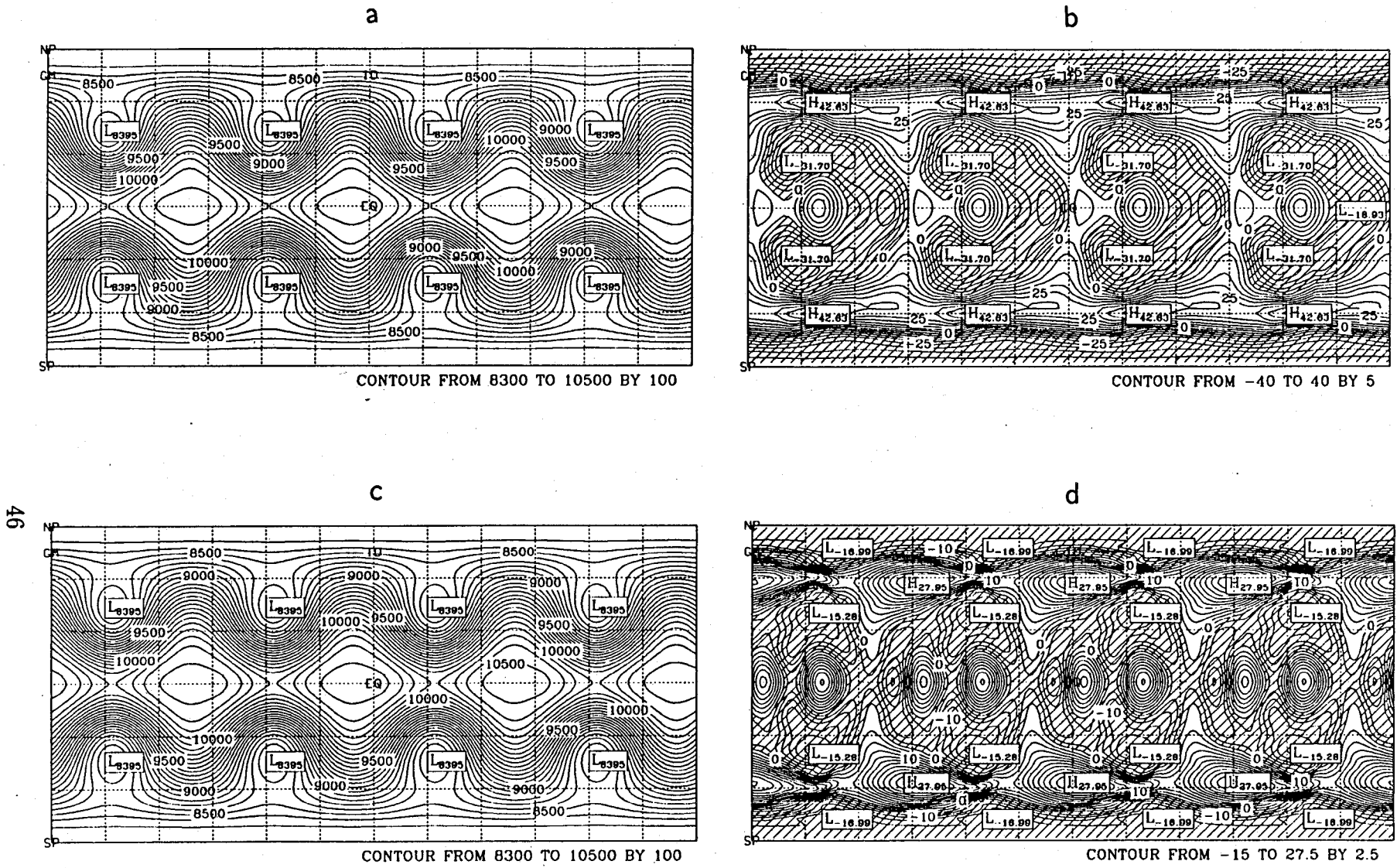
Figure 6.4 Height fields at day 7 for (a) T42 and (c) T63 and differences with reference solution for (b) T42 and (d) T63. Contour intervals are (a) 100 m, (c) 100 m, (b) 5 m, and (d) 2.5 m.

a

CONTOUR FROM 8200 TO 10500 BY 100

b

CONTOUR FROM −90 TO 120 BY 10

c

CONTOUR FROM 8200 TO 10500 BY 100

d

CONTOUR FROM −50 TO 60 BY 5
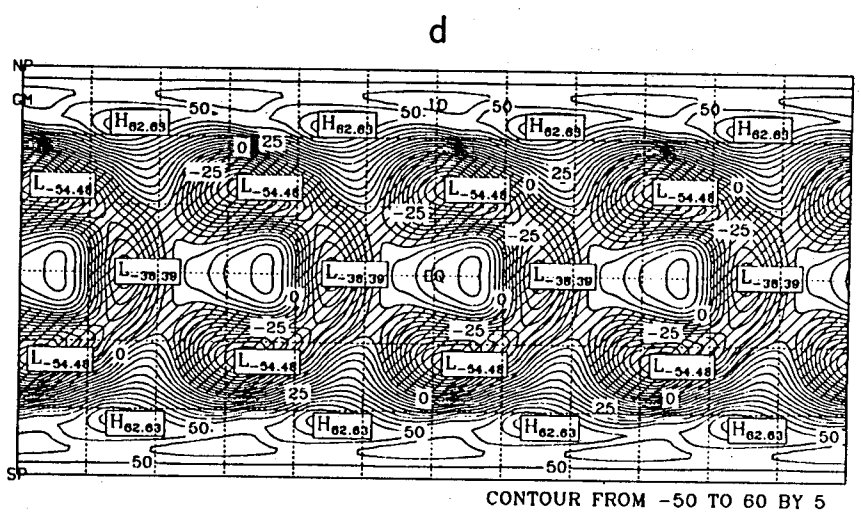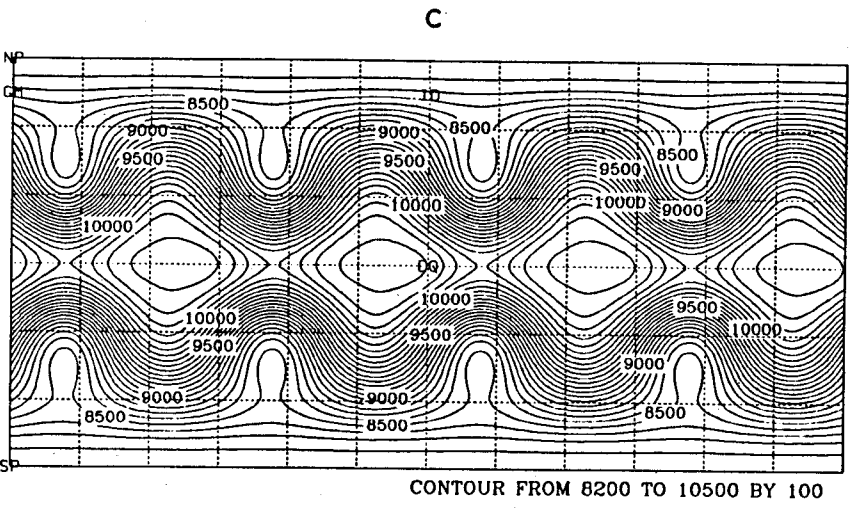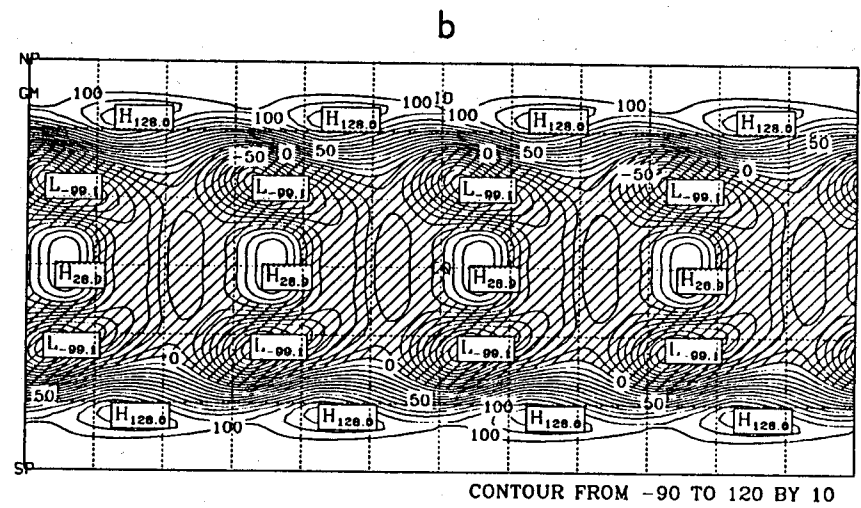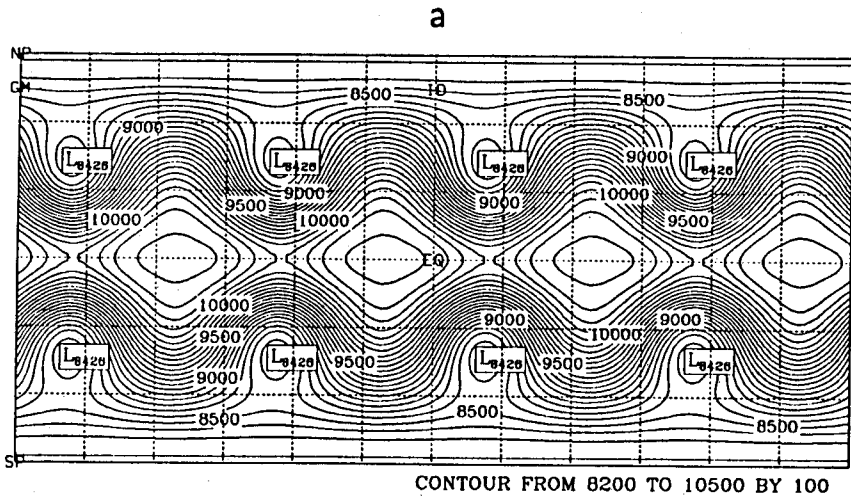
Figure 6.5 Height fields at day 14 for (a) T42 and (c) T63 and differences with reference solution for (b) T42 and (d) T63. Contour intervals are (a) 100 m, (c) 100 m, (b) 10 m, and (d) 5 m.
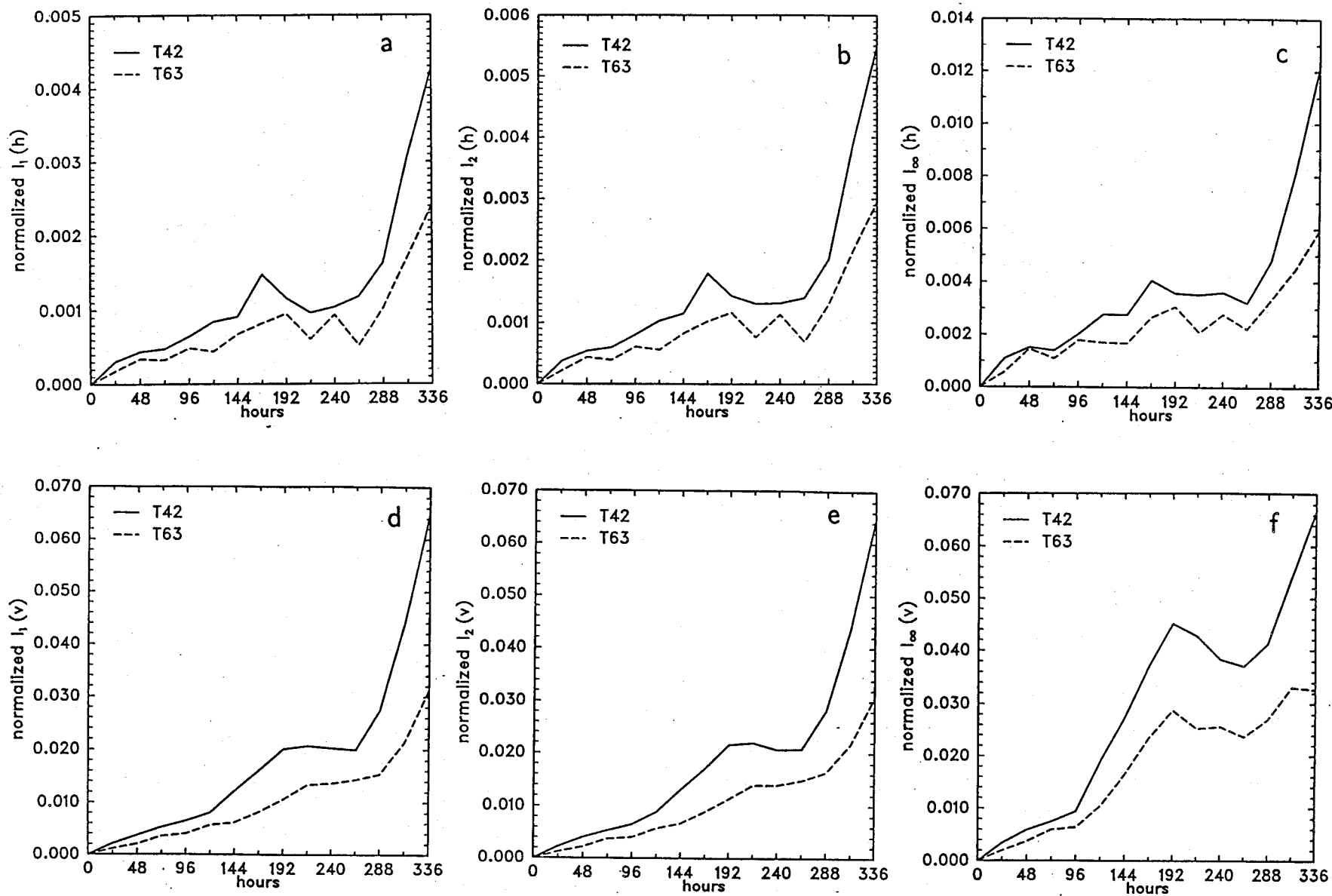
Figure 6.6 l_1, l_2, and l_∞ height errors (a–c) and l_1, l_2, and l_∞ wind errors (d–f) for T42 and T63 resolutions.
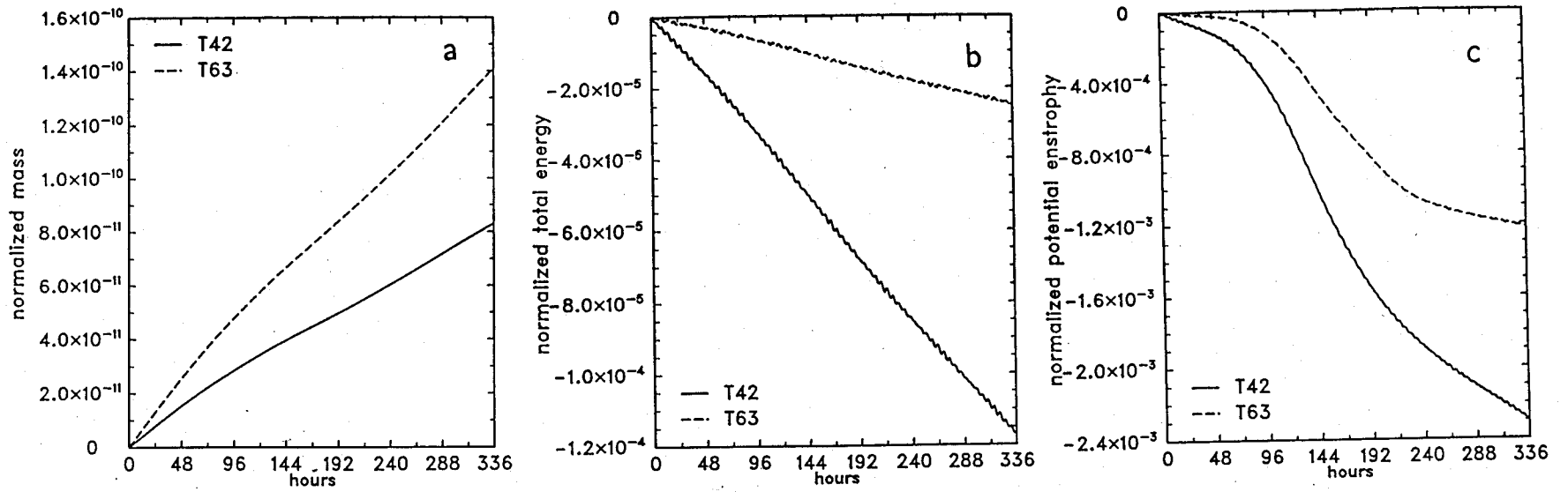
Figure 6.7 Global average (a) mass, (b) energy, and (c) potential enstrophy for T42 and T63 resolutions.
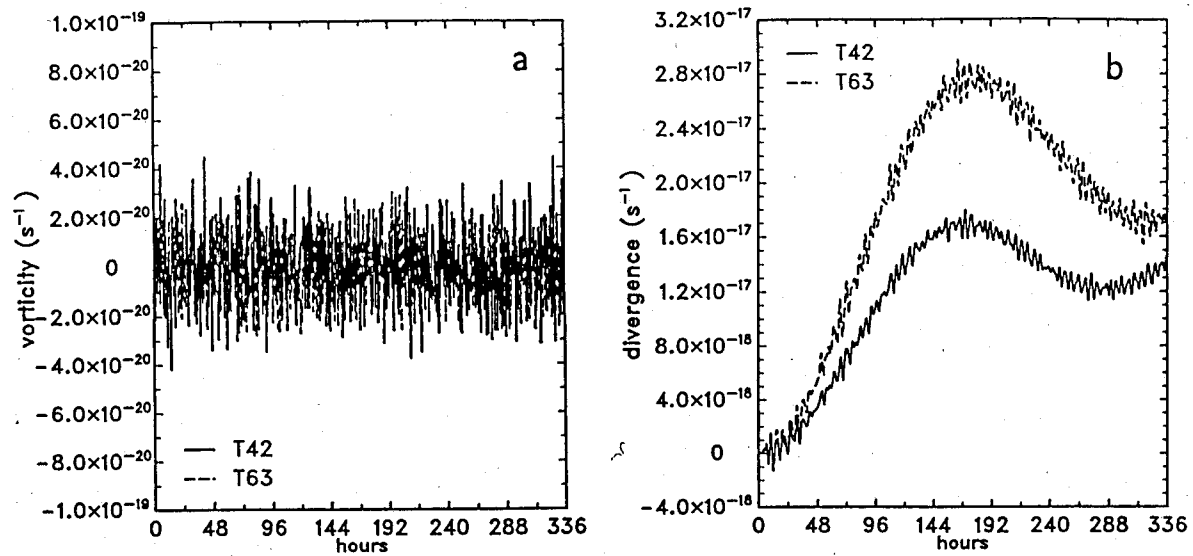
Figure 6.8 Global average (a) vorticity and (b) divergence for T42 and T63 resolutions.

a

CONTOUR FROM 8300 TO 10500 BY 100

b

CONTOUR FROM −20 TO 35 BY 2.5

c

CONTOUR FROM 8200 TO 10500 BY 100

d

CONTOUR FROM −80 TO 130 BY 10
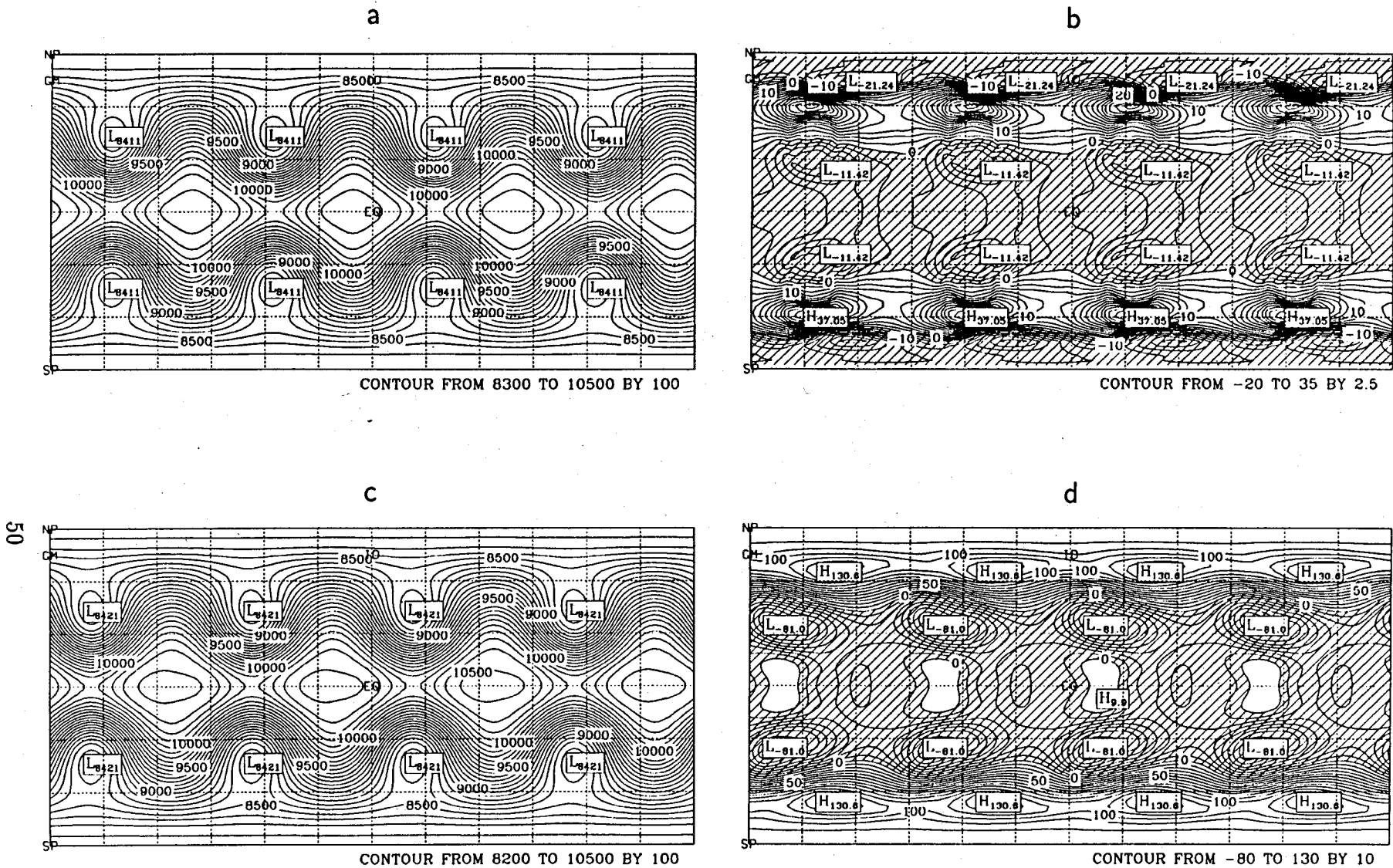
Figure 6.9 Height field at (a) day 7 and (c) day 14 for T42 case with 180 second time step and difference with T213 reference solution at (b) day 7 and (d) day 14. Contour intervals are (a) 100 m, (c) 100 m, (b) 2.5 m, and (d) 10 m.

a

b

CONTOUR FROM 8200 TO 10500 BY 100

CONTOUR FROM −55 TO 30 BY 5

c

d

CONTOUR FROM 8100 TO 10500 BY 100

CONTOUR FROM −85 TO 50 BY 5
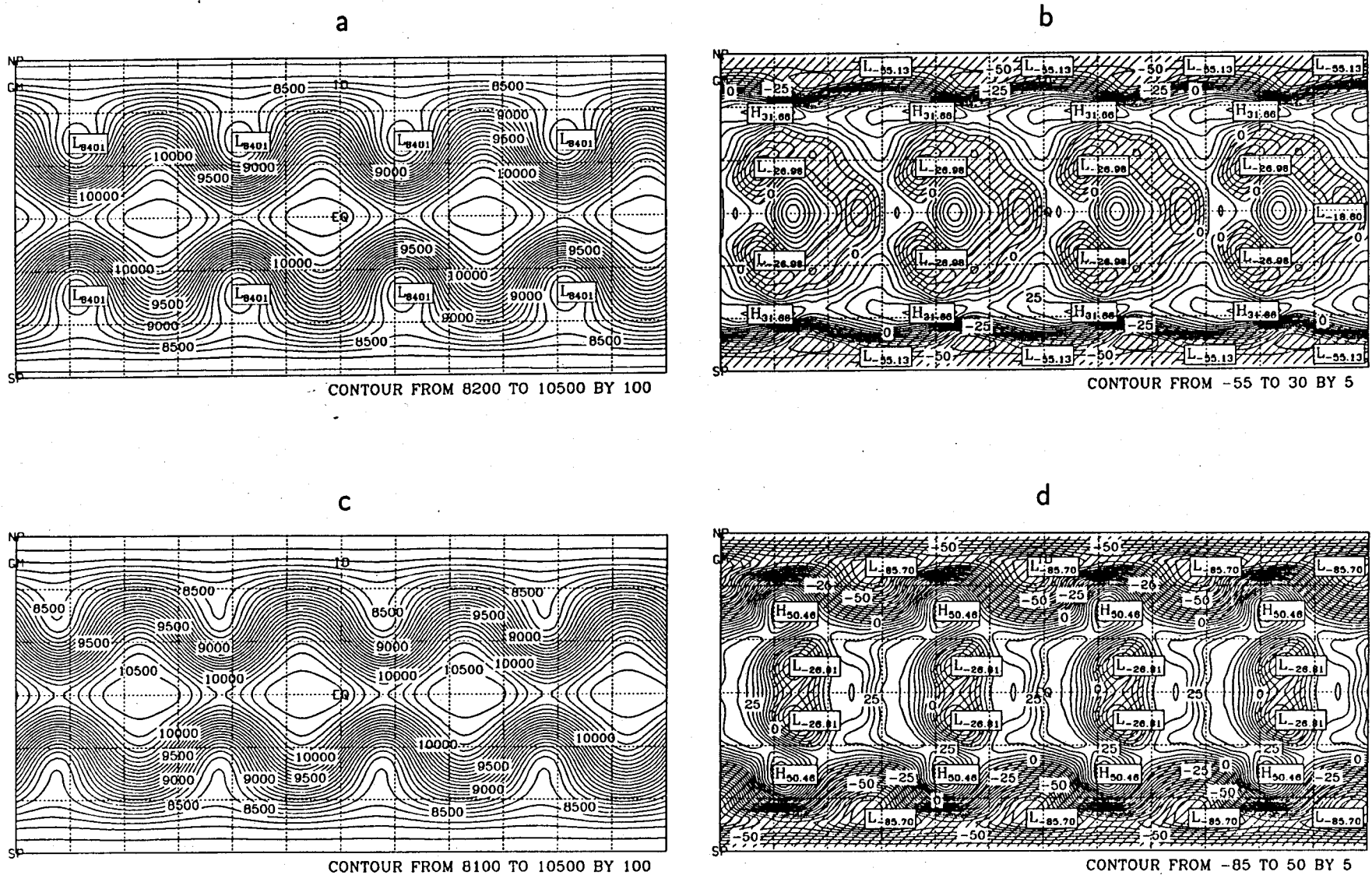
Figure 6.10 Height field at (a) day 7 and (c) day 14 for T42 case with no diffusion and difference with T213 reference solution at (b) day 7 and (d) day 14. Contour intervals are (a) 100 m, (c) 100 m, (b) 5 m, and (d) 5 m.

a

b

CONTOUR FROM 8400 TO 10500 BY 100

CONTOUR FROM 8300 TO 10400 BY 100
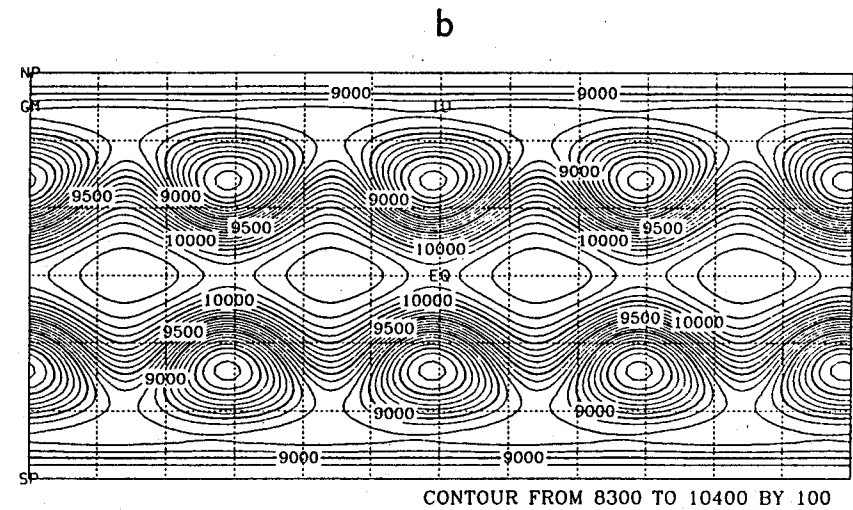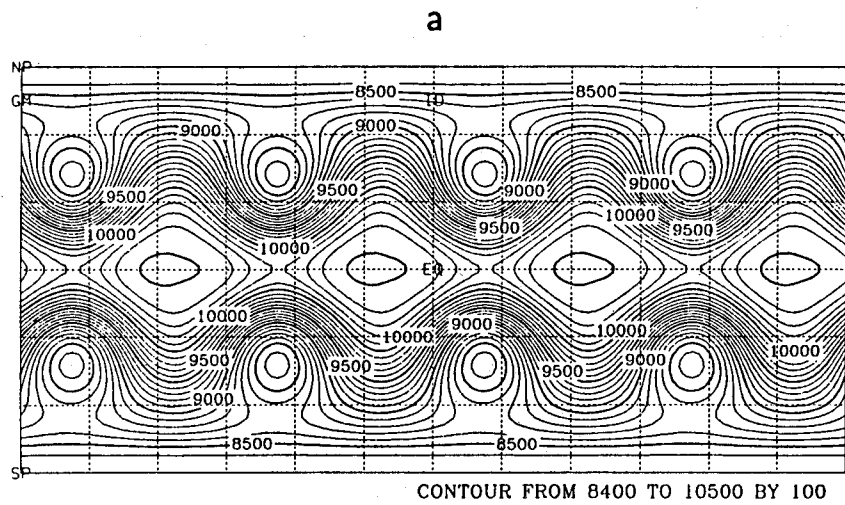
Figure 6.11 Height field at (a) 30 days and (b) 60 days from T42 case with 600 second time step and normal diffusion. Contour interval is 100 m.

7. Analyzed 500 mb Height and Wind Field Initial Conditions

These cases start from analyses of observed data after being initialized with nonlinear normal mode initialization. Details of the initialization are provided in Appendix C. Horizontal diffusion was included in the model for all forecasts. The implications of this diffusion on the forecasts and reference solutions are discussed in the Appendix A.

The l_1, l_2 and l_∞ errors from the forecasts with T42, T63 and T106 are graphed in Figure 7.1. In all figures the short dashed curves are from the T42 forecasts, the solid are from the T63 and the longer dash from the T106. The circle line marker denotes the 21 Dec 1978 Case, the square the 9 Jan 1979 and the triangle 16 Jan 1979. The $l_1(h)$ and $l_1(v)$ errors improve with resolution as expected. The relative standing of the three cases varies with the different resolutions. The $l_2(h)$ and $l_2(v)$ errors as a general rule also improve with resolution. There is an example where a particular T63 forecast is not as good as a T42 forecast for a different case, although for any given case, the l_2 errors always decrease with increasing resolution. The $l_\infty(h)$ and $l_\infty(v)$ errors show much more spread with significant overlap between resolutions and increased resolution does not always result in monotonic decrease in error.

The global integrals of mass were saved to only 10 digits. The variation in the mass over the 5 day forecasts is only 1 or 2 in the last digit. Thus we do not include graphs of the normalized global average mass, as they would basically be straight horizontal lines with a few steps. For an example, see the appendix which shows the normalized global average mass from a 30 day forecast with T213 truncation.

The global average vorticity and divergence are graphed in Figure 7.2. The line codes and markers are the same as in the previous graphs. The global averages are better for lower resolution, i.e. T42 is marginally better than T63 and T63 is noticeably better than T106. Comparison with a T213 run in the appendix shows that T106 is better than T213. The decrease in degree of conservation is attributable to the lack of discrete orthonormality in the Legendre functions as implemented in the code used here and discussed earlier in Test Case 2.

The normalized global average total energy and potential enstrophy are graphed in Figure 7.3 with the same line codes and markers as above. Energy and enstrophy are conserved better with increased resolution associated with the decreased diffusion, as expected. Comparison with the appendix shows that this improvement is also observed when going from T106 to T213 as well. The degree of conservation is case dependent with the relative standing of the three cases being the same with all resolutions.

Figures 7.4a and b present north and south polar stereographic maps, respectively, of the initialized height fields for the 21 December 1978 Case. For comparison, Appendix C shows the north hemisphere before and after initialization. To save space we include

contour maps only for one case. We have chosen the one which is in the middle with respect to the error measures, and which has the strong flow over the pole. Figures 7.5 - 7.6 present north polar stereographic maps of the 1 day height forecasts and errors from the 21 December 1978 Case. The figures show the T42 fields or errors in the upper left, T63 in the upper right, and T106 in the lower left. The reference solution from the T213 is in the lower right. The fields are plotted from the equator to pole but the errors are plotted only poleward of 30 degrees since the error fields show little of interest equatorward of 30 degrees. The reference solution is from a T213 integration with diffusion coefficient $K_4 = 8.0\text{x}10^{12}$ m^4/s and a 360s time step. The contour interval is 50m for the height fields and 10m, 5m and 2.5m for the T42, T63 and T106 errors, respectively. Figures 7.7 and 7.8 show the corresponding south polar stereographic maps. Figures 7.9 - 7.12 present north and south polar stereographic maps of the 5 day height forecasts and errors. The contour interval is again 50m for the height fields, but 25m, 25m and 12.5m for the T42, T63 and T106 errors, respectively.

Figure 7.13 shows the trace of the height field at the grid points closest to (40N, 105W) for the 21 Dec 1978, 9 Jan 1979, and 16 Jan 1979 Cases. The actual locations of the grid points are (40.77N, 106.0W) for T42, (40.1N, 105.0W) for T63 and (40.93N, 104.63W) for T106. The line codes for the different resolutions are the same as used earlier, with the short dash for T42, solid for T63, and long dash for T106. The data are plotted every hour rather than every iteration. Since in the T42 case this is an odd number of time steps, any significant $2\Delta t$ signal caused by even-odd splitting in the leap frog time stepping would appear in the graphs. There is no indication of such a signal. The other resolutions also showed no $2\Delta t$ signal when we examined them during the runs. The figures also indicate that high frequency gravity wave motion is not present in the forecasts. The three resolutions do not track each other identically, even initially, because the grid point locations are not identical, and even if they were identical the grid values could differ because of the different truncations.
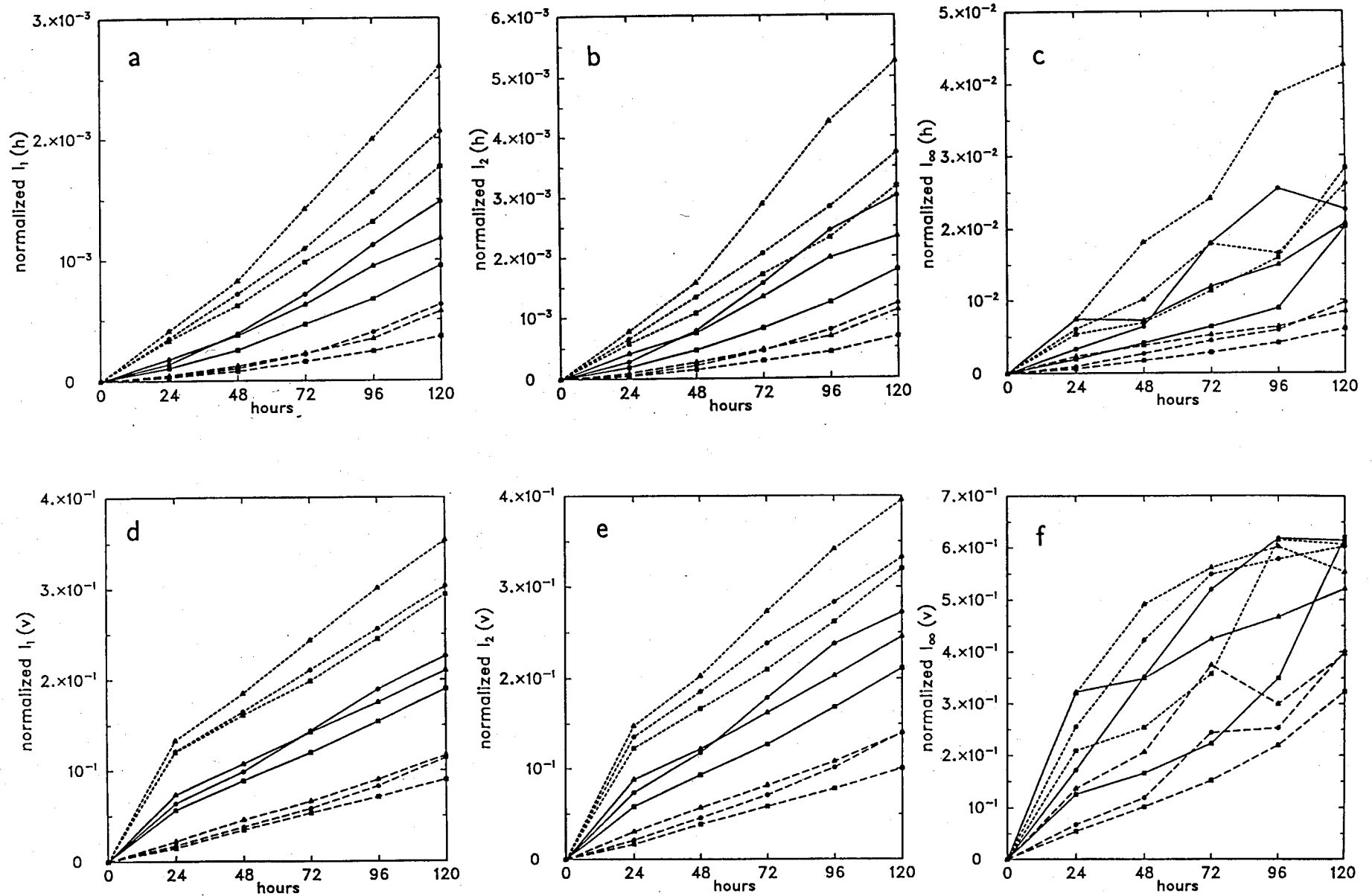
Figure 7.1 $l_1, l_2,$ and l_∞ height errors (a–c) and $l_1, l_2,$ and l_∞ wind errors (d–f). Short dash for T42, solid for T63, and long dash for T106. Circle line marker for 21 December 1978 case, square for 9 January 1979, and triangle for 16 January 1979.
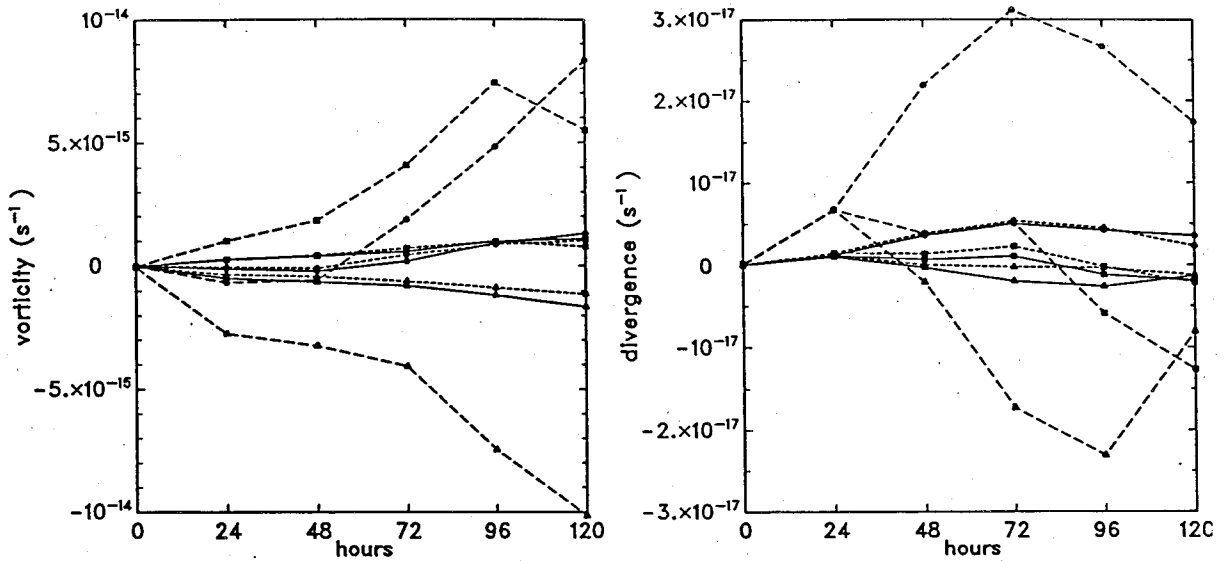
Figure 7.2 Global average vorticity and divergence. Short dash for T42, solid for T63, and long dash for T106. Circle line marker for 21 December 1978 Case, square for 9 January 1979, and triangle for 16 January 1979.
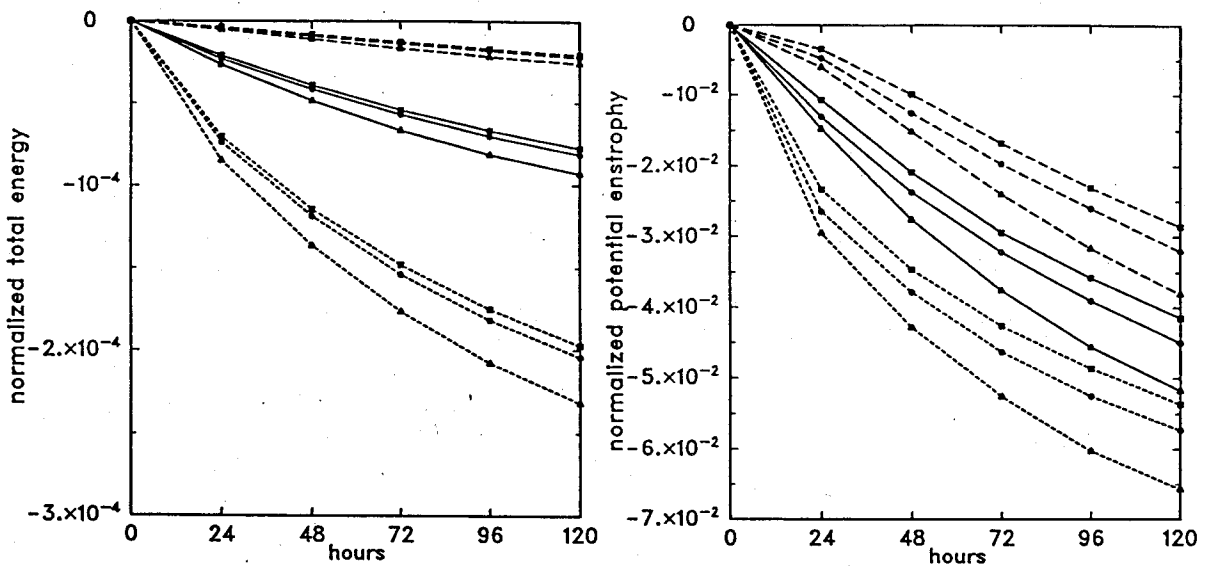
Figure 7.3 Global average energy and potential enstrophy. Short dash for T42, solid for T63, and long dash for T106. Circle line marker for 21 December 1978 Case, square for 9 January 1979, and triangle for 16 January 1979.

CONTOUR FROM 9200 TO 10250 BY 50   CONTOUR FROM 9200 TO 10250 BY 50
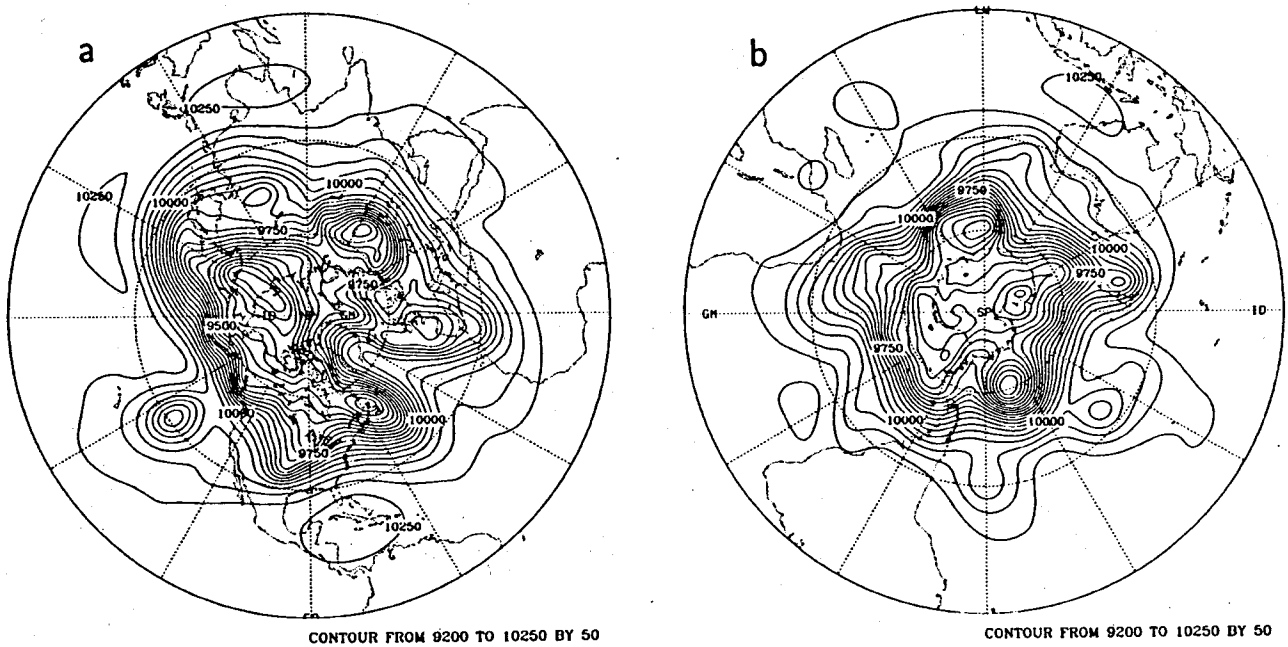
Figure 7.4 Initial height field for 21 December 1978 Case. (a) North polar stereographic projection, (b) South polar stereographic projection. Contour interval is 50 m.
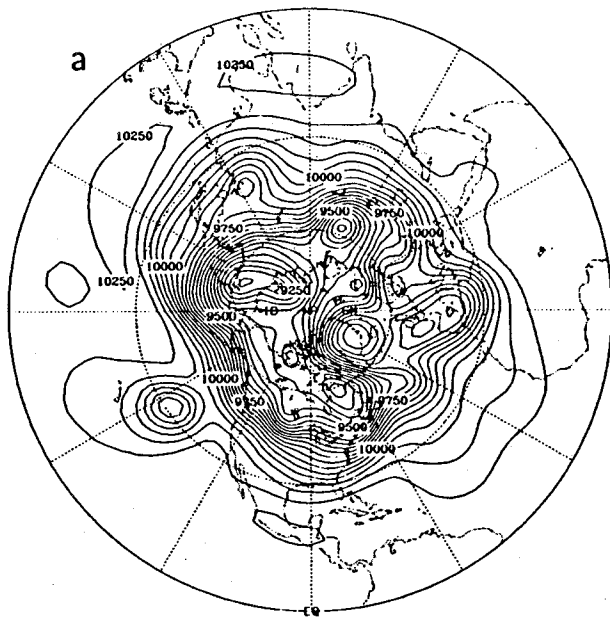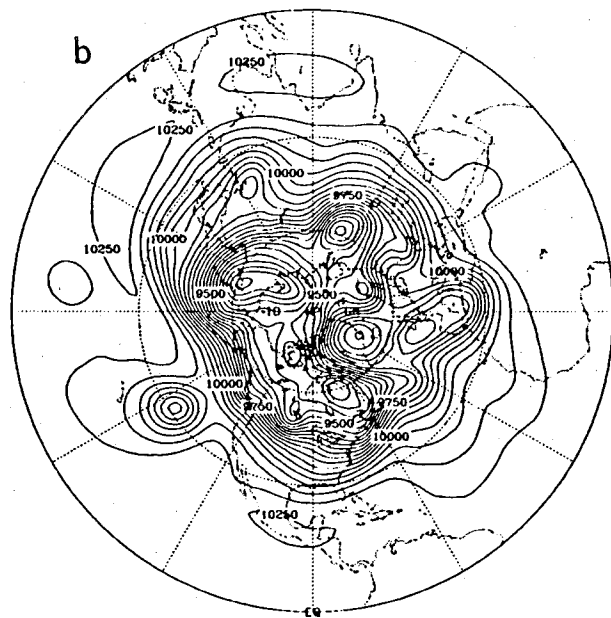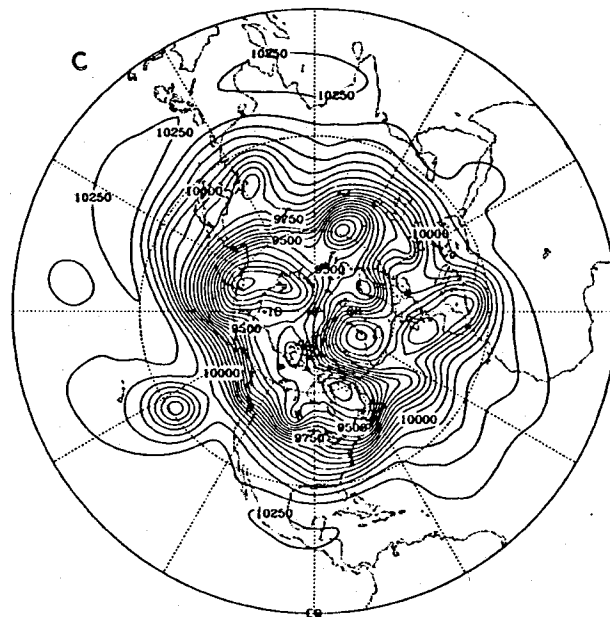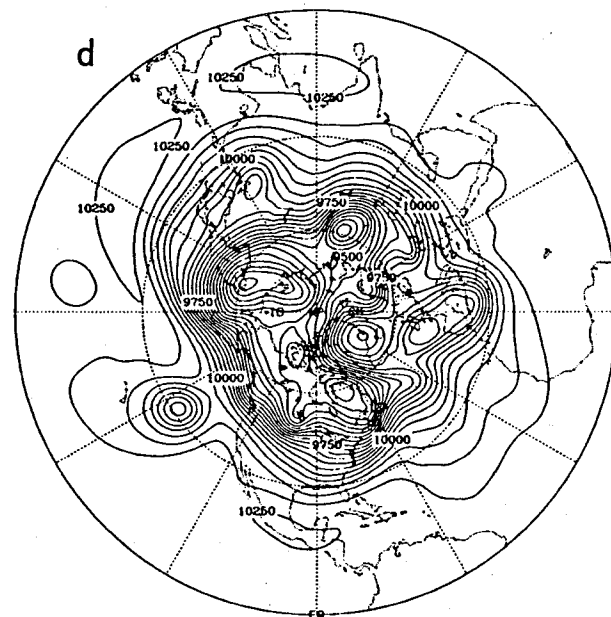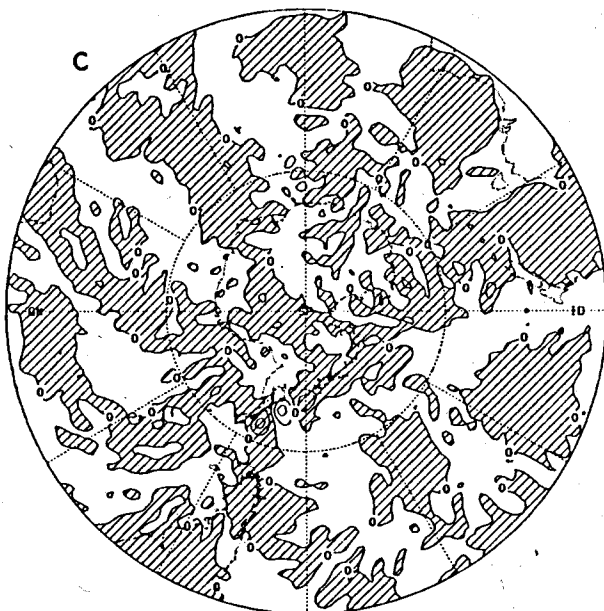
Figure 7.5 Height field for day 1 of 21 December 1978 Case on North polar stereographic projection for (a) T42, (b) T63, (c) T106, and (d) reference solution. Contour interval is 50 m.
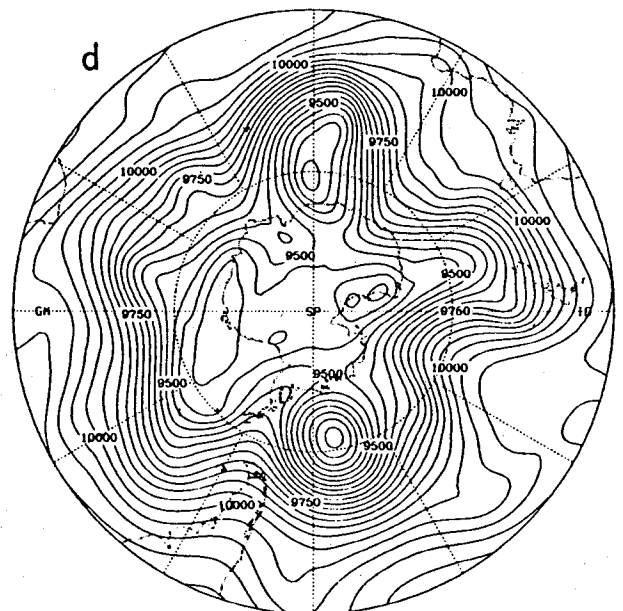
a

CONTOUR FROM -40 TO 60 BY 10

b

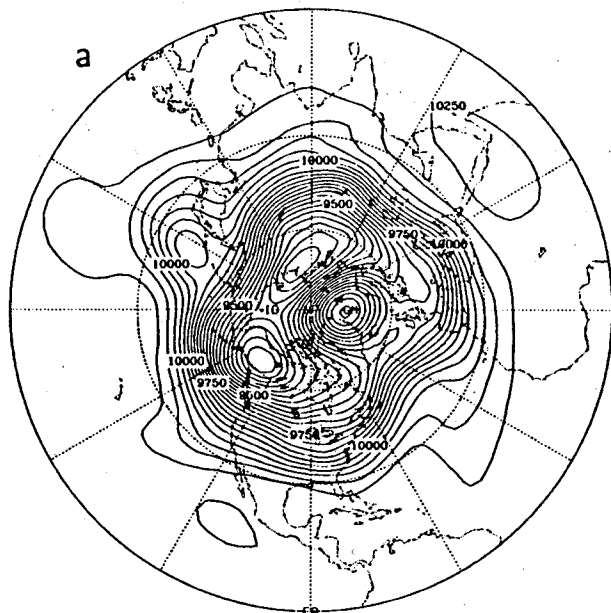CONTOUR FROM -20 TO 30 BY 5

c

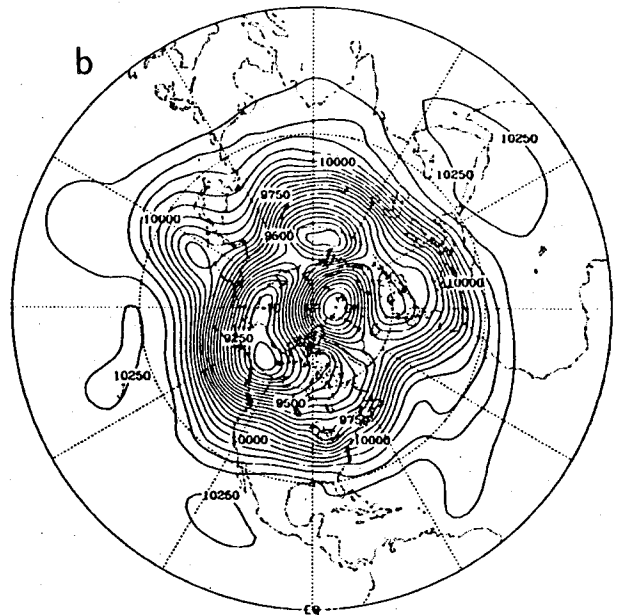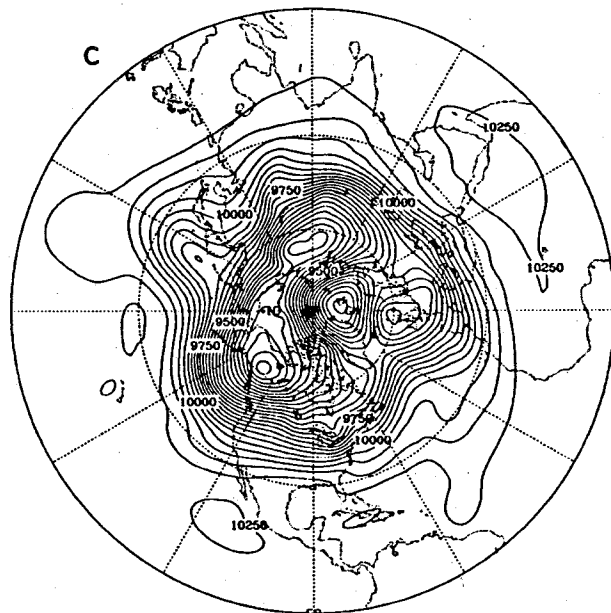CONTOUR FROM -7.5 TO 7.5 BY 2.5

d

CONTOUR FROM 9150 TO 10250 BY 50
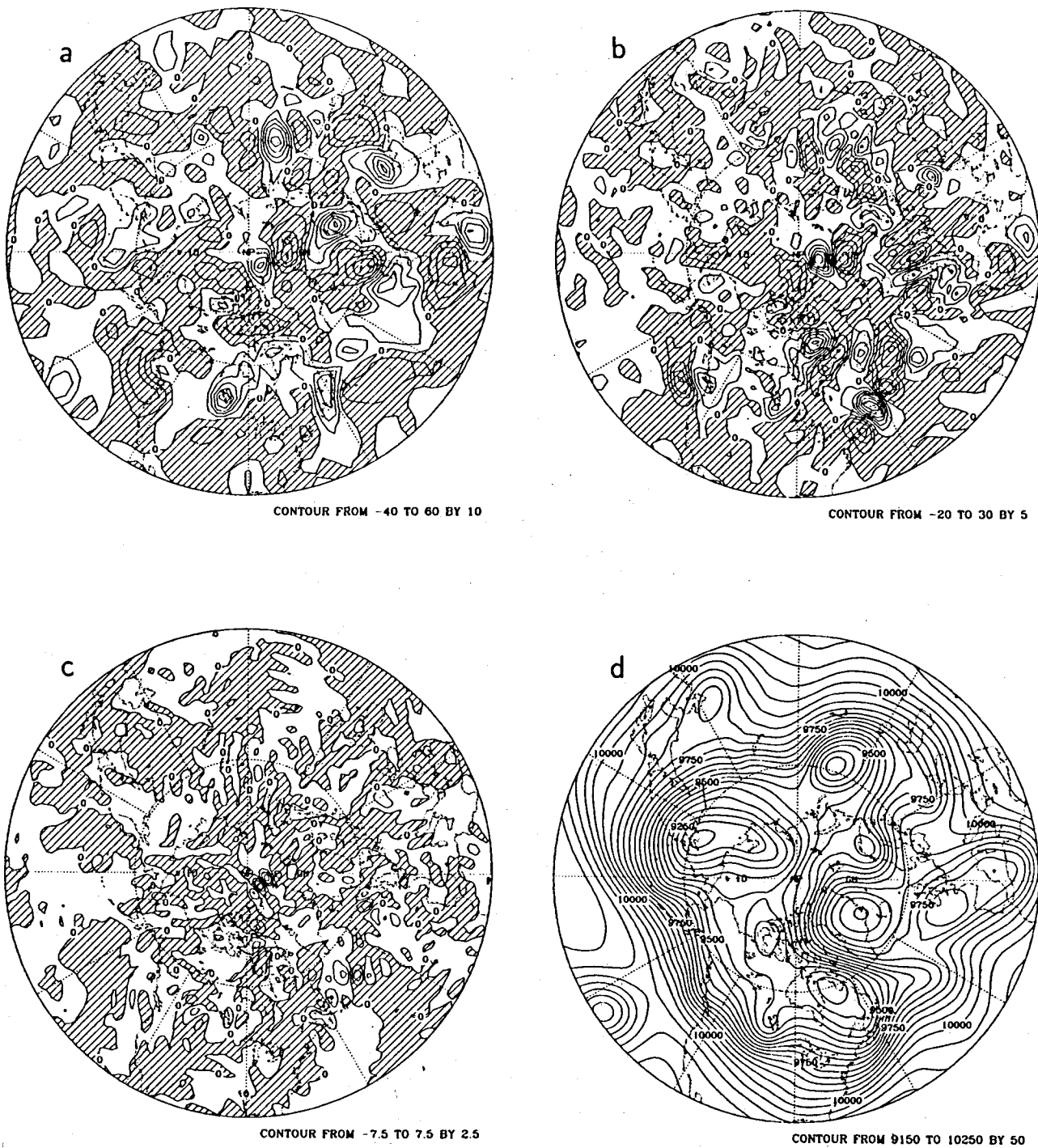
Figure 7.6 Differences with reference solution of height field for day 1 of 21 December 1978 Case on North polar stereographic projection for (a) T42, (b) T63, and (c) T106, and (d) reference solution itself. Contour intervals are (a) 10 m, (b) 5 m, (c) 2.5 m, and (d) 50 m.
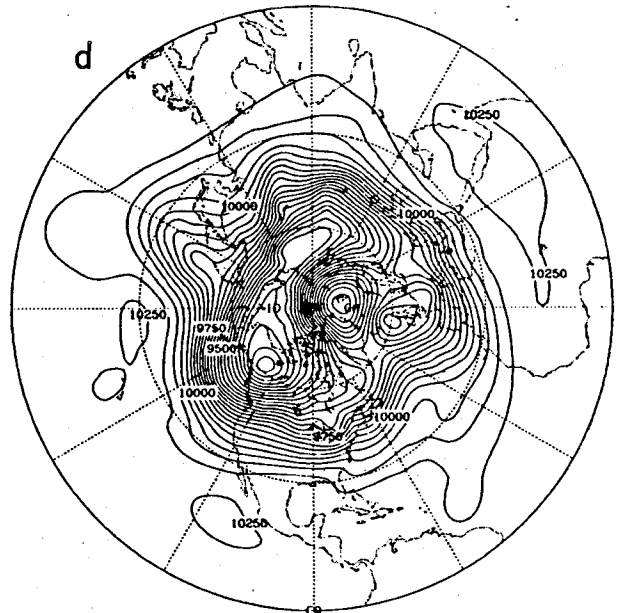
59
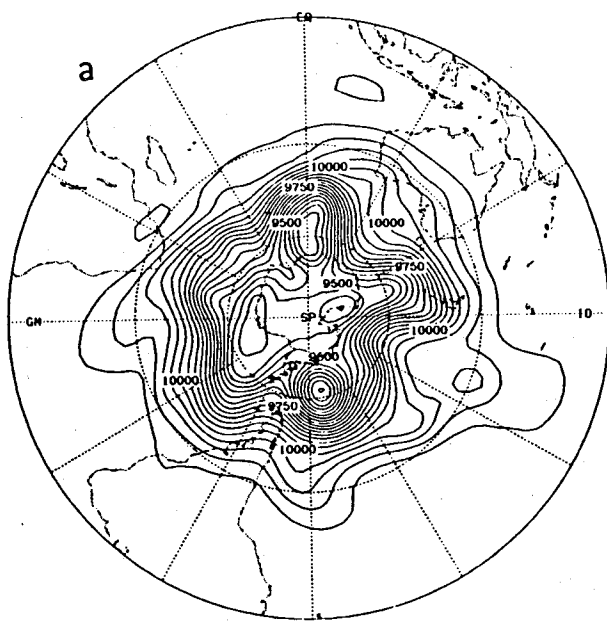
CONTOUR FROM 9150 TO 10250 BY 50
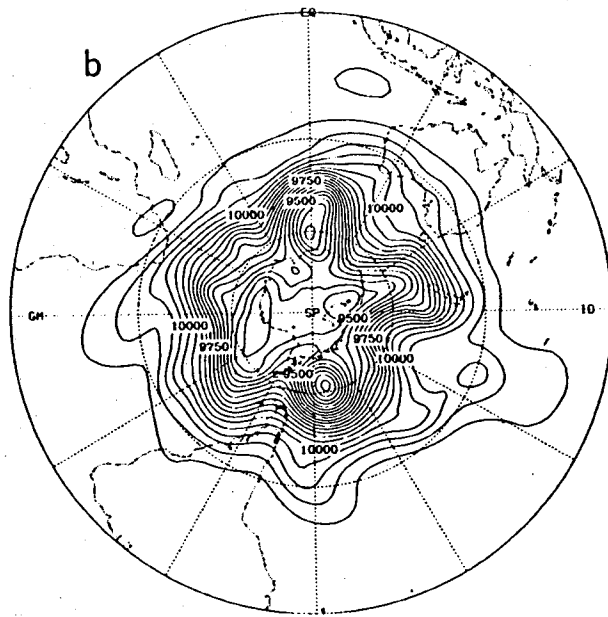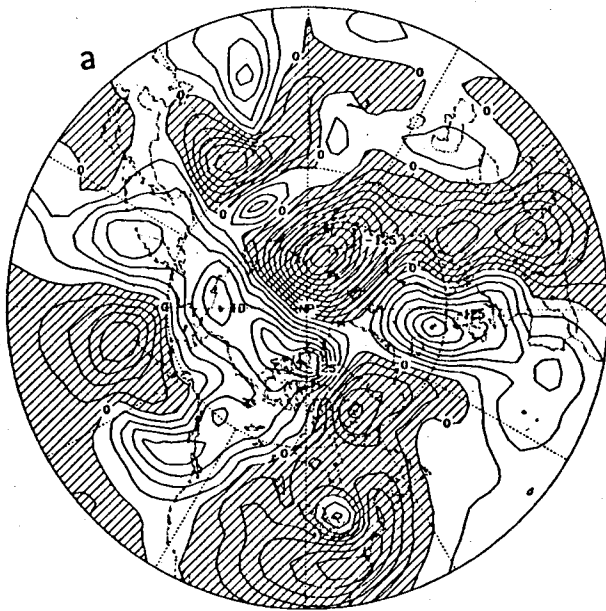
CONTOUR FROM 9150 TO 10250 BY 50
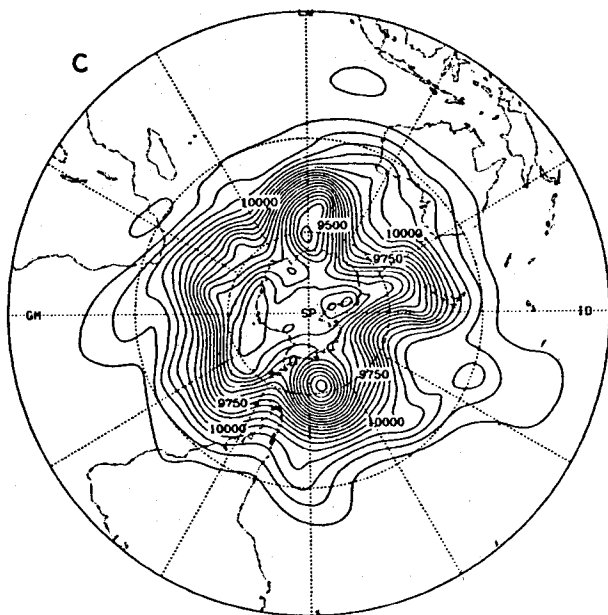
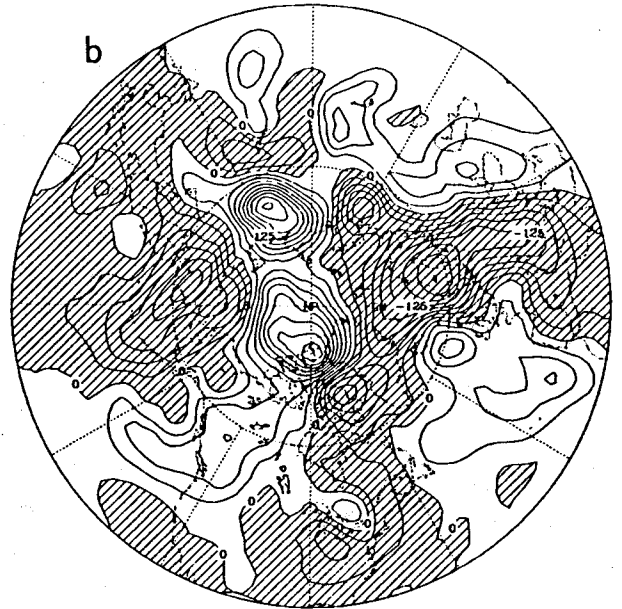CONTOUR FROM 9150 TO 10250 BY 50
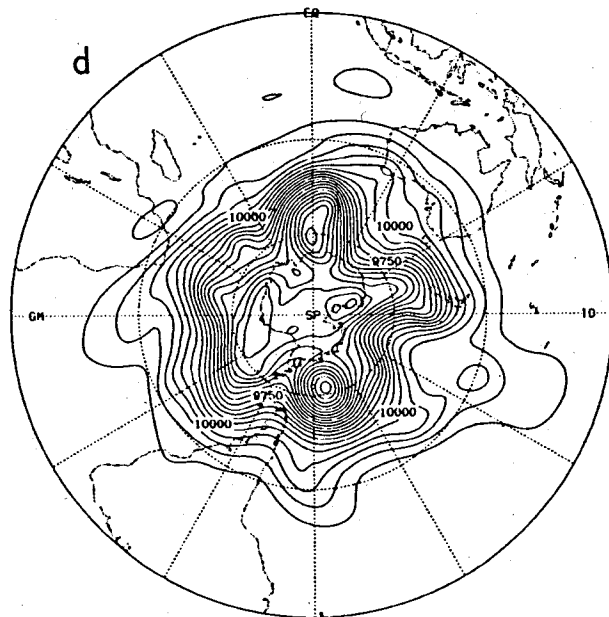
CONTOUR FROM 9150 TO 10250 BY 50

Figure 7.7 Height field for day 1 of 21 December 1978 Case on South polar stereographic projection for (a) T42, (b) T63, (c) T106, and (d) reference solution. Contour interval is 50 m.
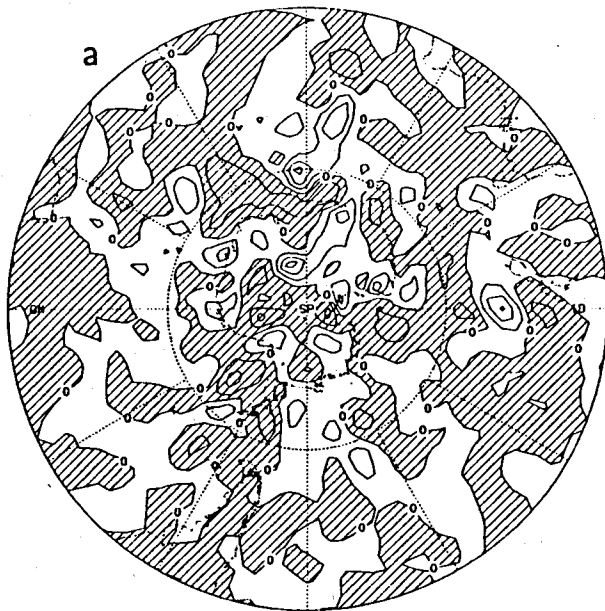
CONTOUR FROM -40 TO 60 BY 10
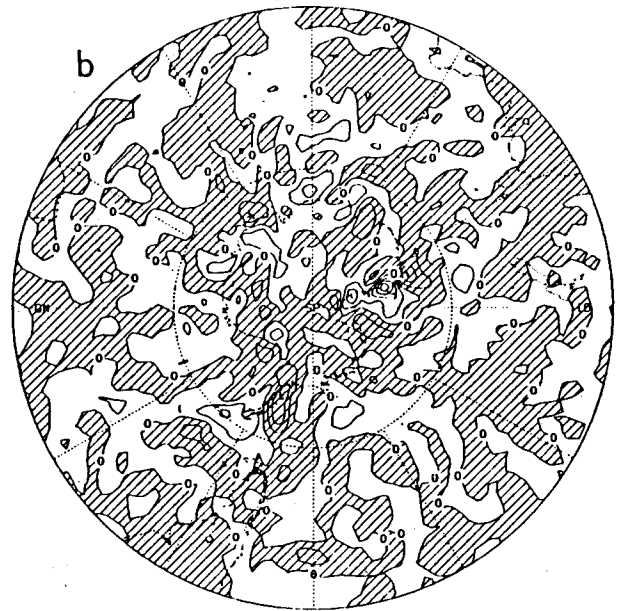
CONTOUR FROM -20 TO 30 BY 5

CONTOUR FROM -7.5 TO 7.5 BY 2.5

CONTOUR FROM 9150 TO 10250 BY 50

Figure 7.8 Differences with reference solution of height field for day 1 of 21 December 1978 Case on South polar stereographic projection for (a) T42, (b) T63, and (c) T106, and (d) reference solution itself. Contour intervals are (a) 10 m, (b) 5 m, (c) 2.5 m, and (d) 50 m.

a

CONTOUR FROM 9100 TO 10250 BY 50

b

CONTOUR FROM 9100 TO 10250 BY 50

c

CONTOUR FROM 9050 TO 10250 BY 50
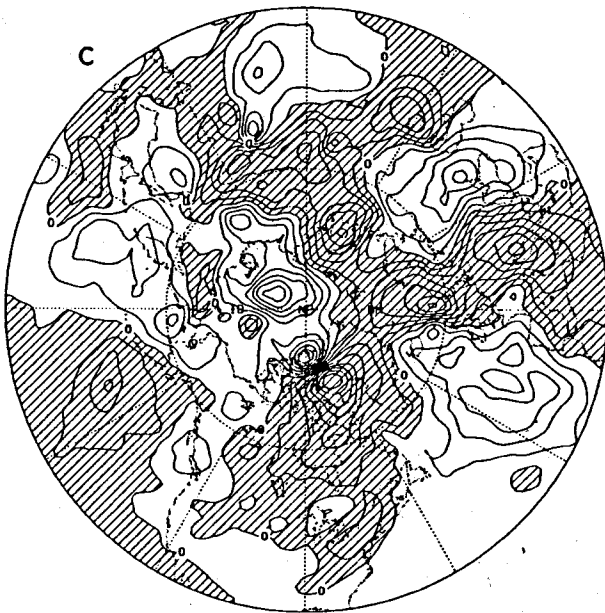
d

CONTOUR FROM 9050 TO 10250 BY 50

Figure 7.9 Height field for day 5 of 21 December 1978 Case on North polar stereographic projection for (a) T42, (b) T63, (c) T106, and (d) reference solution. Contour interval is 50 m.
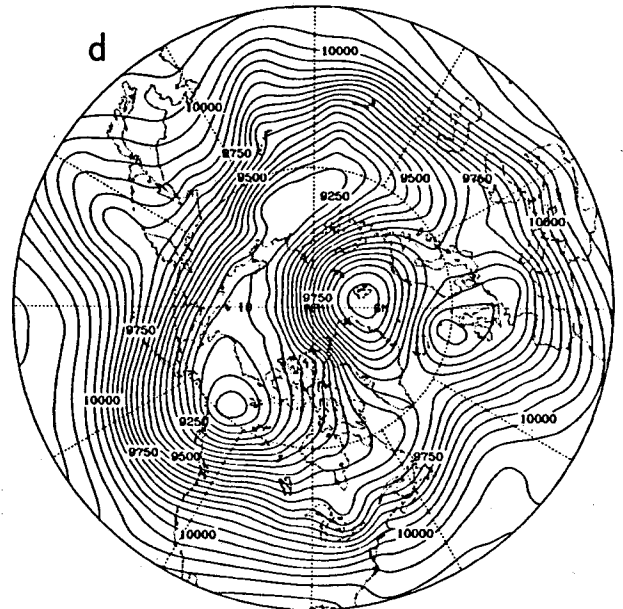
CONTOUR FROM -250 TO 200 BY 25
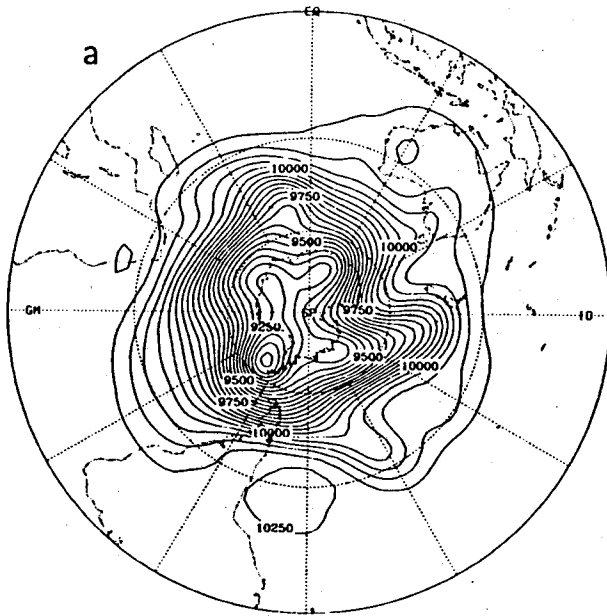
CONTOUR FROM -200 TO 225 BY 25
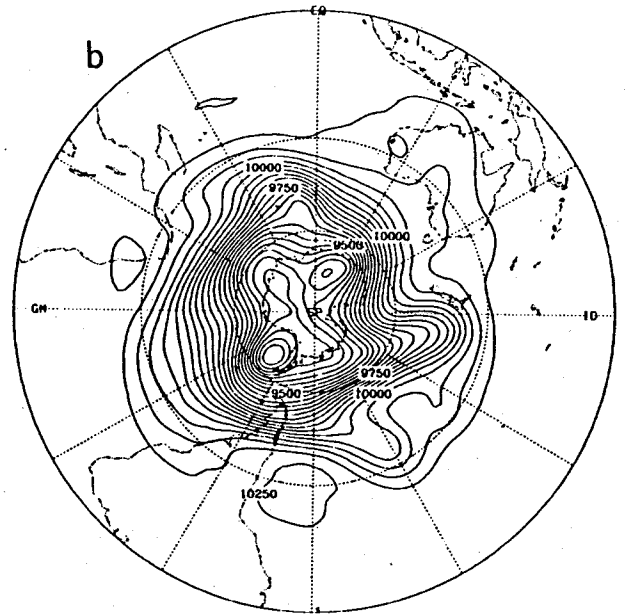
CONTOUR FROM -87.5 TO 75 BY 12.5
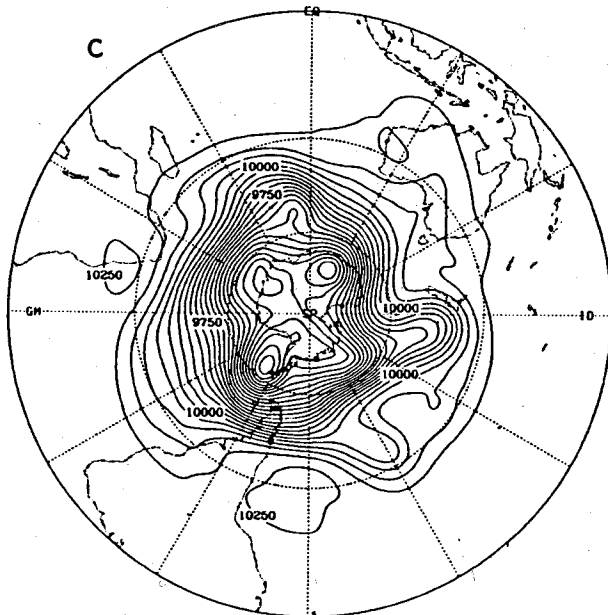
CONTOUR FROM 9050 TO 10250 BY 50

Figure 7.10 Differences with reference solution of height field for day 5 of 21 December 1978 Case on North polar stereographic projection for (a) T42, (b) T63, and (c) T106, and (d) reference solution itself. Contour intervals are (a) 25 m, (b) 25 m, (c) 12.5 m, and (d) 50 m.
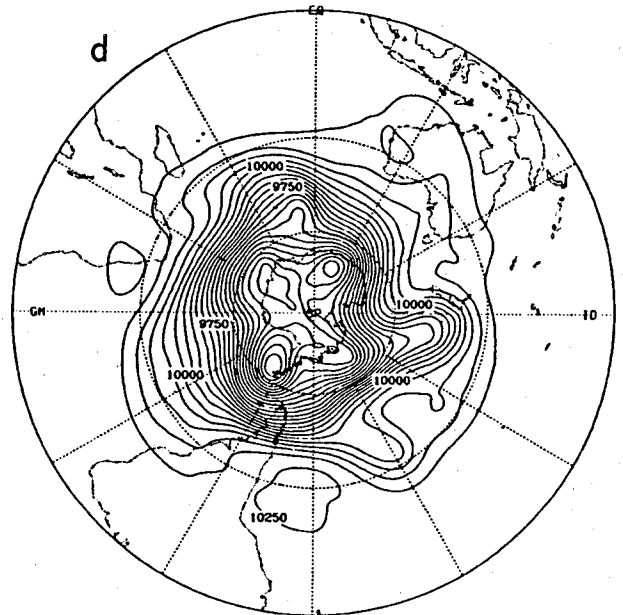
63

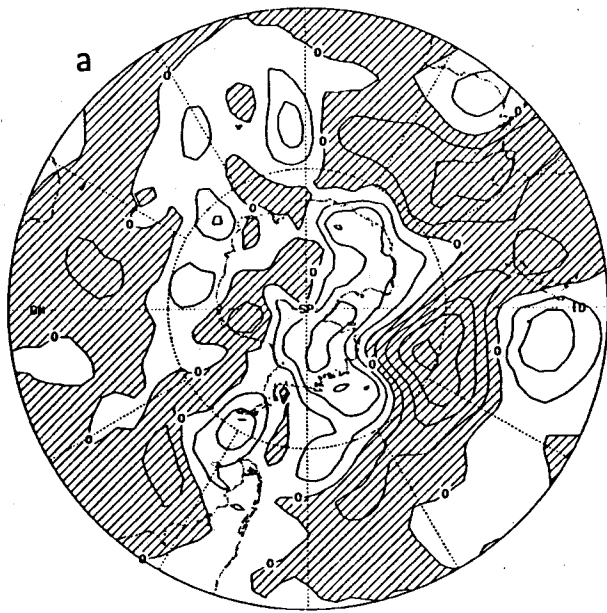CONTOUR FROM 9100 TO 10250 BY 50

CONTOUR FROM 9100 TO 10250 BY 50

CONTOUR FROM 9050 TO 10250 BY 50

CONTOUR FROM 9050 TO 10250 BY 50

Figure 7.11 Height field for day 5 of 21 December 1978 Case on South polar stereographic projection for (a) T42, (b) T63, (c) T106, and (d) reference solution. Contour interval is 50 m.

a

CONTOUR FROM -250 TO 200 BY 25

b

CONTOUR FROM -200 TO 225 BY 25

c

CONTOUR FROM -87.5 TO 75 BY 12.5

d

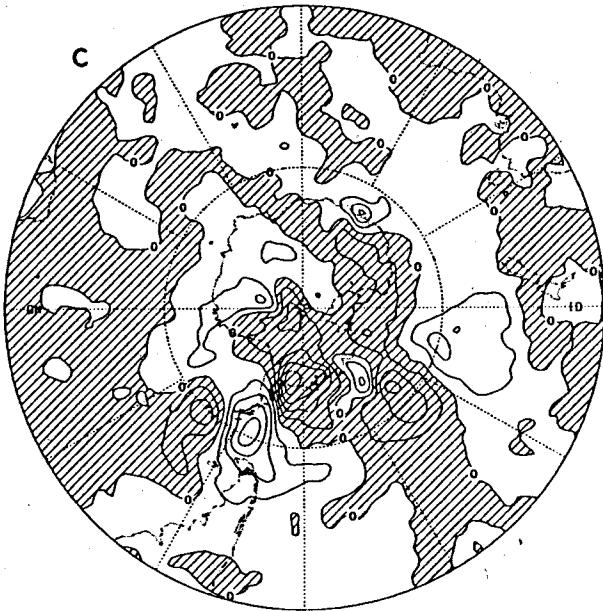CONTOUR FROM 9050 TO 10250 BY 50

Figure 7.12 Differences with reference solution of height field for day 5 of 21 December 1978
Case on South polar stereographic projection for (a) T42, (b) T63, (c) T106, and
(d) reference solution itself. Contour intervals are (a) 25 m, (b) 25 m, (c) 12.5 m,
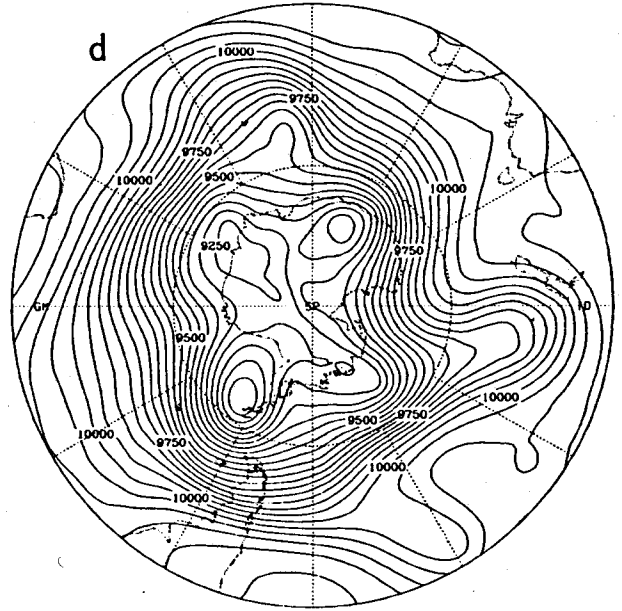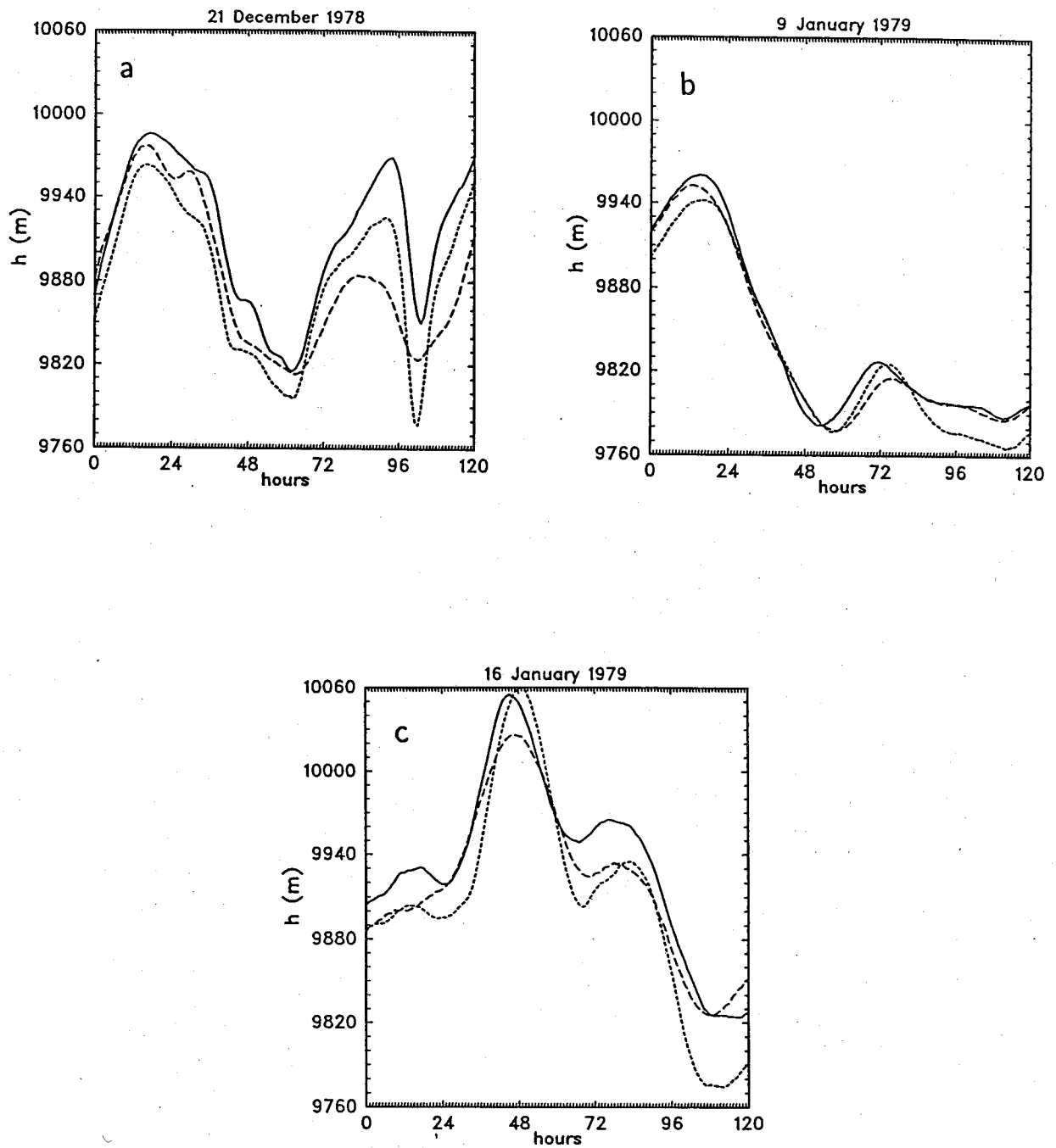and (d) 50 m.

65

Figure 7.13 Height field as a function of time at grid points closest to (40N, 105W) for T42 (short dash), T63 (solid), and T106 (long dash), and (a) 21 December 1978, (b) 9 January 1979, and (c) 16 January 1979.

Appendix A Reference Solutions

In this appendix we present various properties of the real data forecasts with the high resolution model to indicate the uncertainties associated with using it as a reference solution. In particular, we examine the uncertainty associated with including diffusion in the equations. Certainly any errors less than the difference in the reference solutions with and without diffusion indicates that the test solution is within the uncertainty of the reference solution, and any solution reasonably close to the reference solution should also be considered as within the uncertainty.

1. Kinetic Energy Spectra

As mentioned in Williamson et al. (1992), the addition of an explicit diffusion term may be desirable and may lead to improvement in some of the error measures. Figure A1(a) shows the kinetic energy spectra from day 5 of the T213 forecasts from the initial (21 December 1978) data of Test Case 7 with (lower curve) and without (upper curve) diffusion. The equations used to calculate the kinetic energy spectrum are presented in Appendix B. The diffusion coefficient was chosen to give a reasonably straight tail to the spectra. With the coefficient chosen, the tail is slightly steeper than the -3 line plotted for reference. The diffusion has no discernable effect in this plot on wavenumbers less than 40.

Figure A1(b) shows the spectra for the same case from the T106 forecasts. Here, there is no discernable difference for wavenumbers less than 15. Figures A1(c) and (d) compare the spectra from the T106 and T213 forecasts without and with diffusion respectively. In both cases, although the small wavenumbers are very similar, there are observable differences in wavenumbers as small as 8. With the diffusion chosen, the characteristics of the T106 forecast spectrum is very similar to the T213. There is less similarity with either the T63 and T42 spectra compared to the T213. The comparison is shown in Figures A1(e) and (f) for the T63 and T42, respectively. The tail in both is steeper than the corresponding portion of the T213, indicating the diffusion could probably be reduced.

2. Dependence of error measures on parameters defining reference solution

We have performed a few experiments to quantify the uncertainty in the reference solution due to the choice of values for some of the arbitrary parameters. These experiments indicate that the reference solution can be no better than the differences indicated but do *not* indicate that it is necessarily as good as these differences. The differences are summarized in Table A.1. The experiments were all carried out at T213 truncation for the 21 December 1978 initial data set in Test Case 7. The first experiment compares the solution truncated to T106 with the complete T213 representation and indicates the contribution to the norms from neglecting waves 107 through 213. The second experiment compares the forecasts with and without diffusion and indicates the uncertainty introduced

by the arbitrary diffusion. The third experiment compares the standard 360 sec time step with a 450 sec one and provides some indication of the time truncation error.

	$l_1(h)$	$l_2(h)$	$l_\infty(h)$
Difference due to 106 truncation	1.0×10^{-5}	2.0×10^{-5}	2.5×10^{-4}
Difference due to diffusion	8.0×10^{-5}	1.5×10^{-4}	2.5×10^{-3}
Difference due to time step	3.5×10^{-5}	5.5×10^{-5}	6.0×10^{-4}

Table A.1: Approximate differences after 5 days

Any errors calculated with respect to the reference solution that are smaller than these indicate only that the alternate is within the uncertainty of the reference solution.

3. Effect of diffusion on error measures

Fig. A.2 compares the normalized $l_1(h)$, $l_2(h)$ and $l_\infty(h)$ errors for the T106 solutions from the 21 December 1978 initial data of Test Case 7 with (dashed) and without (solid) diffusion. They are calculated against the T213 reference solution with diffusion, retaining all 213 waves in the grid representation. The differences in the normalized l_1, l_2 and l_∞ norms grow to 1.8×10^{-4}, 3.6×10^{-4}, and 2.2×10^{-3} respectively, at day five. The diffusion decreases the errors slightly by damping the erroneous small scales. This damping is evident in the kinetic energy spectra shown earlier. Any test scheme with an error in this range should probably be considered to be comparable to the T106 spectral.

4. Effect of diffusion on global integrals

When diffusion is added to the shallow water equations, mass, vorticity and divergence continue to be conserved by the continuous equations but energy and enstrophy are no longer conserved quantities. In the following, we present the global integrals from 30 day integrations with T213 truncation with and without diffusion. Fig. A.3a shows the normalized mass from the two integrations. Mass is conserved to 9 digits for the 30 days. The curves show a step structure because we only saved the unnormalized mass integrals to 10 digits. Thus, the curves show a step as the last digit changes by one. Fig. A.3b and c also show the vorticity and divergence, respectively. The global average vorticity remains around $2 \times 10^{-14} s^{-1}$ for the 30 days without diffusion and becomes almost one order of magnitude larger at the end of the 30 days with diffusion. Divergence behaves the same way in the two cases, becoming $-4 \times 10^{-16} s^{-1}$ at the end of the period. Fig. A.4a and b show the normalized total energy without and with diffusion. Without diffusion (a) the energy remains conserved to 7 digits whereas with diffusion (b) it is conserved to only 5 and decreases as expected. Fig. A.4c and d also show the normalized potential enstrophy without and with diffusion. It remains conserved to 4 digits without diffusion (c) and slightly better than 1 digit with diffusion (d), again decreasing as expected.

5. Effect of neglecting waves 107 through 213 of the reference solution

Table A.1 above indicated the uncertainty in the reference solution due to neglecting waves 107 through 213. The errors in the T106 solution are large enough that for practical purposes they can be determined using the T213 solution truncated to T106. The normalized l_1 error graphs (not shown) for the two cases fall on top of each other as do those for the l_2 error. The largest difference occurs with the normalized $l_\infty(h)$ error shown in Fig. A.5 in which the solid line is from the complete T213 solution and the dashed is from the T213 solution truncated to T106.

6. Effect of time step on error

The errors in the T106 solutions are dominated by spatial truncation, not by temporal. Fig. A.6 shows the normalized $l_1(h)$ for the T106 solution with the standard 600 sec time step (solid) and with a 300 sec step (dashed). Of the norms, the l_1 shows the largest difference, the two normalized l_2 errors lie on top of each other as do the two l_∞ norms.
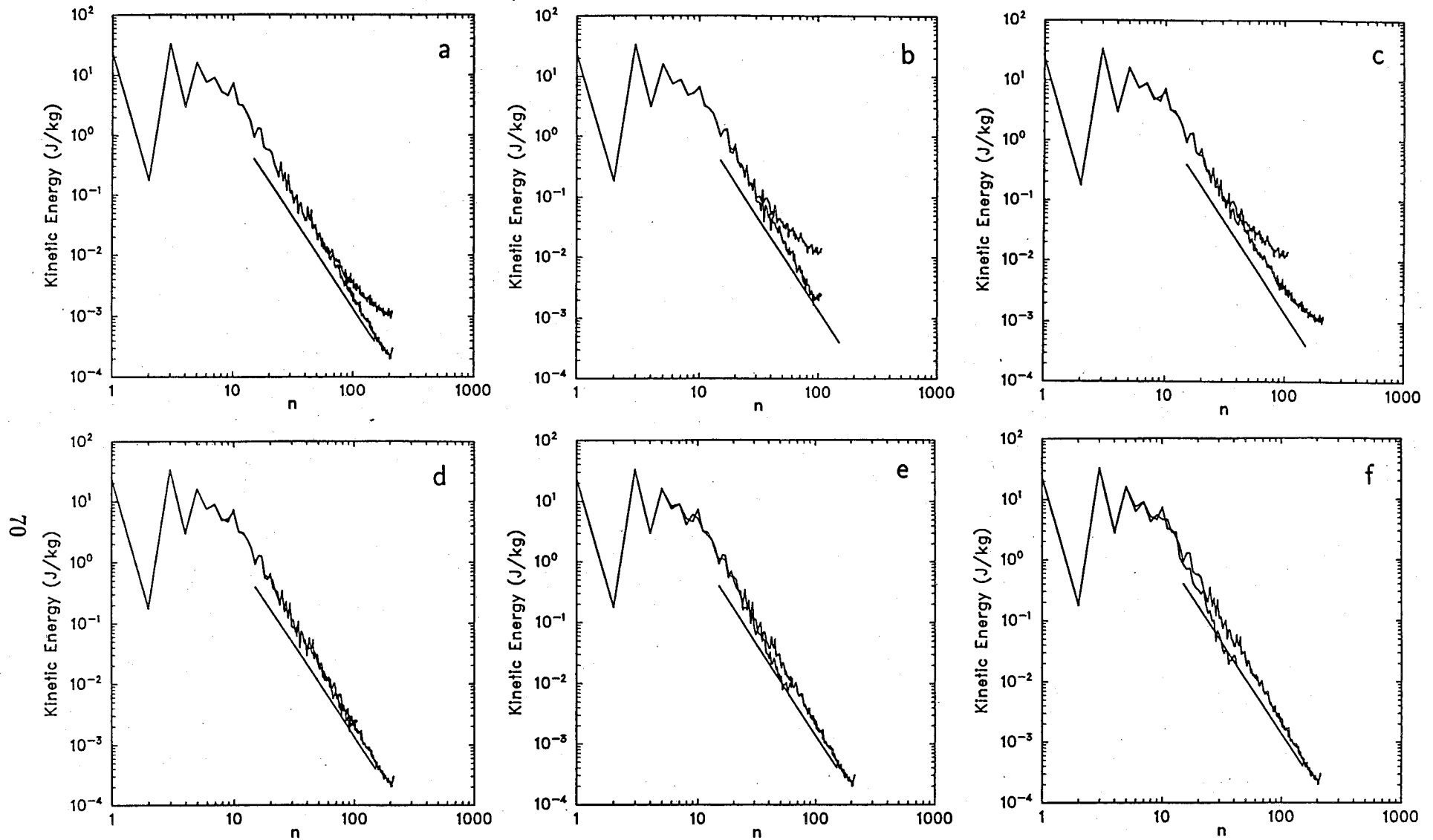
Figure A.1 Kinetic energy spectra for day 5 of forecasts from 21 December 1978. (a) T213 resolution with (lower curve) and without (upper curve) diffusion. (b) T106 with (lower curve) and without (upper curve) diffusion. (c) T213 and T106 without diffusion. (d) T213 and T106 with diffusion. (e) T213 and T63 with diffusion. (f) T213 and T42 with diffusion. The straight line in all panels has a -3 slope.
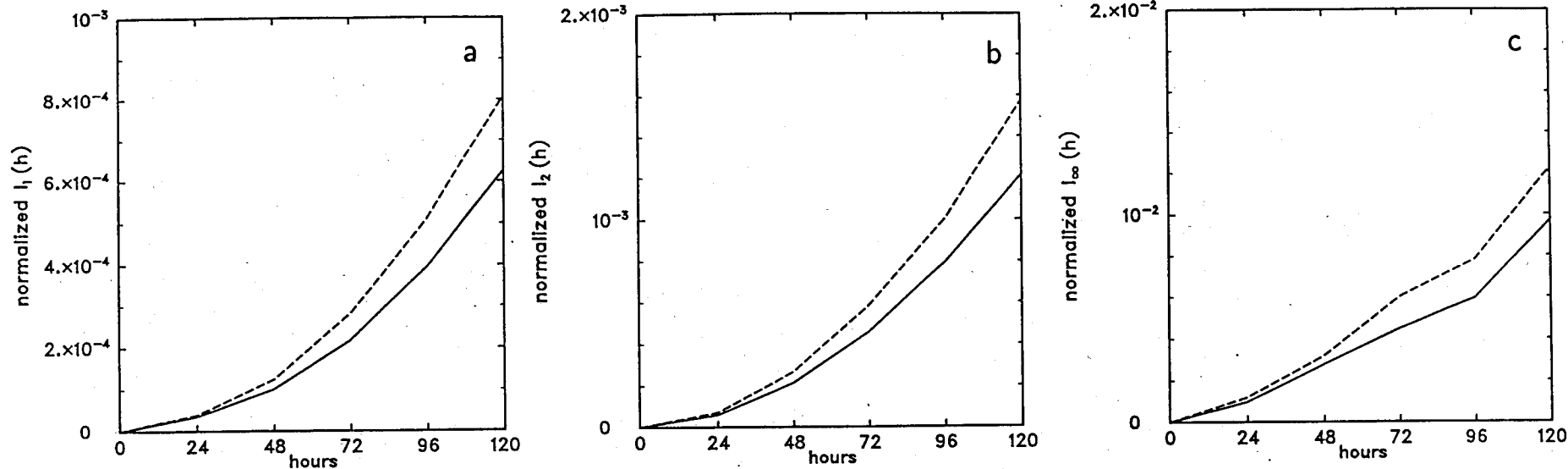
Figure A.2 l_1, l_2, and l_∞ height errors (a–c) for T106 resolution for 21 December 1978 case with (dashed) and without (solid) diffusion.
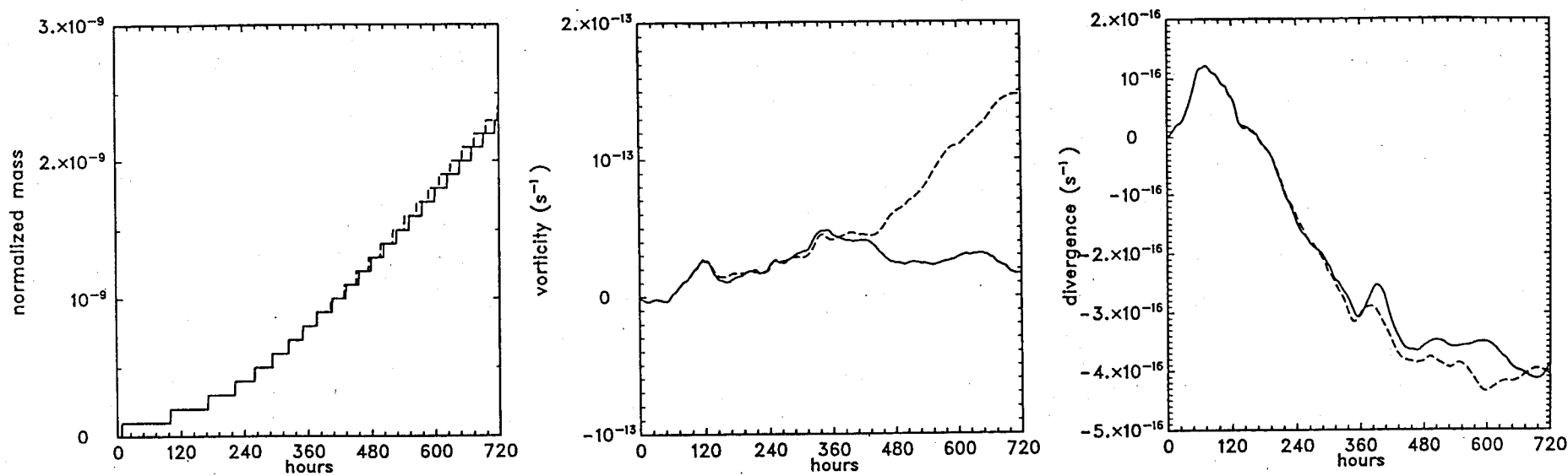

Figure A.3 Global mass, vorticity, and divergence integrals for 30 day integrations at T213 resolution of the 21 December 1978 case with (dashed) and without (solid) diffusion.
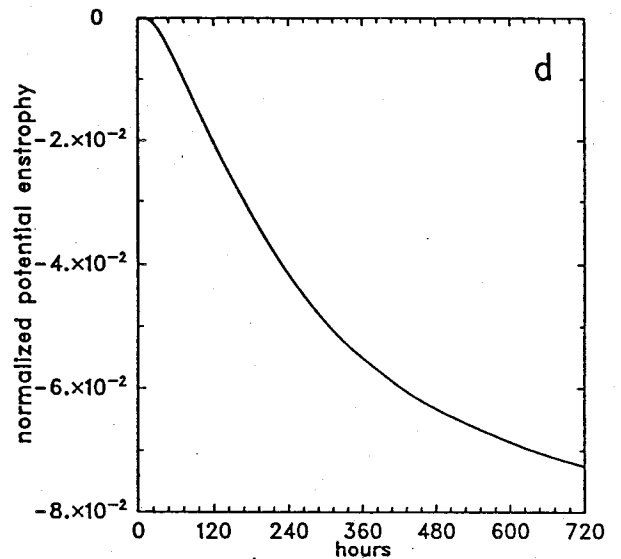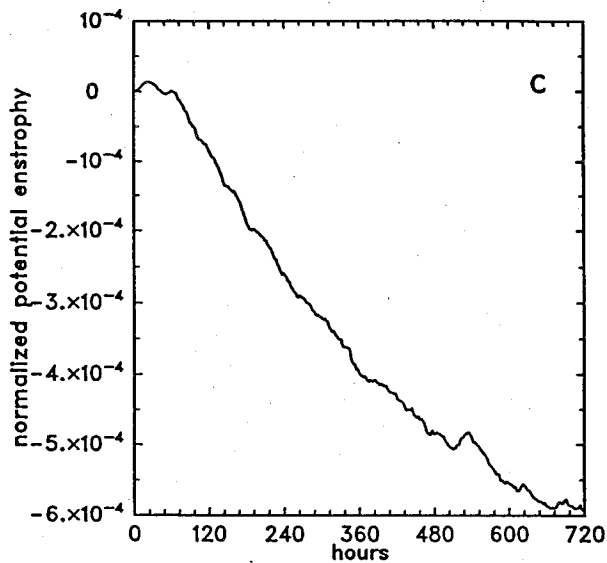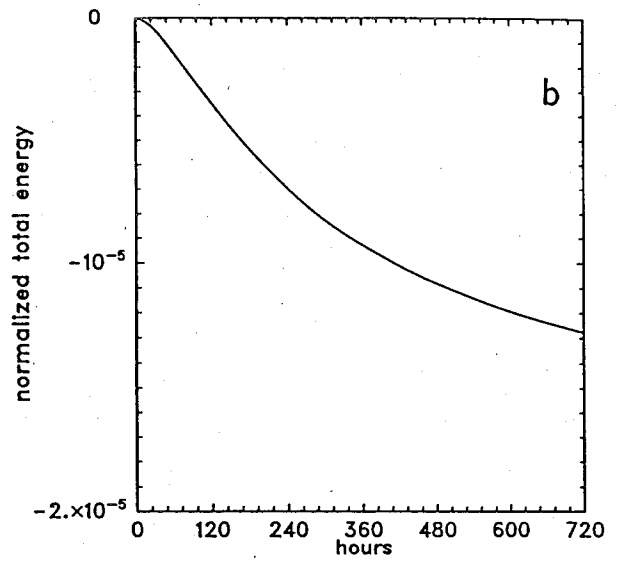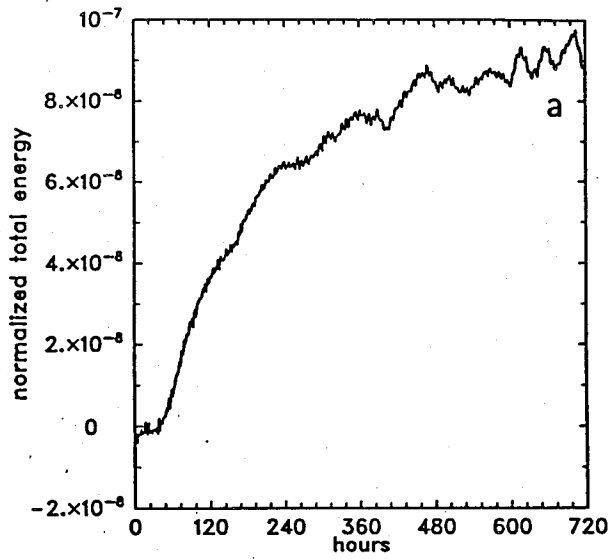
Figure A.4 Normalized total energy (a) without and (b) with diffusion and normalized potential enstrophy (c) without and (d) with diffusion for T213 resolution and 21 December 1978 Case.
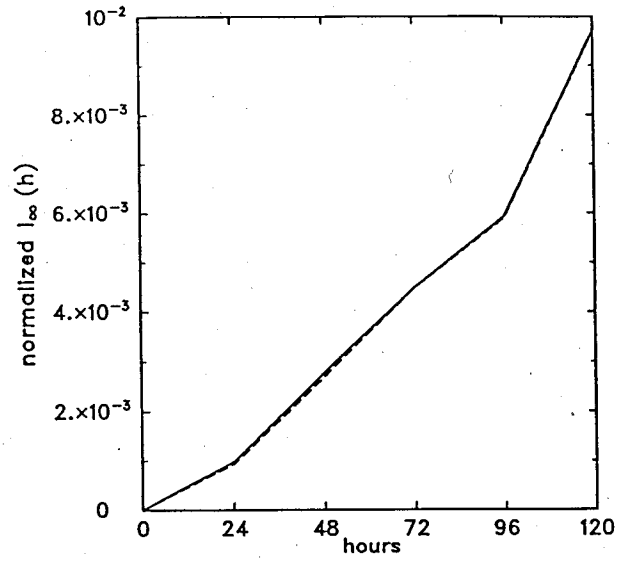
72

Figure A.5 l_∞ height difference for day 5 of T106 integration of 21 December 1978 Case compared to T213 solution (solid) and T213 solution truncated to T106 (dashed).
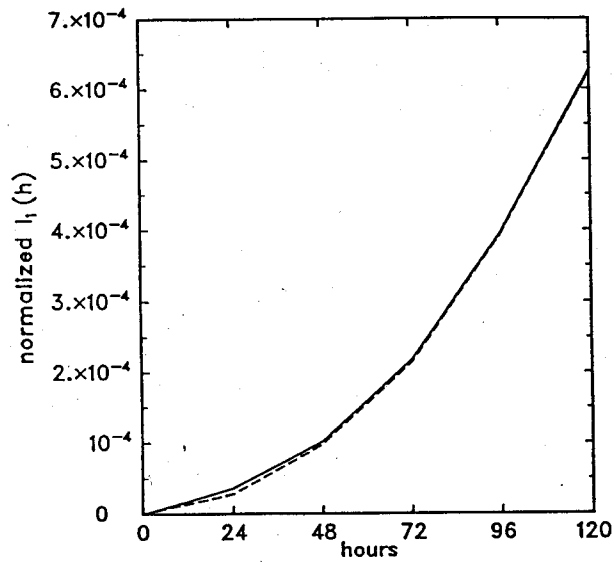

Figure A.6 l_1 height error for T106 integration of 21 December 1978 Case with 600 s (solid) and 300 s (dashed) time steps.

73

Appendix B. Calculation of Kinetic Energy Spectrum

This appendix contains the derivation of the equations for computing the kinetic energy spectrum from the spectral coefficients of divergence and vorticity. The specific kinetic energy per volume element is defined as

$$KE = \frac{1}{2}\mathbf{v} \cdot \mathbf{v} \tag{B.1}$$

where the horizontal vector velocity $\mathbf{v}$ can be represented (using the Helmholtz theorem) by the scalar streamfunction ψ and scalar velocity potential χ as

$$\mathbf{v} = \mathbf{k} \times \nabla\psi + \nabla\chi \tag{B.2}$$

The relative vorticity ζ and divergence δ are defined as

$$\zeta \equiv \mathbf{k} \cdot (\nabla \times \mathbf{v}) = \nabla^2\psi \tag{B.3}$$

and

$$\delta \equiv \nabla \cdot \mathbf{v} = \nabla^2\chi \tag{B.4}$$

Substituting (B.2) into (B.1) and using the vector identities

$$\nabla \cdot (\xi\nabla\xi) = (\nabla\xi)^2 + \xi(\nabla^2\xi) \tag{B.5}$$

and

$$(\mathbf{k} \times \nabla\psi)\nabla\chi = (\nabla\psi \times \nabla\chi) \cdot \mathbf{k} \tag{B.6}$$

the specific kinetic energy becomes

$$KE = \frac{1}{2}[\nabla \cdot (\psi\nabla\psi + \chi\nabla\chi) - (\psi\zeta + \chi\delta)] + (\nabla\psi \times \nabla\chi) \cdot \mathbf{k} \tag{B.7}$$

The global integrals of the first and last terms vanish because $\nabla \cdot (\psi\nabla\psi + \chi\nabla\chi)$ is irrotational and $\nabla\psi \times \nabla\chi$ is solenoidal. The global mean of the specific kinetic energy reduces to

$$\overline{KE} = \frac{1}{4\pi} \int_{-\frac{\pi}{2}}^{\frac{\pi}{2}} \int_0^{2\pi} -\frac{1}{2}(\psi\zeta + \chi\delta)\cos\theta d\lambda d\theta \tag{B.8}$$

In spectral space, velocity potential and divergence, as well as relative vorticity and streamfunction, are related by

$$\delta_n^m = -\frac{n(n+1)}{a^2}\chi_n^m \tag{B.9}$$

$$\zeta_n^m = -\frac{n(n+1)}{a^2}\psi_n^m \tag{B.10}$$

75

Also, since the fields are real-valued

$$\chi_n^{-m} = (-1)^m \left(\chi_n^m\right)^*$$ (B.11)

$$\psi_n^{-m} = (-1)^m \left(\psi_n^m\right)^*$$ (B.12)

where ( )* denotes the complex conjugate. Finally, the orthogonality property of the spherical basis functions is

$$\int_{-1}^{1} \int_{0}^{2\pi} P_n^m(\mu)e^{im\lambda} \left(P_l^k(\mu)e^{ik\lambda}\right)^* d\lambda d\mu = 2\pi\delta_{n,l}\delta_{m,k}$$ (B.13)

where $\delta_{n,l}$ and $\delta_{m,k}$ are Kronecker-δ functions. Substituting the last five equations into (B.8), the global mean kinetic energy can be computed as

$$\overline{KE} = \sum_{m=-M}^{M} \sum_{n=|m|}^{N(m)} \frac{n(n+1)}{4a^2} \left[\psi_n^m \left(\psi_n^m\right)^* + \chi_n^m \left(\chi_n^m\right)^*\right]$$ (B.14)

Assuming triangular truncation ($N(m) = M$), the global mean kinetic energy $\overline{KE}_n$ for spherical wavenumber $1 \le n \le M$ is thus

$$\overline{KE}_n = \frac{a^2}{4n(n+1)} \left[\zeta_n^0 \left(\zeta_n^0\right)^* + \delta_n^0 \left(\delta_n^0\right)^* + 2\sum_{m=1}^{n} \zeta_n^m \left(\zeta_n^m\right)^* + 2\sum_{m=1}^{n} \delta_n^m \left(\delta_n^m\right)^*\right]$$ (B.15)

This result is consistent with equation (19) of Merilees (1968).

Appendix C. Normal Mode Initialization

The initial data were obtained from NCAR history tape files that Trenberth and Olson (1988) compiled from ECMWF analyses. The data are available as grid point data on a T-42 spectral grid. However, the data were interpolated from the ECMWF data using cubic splines, and are therefore not spectrally truncated at T-42. In fact, the initial data contain waves up to T-63. The mean height of the 500 mb equivalent geopotential was changed to 10 km. The data were then initialized using a Machenhauer Nonlinear Normal Mode Initialization (NNMI) with Hough functions appropriate for an equivalent depth of 10 km. After an initial linear step zeroing the gravity wave amplitudes, five iterations of the NNMI were used. This procedure has been described by Errico (1987) and Errico and Eaton (1987) for the NCAR Community Climate Model. The actual initialization code for the shallow water model was provided by Andy van Tuyle (personal communication).

Figure C.1 shows the height time series for a point near Boulder, Colorado (40N,105W) computed from the uninitialized data and from the initialized data. A comparison shows that the high frequency variations in the height field have been filtered out without changing the larger scale features of the flow. Figure C.2 shows the height field before and after the NNMI and the difference initialized versus uninitialized.
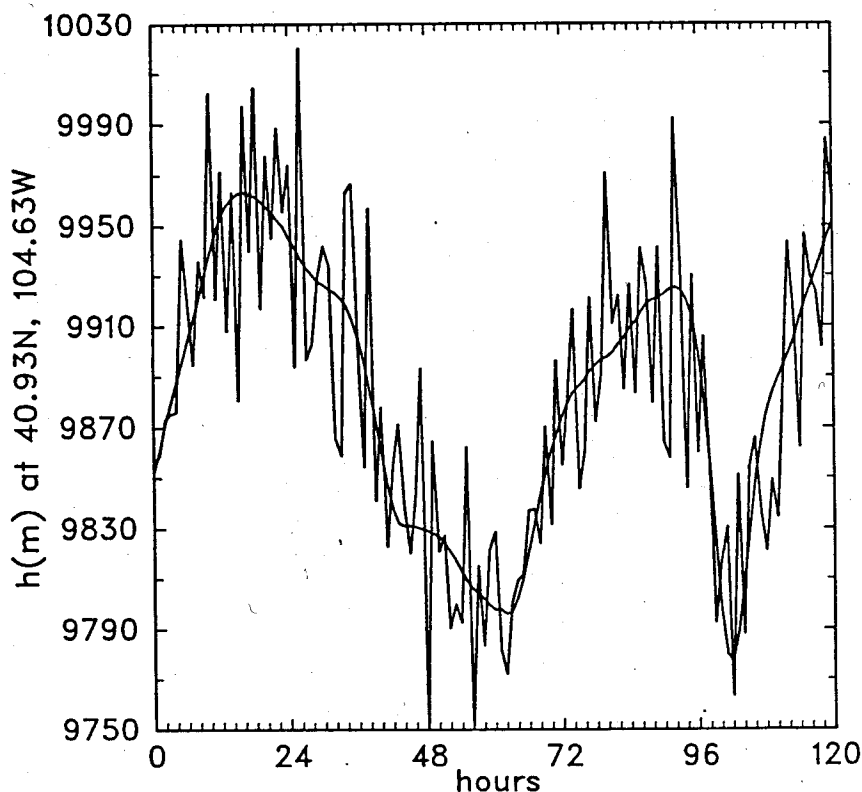

Figure C.1 Height time series without (noisy) and with (smooth) Nonlinear Normal Mode Initialization at the grid point closest to (40N, 105W).

a

CONTOUR FROM 9200 TO 10250 BY 50

b

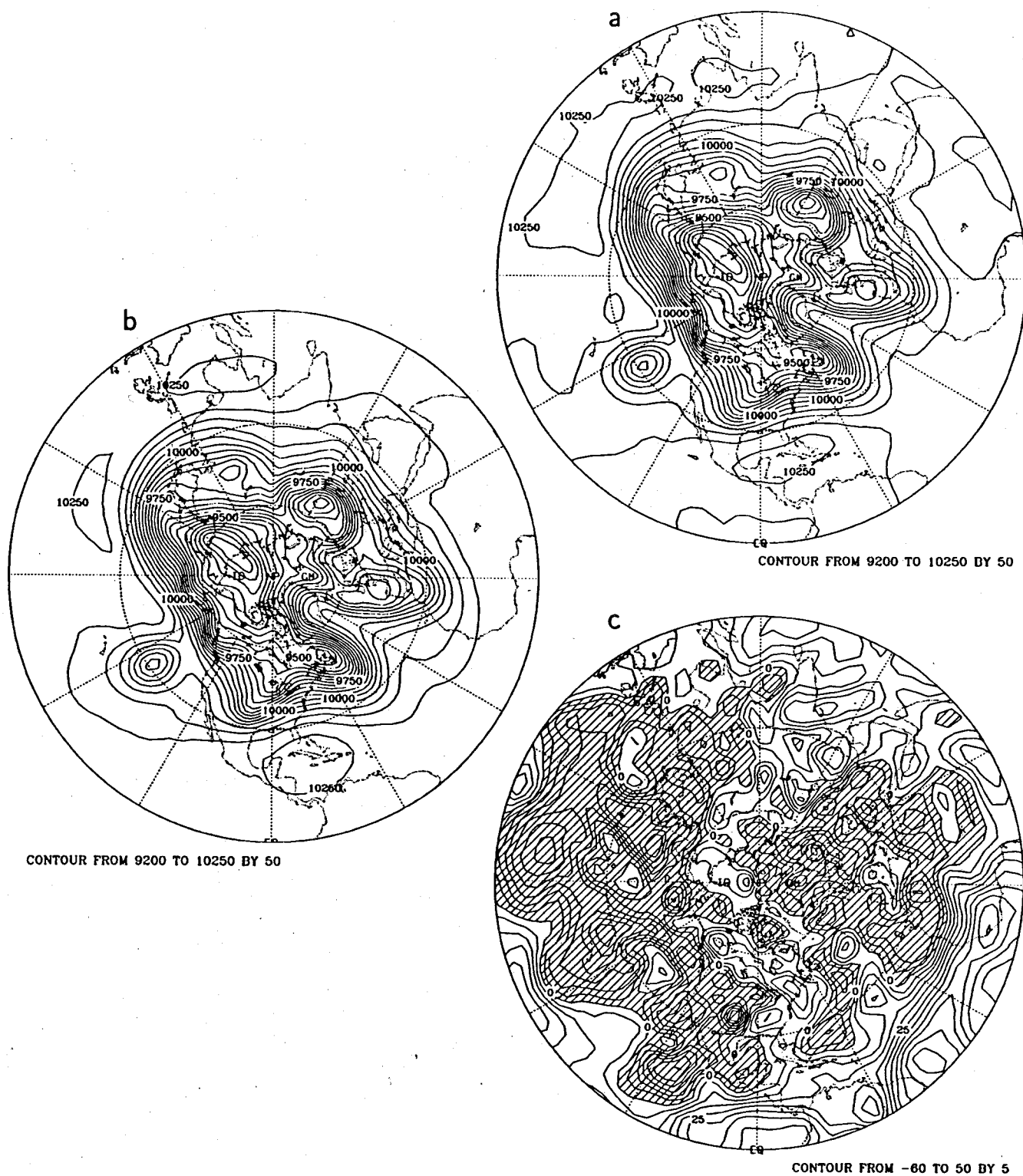CONTOUR FROM 9200 TO 10250 BY 50

c

CONTOUR FROM -60 TO 50 BY 5

Figure C.2 Height field before (a) and after (b) Nonlinear Normal Mode Initialization, and the difference, uninitialized minus initialized (c). Contour interval is 50 m for the fields and 5 m for the difference.

Acknowledgments

REFERENCES

ANSI X3J3, 1978: *Programming Language FORTRAN Standard.* American National Standards Institute, New York, NY.

Eliasen, E., B. Machenhauer, and E. Rasmussen, 1970: *On a Numerical Method for Integration of the Hydrodynamical Equations with a Spectral Representation of the Horizontal Fields.* Report No. 2, Institut for Teoretisk Meteorologi, University of Copenhagen.

Errico, R. M., 1987: *A Description of Software for Determination of Normal Modes of the NCAR Community Climate Model.* NCAR Technical Note, NCAR/TN–277+STR, 86 pp.

Errico, R.M., and B. E. Eaton, 1987: *Nonlinear Normal Model Initialization of the NCAR CCM.* NCAR Technical Note, NCAR/TN–303+IA, 106 pp.

Hack, J. J., and R. Jakob, 1992: *Description of a Shallow Water Model Based on the Spectral Transform Method.* NCAR Technical Note NCAR/TN-343+STR, 39 pp.

Jakob, R., 1993: *Fast and Parallel Spectral Transform Algorithms for Global Shallow Water Models.* Ph.D. thesis, University of Colorado, Boulder, Colorado, 125 pp.

Orszag, S. A., 1970: Transform method for calculation of vector coupled sums: Application to the spectral form of the vorticity equation. *J. Atmos. Sci.,* **27,** 890–895.

Machenhauer, B., 1979: The spectral method. *Numerical Methods Used in Atmospheric Models.* GARP Publication Series **17,** 121–275, World Meteorological Organization, Geneva, Switzerland.

Machenhauer, B., and E. Rasmussen, 1972: *On the Integration of the Spectral Hydrodynamical Equations by a Transform Method.* Report No. 3, Institut for Teoretisk Meteorologi, University of Copenhagen.

Matsumoto, S., 1961: A note of geostrophic adjustment and gravity wave in the atmosphere. *J. Meteor. Soc. Japan,* **39,** 18–28.

Merilees, P. E., 1968: The equations of motion in spectral form. *J. Atmos. Sci.*, **25**, 736–743.

Rossby, C. G., 1938: On the mutual adjustment of pressure and velocity distributions in certain simple current systems. *J. Marine Res.*, **1**, 239–263

Temperton, C., 1983: Fast Mixed-Radix Real Fourier Transforms. *J. Comp. Physics*, **52**, 340–350.

Trenberth, K. E. and J. G. Olson, 1988: *ECMWF Global Analyses 1979–1986: Circulation Statistics and Data Evaluation*. NCAR Tech. Note NCAR/TN-300+STR, National Center for Atmospheric Research, Boulder, Colo., NTIS PB88-178165/AS, 12 fiche, 94pp.

Williamson, D. L., J. T. Kiehl, V. Ramanathan, R. E. Dickinson, J. J. Hack, 1987: *Description of the NCAR Community Climate Model (CCM1)*. NCAR Technical Note NCAR/TN-285+STR, NTIS PB87-203782/AS, 112 pp.

Williamson, D. L., J. B. Drake, J. J. Hack, R. Jakob, and P. N. Swarztrauber, 1992: A Standard Test Set for Numerical Approximations to the Shallow Water Equations in Spherical Geometry, *J. Comp. Phys.*, **102**, 211–224.